Technische Universität München
TUM School of Natural Sciences

Clinical Dark-Field Chest Radiography – Patient Exposure and Application for COVID-19-pneumonia

Manuela Stefanie Frank

Vollständiger Abdruck der von der TUM School of Natural Sciences der Technischen Universität München zur Erlangung des akademischen Grades einer

Doktorin der Naturwissenschaften (Dr. rer. nat.)

genehmigten Dissertation.

Vorsitz:	Prof. Dr. Martin Zacharias
Prüfer*innen der Dissertation:	1. Prof. Dr. Franz Pfeiffer
	2. Prof. Dr. Matthias Hebrok

Die Dissertation wurde am 20.01.2023 bei der Technischen Universität München eingereicht und durch die TUM School of Natural Sciences am 01.05.2023 angenommen.

Abstract

Chest radiography is commonly used in clinical routine for the initial assessment of the lung. However, its diagnostic sensitivity for the detection of pulmonary disorders such as pulmonary emphysema or fibrosis is rather low, especially in early stages of disease. Contrast formation is based on the attenuation of X-rays alone, while the air-filled lung itself is overlayed by surrounding tissue and bones. Dark-field radiography is a novel and promising interferometric X-ray imaging technique that provides additional contrast information in comparison to the conventional attenuation signal. Due to small-angle scattering of X-rays, the otherwise unresolvable microstructure of the imaged specimen can be visualized. Various animal models showed that the lung's alveolar structure can be well assessed with dark-field radiography, allowing for facilitated diagnosis of numerous pulmonary diseases. Recently, a clinical prototype system for dark-field chest radiography was commenced in operation and applied to human subjects for the first time.

In this PhD project, the benefits and risks associated with dark-field chest radiography for patients were evaluated. An extensive risk analysis concerning the effective radiation dose a subject is exposed to, along with a comparison to regulatory dose levels, was conducted. As a central result, we found that the effective dose at the clinical dark-field radiography system is within the range of reported standard dose values for chest radiography, enabling further research on this method's potential in humans. Also, different exposure control methods were developed, validated with an anthropomorphic phantom, and evaluated for patient examinations. We have successfully implemented exposure control approaches that deliver images of diagnostic quality. After ensuring the safe application of dark-field radiography for patients, its benefits for the assessment of COVID-19-pneumonia were evaluated in comparison to conventional attenuation-based chest radiography. We found that dark-field imaging has a higher sensitivity for COVID-19-pneumonia than attenuation-based imaging. Moreover, the simultaneous display of both modalities is superior to dark-field imaging alone. Based on the results of the risk analysis and first imaging results concerning lung diseases within the range of this thesis, we are fully convinced that dark-field chest radiography complements and improves conventional radiography for the assessment of pulmonary disorders in a dose-compatible manner.

Zusammenfassung

Die Röntgenaufnahme des Brustkorbs wird in der klinischen Routine häufig für die Erstbeurteilung der Lunge verwendet. Ihre diagnostische Sensitivität für den Nachweis von Lungenerkrankungen wie Lungenemphysem oder Fibrose ist jedoch eher gering, insbesondere in frühen Krankheitsstadien. Die Kontrastbildung beruht allein auf der Abschwächung der Röntgenstrahlen, während die luftgefüllte Lunge selbst von umgebendem Gewebe und Knochen überlagert wird. Die Dunkelfeld-Radiographie ist ein neuartiges und vielversprechendes interferometrisches Röntgen-Bildgebungsverfahren, das im Vergleich zum herkömmlichen Abschwächungssignal zusätzliche Kontrastinformationen liefert. Durch die Kleinwinkelstreuung der Röntgenstrahlen kann die sonst nicht auflösbare Mikrostruktur der abgebildeten Probe sichtbar gemacht werden. Verschiedene Tiermodelle haben gezeigt, dass die Alveolarstruktur der Lunge mit der Dunkelfeldradiographie gut beurteilt werden kann, was die Diagnose zahlreicher Lungenkrankheiten erleichtert. Kürzlich wurde eine klinische Prototypenanlage für die Dunkelfeld-Thorax-Radiographie in Betrieb genommen und zum ersten Mal an Menschen angewendet.
In diesem Promotionsprojekt wurden die Vorteile und Risiken der Dunkelfeld-Thorax-Radiographie für Patienten bewertet. Es wurde eine umfassende Risikoanalyse bezüglich der effektiven Strahlendosis, der eine Person ausgesetzt ist, sowie ein Vergleich mit den gesetzlichen Dosiswerten durchgeführt. Als zentrales Ergebnis stellten wir fest, dass die effektive Dosis am klinischen Dunkelfeld-Radiographiesystem im Bereich der Standarddosiswerte für die Thorax-Radiographie liegt, was weitere Untersuchungen zum Potenzial dieser Methode für den Menschen ermöglicht. Außerdem wurden verschiedene Methoden zur Belichtungssteuerung entwickelt, an einem anthropomorphen Phantom validiert und für Patientenuntersuchungen evaluiert. Wir haben erfolgreich Ansätze zur Belichtungssteuerung implementiert, die Bilder von diagnostischer Qualität liefern. Nachdem wir die sichere Anwendung der Dunkelfeld-Radiographie für Patienten sichergestellt hatten, wurde ihr Nutzen für die Beurteilung der COVID-19-Pneumonie im Vergleich zur herkömmlichen, auf Abschwächung basierenden Thorax-Radiographie bewertet. Es zeigte sich, dass die Dunkelfeld-Bildgebung eine höhere Sensitivität für COVID-19-Pneumonie aufweist als die auf Abschwächung basierende Bildgebung. Außerdem ist die gleichzeitige Darstellung beider Modalitäten der Dunkelfeld-Bildgebung allein überlegen. Aufgrund der Ergebnisse der Risikoanalyse und erster Bildgebungsergebnisse bei Lungenerkrankungen im Rahmen dieser Arbeit sind wir davon überzeugt, dass die Dunkelfeld-Thorax-Radiographie die konventionelle Radiographie bei der Beurteilung von Lungenerkrankungen dosisverträglich ergänzt und verbessert.

Contents

1 Introduction

Medical X-ray imaging is an indispensable tool used worldwide to generate images of tissues and structures inside the human body both noninvasively and painlessly. With approximately 130 million X-ray procedures in the year 2018 in Germany alone [BfS, 2022], X-ray imaging plays an important role in clinical routine.
X-ray imaging examinations cover a wide variety of clinical examinations and procedures. These include disease diagnosis and therapy monitoring, medical and surgical treatment planning support, and guidance of medical personnel for the insertion of catheters, stents, or other devices into the body [FDA, 2022]. Even for patients with contraindications for other imaging modalities such as magnetic resonance imaging (MRI), X-ray imaging can be performed. Depending on the clinical indication, three different methodologies are applied. Plain radiography renders a two-dimensional projection, fluoroscopy enables the acquisition of real-time moving images, and computed tomography (CT) imaging provides three-dimensional information of the imaged body part. Yet there is always an associated risk for X-ray examinations, as X-rays are a form of ionizing radiation. Ionizing radiation has enough energy to potentially damage the DNA and thereby enhance the probability of cancer growth. The associated risk of medical examinations is generally below the threshold for causing deterministic effects, however increasing the statistical risk. Although CT imaging provides more information of the examined subject, it is also associated with a considerably higher effective radiation dose than plain radiography [Mettler, 2008]. Each patient's exposure has to be measured and assessed [BfS, 2022], and the exposure of each kind of examination has to be monitored and controlled.

From the discovery of X-rays by W. C. Röntgen in 1895 [Röntgen, 1896], medical X-ray technologies were developed further at an astounding speed. These new advances were only possible by a comprehensive approach bringing advancements in X-ray sources, medical detectors, computed tomography techniques, and digital image processing together [Pfeiffer, 2018]. However, all the aforementioned applications in use today rely on the same contrast formation mechanism in use fore over 100 years. Today's medical applications, i.e. plain radiography, fluoroscopy, and CT imaging, rely on the X-rays' varying attenuation of the internal structures of the investigated specimen. Especially in functional imaging or soft tissue structures with low contrast, current technology

reaches its limit. Contrast agents are often used to enhance contrast in soft tissues with similar attenuation, at the cost of potential adverse effects such as allergic reactions [FDA, 2022].

In basic research, different contrast formation mechanisms such as phase-shift and multiple refractions of X-rays have been proposed to overcome the above mentioned limitations [Bonse, 1965]. Methods for recording the phase-shift of X-rays include among others propagation-based X-ray imaging [Snigirev, 1995], speckle-based X-ray imaging [Bérujon, 2012], and grating-based X-ray interferometry [Momose, 2003]. Due to rigid requirements on X-ray source coherence, these imaging techniques were originally restricted to large-scale synchrotron facilities [Pfeiffer, 2013].
This changed in 2006, when Pfeiffer et al. achieved grating-based X-ray interferometry with low-brilliance X-ray sources with limited coherence [Pfeiffer, 2006]. By using a three-grating interferometer, the phase-shift and small-angle scattering of X-rays at interfaces can be measured [Momose, 2003; Pfeiffer, 2006; Pfeiffer, 2008]. The small-angle scattering, or multiple refraction, at material interfaces is visualized in the so-called dark-field image. The dark-field signal provides structural information on the micron scale, below the physical resolution of the imaging system [Pfeiffer, 2009]. This combination of grating-interferometry and widely available X-ray sources enabled the evaluation of the potential of phase-contrast and dark-field contrast for a broad range of applications.

After this transition, the first imaging study of an in-vivo mouse proved the high potential of dark-field X-ray imaging for the evaluation of the lungs, as their pulmonary microstructure causes a high amount of small-angle scattering resulting in a high dark-field signal [Bech, 2013]. Consequently, diseases that affect the lungs' microstructure and reduce the amount of interfaces in the lung result in a decreased dark-field signal in the affected region. The change in alveolar structure can either be caused by its destruction, consolidation, or invasive growth corresponding to pulmonary emphysema, pneumonia, or cancer, respectively [Pfeiffer, 2018]. Soon dark-field radiography was advanced to dark-field CT imaging, resulting in three-dimensional dark-field information of the lung [Velroyen, 2015].

After several studies in small-animal models proved the diagnostic benefit and additional value of dark-field imaging for lung pathologies [Yaroshenko, 2013; Meinel, 2013; Yaroshenko, 2015; Hellbach, 2015; Yaroshenko, 2016; Hellbach, 2017], the technology was further advanced for the applications in large animals [Gromann, 2017; Hellbach, 2018] and finally, living humans. Recently, the first clinical prototype for X-ray dark-field chest imaging in humans was commissioned and constructed at a clinical site (Klinikum rechts der Isar, Munich, Germany).

While numerous pre-clinical studies showed the potential of dark-field chest imaging, within this PhD thesis we evaluate the safety of this new imaging technique for the

application to humans. For this purpose, we conducted an in-depth dose analysis. In this work, we establish dosimetry performed at the clinical prototype system. We evaluate the effective radiation dose deposited in the reference person, and compare that dose to literature values for chest radiography. A comprehensive dose analysis is a requirement for the wide-spread application of any new imaging techniques and especially important in order to show that dark-field imaging could be a low-radiation alternative for disease monitoring or screening applications.

Further, the safe application also includes control mechanisms for exposure that are patient-specific. Overexposure results in an increased radiation dose for the patient, while underexposure results in reduced signal-to-noise ratio which may impede diagnosis. In order to produce diagnostic images with a reasonable trade-off between radiation dose and contrast, we developed two methods for exposure control, validated them with an anthropomorphic phantom and evaluated them for patient examinations.

Controlling the risks associated with dark-field chest radiography for humans allows the execution of a patient study on the benefits of dark-field imaging on manifestations of COVID-19-pneumonia. For that purpose, we evaluate the image appearance of dark-field radiographs of patients with COVID-19-pneumonia in comparison to participants without pulmonary disorders. In a reader study, we investigate conventional attenuation and novel dark-field chest radiographs of healthy controls and patients with COVID-19-pneumonia for their capability of the assessment of the lungs' condition. Only by evaluating both risks and benefits of dark-field chest radiography, we can classify the potential of the new imaging method.

Outline

Chapter 2 of this PhD thesis covers the physical background of X-ray imaging, both based on attenuation and small-angle scattering. Further, the concepts of dosimetry and the regulatory parameters concerning exposure control are introduced and the medical background relevant for X-ray dark-field lung imaging is explained.
The clinical prototype for X-ray dark-field chest imaging is described in Chapter 3. Set-up specific image corrections and processing steps are presented. Additionally, a summary of the patient studies conducted during this PhD project is given.
In Chapter 4, the dosimetry conducted at the dark-field prototype is presented. For this purpose, the effective dose deposited into a phantom modeling the standardized adult man is reported. Also, the methodology on radiation dose estimation for patients is described, and analyzed for the first 92 imaged participants. The recorded values are also compared to legal dose limits.
Since the radiation dose is dependent on patient exposure, two different approaches on exposure control implemented in the current patient studies are presented in Chap-

ter 5. The first one relies on a scout scan on a reference device with automatic exposure control (AEC), while the second is based on body parameters of the patient. Both approaches are evaluated for the safe application of this new imaging method.
As the technical implementations of dosimetry and exposure control were successful and demonstrated the feasibility of clinical X-ray dark-field chest imaging, this technique is applied for the assessment of COVID-19-pneumonia. The image appearance of COVID-19-pneumonia in contrast to healthy lungs is discussed in Chapter 6. Further, a reader study and a quantitative analysis are conducted to evaluate the capability of X-ray dark-field imaging for the detection of COVID-19-pneumonia.
The last chapter, Chapter 7, summarizes the presented work in this thesis and further challenges and potential next steps associated with dark-field chest radiography are discussed.

Further remarks

The scientific results described in this work originate from a collaborative effort of a multidisciplinary team, consisting of fellow PhD students as well as clinical and industrial partners. For further insight, the reader is referred to the PhD theses of my colleagues as follows: for more information on the preceding system for large animals and deceased humans, look into the PhD theses of Lukas Gromann, Fabio De Marco, and Jana Andrejewski. More information on the conception, technical implementations, and image reconstruction algorithms of the clinical dark-field prototype system, seek the works of Konstantin Willer, Alex Gustschin, Wolfgang Noichl, Theresa Urban, and Rafael Schick. More results on the clinical impact of dark-field chest radiography can be found in the PhD theses of Konstantin Willer, Theresa Urban, and Henriette Bast as well as the habilitation reports of Alexander Fingerle, Andreas Sauter, and Florian Gassert.

Theoretical Background 2

In this chapter, the physical concepts necessary to understand this thesis and further background are introduced. In the beginning, Röntgen radiation (X-rays) are introduced. Next, a short introduction to grating-based X-ray interferometry is given. Then, dosimentry and its consequences for a safe application are described. Next, measures for exposure control are introduced. The chapter ends with information about the medical background relevant for the application of dark-field radiography on lungs.

2.1 Definition of X-rays

X-rays (or Röntgen radiation) are a form of electromagnetic radiation discovered by W. C. Röntgen [Röntgen, 1896]. Within the electromagnetic spectrum, they are found at energies between a few 100 eV to 100 keV, corresponding to short wavelengths between ultraviolet and gamma rays from about 0.1 to 100 Å ($1\,\text{Å} = 1 \times 10^{-10}\,\text{m}$). In vacuum, their energy is defined by

$$E = \frac{hc}{\lambda} = \hbar\omega, \tag{2.1}$$

with the speed of light $c = 2.998 \times 10^9\,\text{m}\,\text{s}^{-1}$, Planck's constant $h = 4.136 \times 10^{-15}\,\text{eVs}$ ($\hbar = h/(2\pi)$), wavelength λ, and radiation frequency $\omega = 2\pi f$. Often (and for applications in this thesis), X-rays are produced by accelerating electrons from a heated cathode towards an anode target with tube voltages between 25 kV and 150 kV. Radiative energy loss through electrons slowing down in the target material results in so-called *bremsstrahlung* with a continuous range of energies from the energy caused by the highest accelerating voltage downwards. Further, radiative transitions of electrons within the atom of the target material cause so-called characteristic X-rays, which occur at discrete energies characteristic to the anode target material.
X-rays, as part of the electromagnetic spectrum, have both a particle and wave-like behavior due to the wave-particle dualism. The particle aspect of X-rays helps to explain the interaction between X-rays and the electrons of an atom, while their wave nature

accounts for the phenomena of refraction and interference. Both aspects are important in X-ray imaging, as described in the following.

2.1.1 X-ray Interactions with Matter

X-rays used for medical imaging usually have energies of at least the binding energies of inner shell electrons of an atom, yet lower than the energies required for pair production. Thus, interactions occur mainly between X-ray photons and the electrons of the irradiated object.

Photoelectric Effect and Fluorescence

The process of an incident photon being absorbed by an atom, and its complete energy being transferred to an atomic electron, which in turn leaves the atom, is called photoelectric absorption or photoelectric effect. For this effect to occur, the energy of the incident photon has to be at least as high as the binding energy of the atomic electron. Excess energy is imparted as kinetic energy of the freed electron.

The inverse effect, i.e., an electron transitioning to a lower energy level within the atom by emission of a photon, is called X-ray fluorescence. This effect results in the characteristic peaks of an X-ray spectrum.

Elastic Scattering

In an elastic scattering process, incident and scattered radiation have the same wavelength. Therefore, no energy is transferred to the electron. This kind of scattering is also called Thomson scattering or coherent scattering.

Inelastic Scattering

Compton scattering (or incoherent scattering) is an inelastic interaction between the incident photon and electrons in an outer shell of the atom. During the interaction process, a part of the energy of the incoming photon is transferred to the electron, which is in turn ejected from the shell. The scattered photon leaves with decreased energy or a longer wavelength.

2.1.2 Complex Refractive Index

The interaction of an electromagnetic wave with matter, as summarized above, can be characterized by the complex refraction index n:

$$n = 1 - \delta + i\beta, \tag{2.2}$$

where the imaginary part β describes the attenuation strength and δ the index decrement responsible for phase shift. A plane wave $\Psi(\vec{r})$ interacting with matter can therefore be described as

$$\Psi(\vec{r}, t) = E_0 e^{in\vec{k}\cdot\vec{r}} = E_0 e^{i(1-\delta)\vec{k}\cdot\vec{r}} e^{\beta\vec{k}\cdot\vec{r}}. \tag{2.3}$$

Here, E_0 is the initial wave amplitude, $\vec{r}$ the position in space, and $\vec{k}$ the wave vector with $\left|\left(\vec{k}\right)\right| = \frac{2\pi}{\lambda}$. The real part of equation 2.3 is responsible for the exponential decay of the wave's amplitude with propagation distance. The transmitted intensity after propagation distance L can be expressed as

$$T(L) = \frac{I(L)}{I_0} = \frac{|\Psi(L)|}{|\Psi_0|} = e^{-2k\beta L} = e^{-\mu L}, \tag{2.4}$$

which is known as the *Lambert-Beer* law with the absorption coefficient $\mu = 2k\beta$ [Beer, 1852]. Additionally, the wave will experience a phase shift described by the imaginary part of equation 2.3 and given by

$$\Delta\Phi = \delta\vec{k}\vec{r}. \tag{2.5}$$

The underlying interaction effects also depend on the X-ray energy. To extend the model for the use of conventional, polychromatic X-ray sources, an integral over the involved energies with a weighting factor accounting for spectral distribution is performed.

2.2 Grating-based X-ray Interferometry

2.2.1 Talbot Effect

In 1836, Henry Fox Talbot discovered that a periodic structure, e.g., a grating, that is illuminated by coherent light repeats itself after certain propagation distances and

a so-called self-image of the structure occurs [Talbot, 1836]. These images occur at propagation distances

$$d_T = \frac{2p^2}{\lambda}, \tag{2.6}$$

with the structure period p and the wave length λ of the illuminating light. This distance is also called *full Talbot distance*. In 1881, Lord Rayleigh explained the effect theoretically [Rayleigh, 1881]. Additionally, intensity patterns with a high correlation to the initial structure can be observed at fractional Talbot distances. An evaluation of (fractional) Talbot distances for a combination of different duty cycles and phase-shifting properties was carried out by Suleski [Suleski, 1997]. Based on this work, the grating interferometer described in the following and used for this thesis was designed.

2.2.2 X-ray Grating Interferometer

Introducing a sample into the beam path modifies the downstream fields. By exploiting the aforementioned Talbot Effect, information on the object is extracted in grating-based interferometry by analyzing the change in the intensity pattern caused by the sample. Three different effects can be distinguished: Attenuation, refraction, and small-angle scattering. A purely absorbing object reduces the amplitude of the detected pattern uniformly, meaning all measured intensities are reduced by a constant factor. Refraction along the pattern's periodicity leads to a lateral shift of the pattern as the incident and transmitted propagation directions deviate. Small-angle scattering results in diffusion of the X-rays' direction and an according amplitude reduction in the detected pattern while its mean intensity remains constant. These effects on the intensity pattern are schematically depicted in Figure 2.1.

The change of the interference pattern can be recorded with a three-grating interferometer introduced by [Momose, 2003; Pfeiffer, 2006; Pfeiffer, 2008; Pfeiffer, 2009] and exploited for this thesis. In grating-based interferometry, the periodic structure that imprints an intensity modulation onto the incoming wavefront is called reference grating G1. For the energy range used in medical X-ray imaging and flux limitations, the period of G1 has to be in the order of a few µm. Such periods are one order of magnitude smaller than the pixel size of flat-panel detectors used for radiography, because of which these detectors cannot directly resolve the self-images. In order to decouple detector resolution from grating periods, a binary absorption mask realized as an absorbing grating (called analyzer grating G2) is placed in front of the detector. The position of the analyzer grating must match a (fractional) Talbot distance to exploit the self-image's intensity modulation, and the grating's period must match the intensity's period. This way, the transmitted intensity behind the second grating

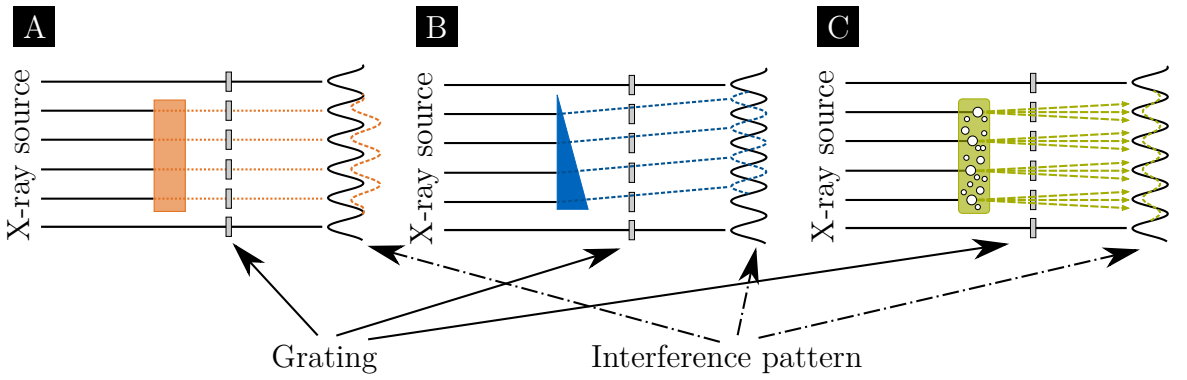

Figure 2.1: Modification of intensity pattern caused by three idealized sample types in a Talbot interferometer. A, A purely attenuating object reduces the intensity pattern's mean intensity. B, The lateral phase-shift of the intensity pattern is caused by the refraction of an object. C, Multiple scattering within an object reduces the amplitude of the intensity pattern. Figure adapted from [Umkehrer, 2022].

is constant, and the measured signal in a detector pixel is independent of pixel size.

An additional requirement for the Talbot effect is sufficient spatial coherence in the direction orthogonal to the grating lines, which clinical X-ray tubes lack. By introducing an additional attenuating grating to the interferometer near the X-ray source, this source grating G0 acts as a special collimator: For one, the single slits must be narrow enough to ensure a sufficiently high coherence. The X-rays emitted from each slit produce Talbot self-images on the analyzer grating. For the other, the distance between two slits must be matched so that the self-images of each slit are in phase with each other.

This second condition of phase-matched self-images from each grating line is fulfilled if

$$\frac{p_0}{p_2} = \frac{L}{D}, \tag{2.7}$$

with p_0 and p_2 being the periods of G0 and G1, respectively, L the distance between G0 and G1, and D the distance between G1 and G2 (see Figure 2.2). Pfeiffer et al. first presented this arrangement, called Talbot-Lau interferometer, for the use with X-rays [Pfeiffer, 2006]. For clinical X-ray tubes, additionally the cone-beam geometry and the resulting magnification have to be considered. The corresponding effect on grating periods has previously been described in e.g. [Bech, 2009].

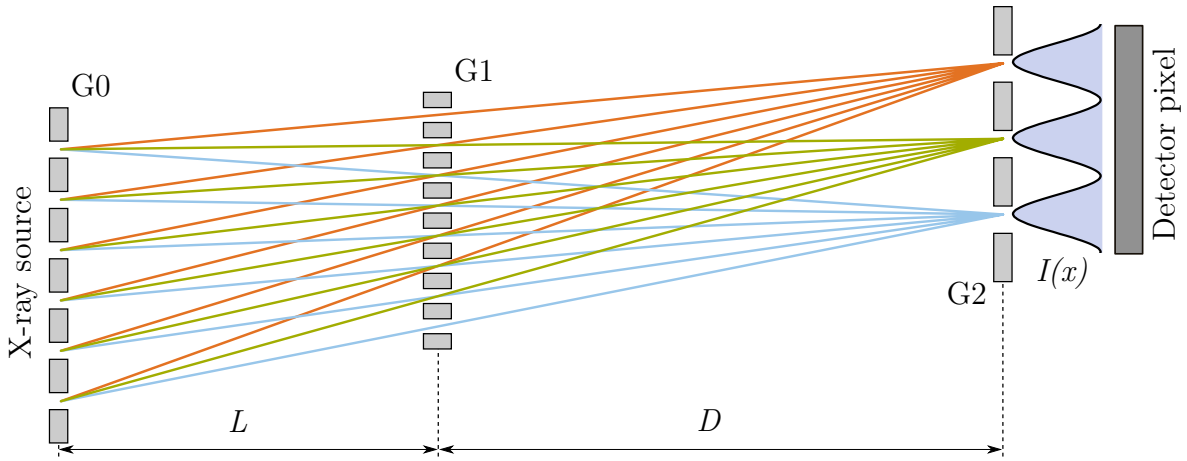

Figure 2.2: Geometric condition for phase-matched self-images. The individual slits of grating G0 with periodicity p_0 act as independent X-ray sources. The X-rays emitted from each slit produce Talbot self-images of the G1, which is positioned at a distance L. The self-images interfere constructively after propagation distance D, resulting in an intensity pattern $I(x)$ with a periodicity of p_2. For the intensity pattern to arise, the grating periods and distances must fulfill the geometric constraint given in Equation 2.7. Figure adapted from [Willer, 2022].

2.2.3 Phase Stepping

Under these conditions, the intensity measured at the detector pixels only depends on the relative position of the grating bars of G2 to the self-image. By a lateral translation of either grating, this relative phase can be altered, which in turn leads to a variation of measured intensity. At any point of the field of view (FOV), this intensity must be a periodic function of lateral grating translation. By recording the intensity as a function of the grating position, the so-called *stepping curve* is obtained for every pixel (m, n):

$$I(m, n, x_g) = a_0(m, n) + a_1(m, n) \cdot \cos\left[\phi(x, y) + x_g \frac{2\pi}{p_2}\right]. \tag{2.8}$$

Here, x_g denotes each *phase step*, e.g. relative G2 to self-image phase, a_0, a_1, and ϕ the corresponding coefficients [Pfeiffer, 2009]. Two such stepping curves are depicted in Figure 2.3, one with and one without a sample in the beam path, denoted with the superscripts $(^s)$ and $(^r)$ for sample and reference, respectively. By comparing the recorded stepping curves, all three modalities, e.g., attenuation, refraction, and small-angle scattering, can simultaneously be extracted as follows:

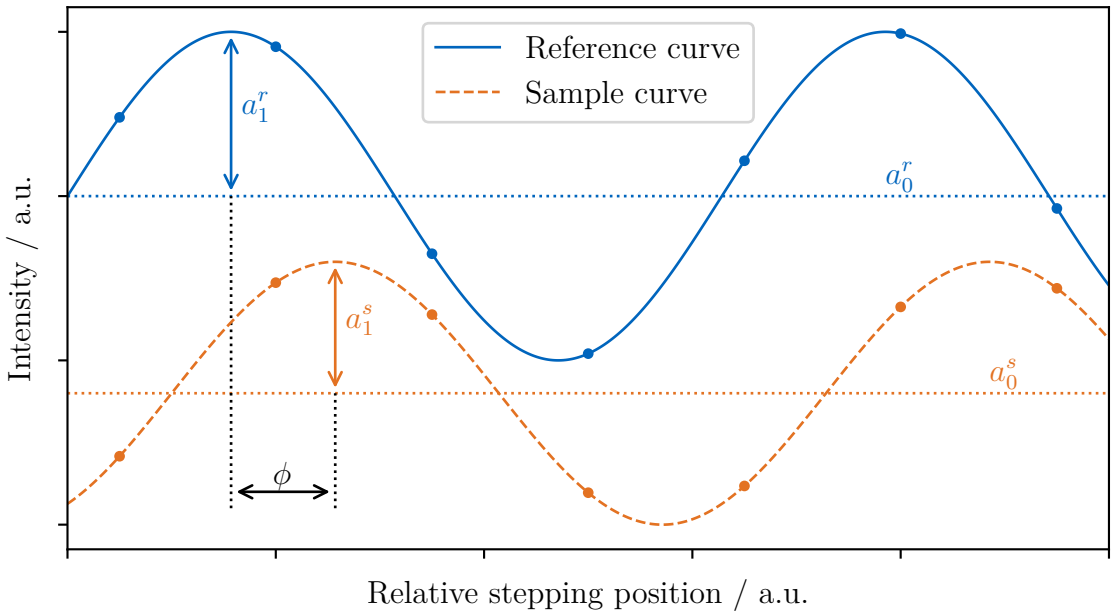

Figure 2.3: Schematic of stepping curve for a reference scan (blue, solid line, indicated by superscript (^{r})) and a sample scan (orange, dashed line, indicated by superscript (^{s})). The three coefficients describing the periodic function, namely mean intensity a_0, amplitude a_1, and relative phase ϕ, are depicted. The absorption, phase contrast, and dark-field modality can be extracted from those coefficients.

Attenuation

The transmitted intensity of the stepping curve corresponds to its average value a_0. An object placed into the beam path reduces the transmitted intensity of the incident wave due to its attenuation. The transmission T is defined as

$$T = \frac{a_0^s}{a_0^r}. \tag{2.9}$$

Note that T is the same information that conventional radiography setups record. The attenuation is the loss of transmission signal strength and as such given as:

$$AT = -\log(T). \tag{2.10}$$

Differential Phase Shift

The differential phase shift can be calculated by subtracting the phase of the reference stepping curve from the sample stepping curve:

$$\phi = \phi^s - \phi^r, \tag{2.11}$$

with ϕ^s and ϕ^r being the phase of the intensity modulation. In this work, the differential phase shift will not be considered further.

Dark-field

As mentioned above, the dark-field signal is encoded in the loss of amplitude. The oscillation amplitude of the intensity modulation is called visibility V and given as:

$$V = \frac{I_{max} - I_{min}}{I_{max} + I_{min}} = \frac{a_1}{a_0}, \tag{2.12}$$

with I the recorded intensity from the stepping curve (see Equation 2.8). The relative decrease of visibility caused by small-angle scattering can be quantified by defining the normalized visibility V_{norm}:

$$V_{norm} = \frac{V^s}{V^r} = \frac{a_1^s a_0^r}{a_1^r a_0^s}. \tag{2.13}$$

For a homogeneous sample that does not induce small-angle scattering, the value remains constant at $V_{norm} = 1$, but for specimens which induce small-angle scattering, V_{norm} can be reduced up to 0. The dark-field signal DF, as it is referred to in this work, is the negative logarithm of the normalized visibility:

$$DF = -\log(V_{norm}). \tag{2.14}$$

For a comprehensive description of grating-based X-ray interferometry, the reader is referred to [De Marco, 2021].

2.2.4 Fringe Scanning

An alternative approach to sample the stepping curve (see Equation 2.8), called fringe scanning, was introduced by [Kottler, 2007]. With this approach, different relative positions between the frequency of the self-images and the grating bars of the G2 are obtained by slightly detuning the interferometer by introducing a deliberate deviation

from the ideal inter-grating distances or grating periods. Such a detuning results in a beat pattern, so-called moiré fringes at the detector. By placing an object at different locations, i.e., a different phase in this moiré pattern, different phase steps can be recorded. A continuous movement of the object over one or more full periods of the moiré pattern with according intensity measurements results in a full phase-stepping measurement. In this approach, either the sample can be moved through a fixed interferometer, or the interferometer can be moved around a stationary sample. For more information on fringe scanning, the reader is referred to [Koehler, 2015; De Marco, 2021].

2.2.5 Image Extraction

The different image signals, i.e., attenuation, dark-field, and phase contrast, are retrieved by a least-squares fit. The input data is generated via fringe scanning, thus by repeated acquisitions, while the moiré pattern is moved across the sample area.

The expected intensity, measured in one pixel of the detector in the k-th frame of in total N exposures, can be approximated via

$$I_k = T \cdot I_{0,k} \left(1 + V_{norm} \cdot V_{0,k} \cos(\phi + \Phi_{0,k})\right), \quad k = 1, .., N, \tag{2.15}$$

where T, V_{norm}, and ϕ correspond to the imaged object's transmission, normalized visibility reduction, and phase shift of the moiré fringe, respectively [Pfeiffer, 2008; Koehler, 2015]. Here, T and V_{norm} already include the normalization with their respective reference scan, according to Equations 2.9 and 2.13. $I_{0,k}$, $V_{0,k}$, and $\Phi_{0,k}$ correspond to the reference scan's mean intensity, mean visibility, and phase of the moiré fringe pattern.

2.3 Dosimetry

X-rays are a kind of ionizing radiation which cause cell damage to living tissue and organ damage. Exposure to ionizing radiation causes health effects that can be divided into two groups: deterministic effects and stochastic effects. Deterministic effects occur due to killing or malfunction of cells following high doses (i.e., severe skin reactions). In contrast, stochastic effects occur due to mutation of somatic cells (i.e., cancer) or reproductive cells (i.e., heritable diseases). Nevertheless, X-ray and other ionizing radiation enabled great advances in medical care, which justifies the exposure as long as the ALARA (=***A**s **L**ow **A**s **R**easonably **A**chievable*) principle is adhered. In this section, a brief introduction to different general dosimetric quantities is given.

2.3.1 Dosimetric Quantities

Here, different units used in dosimetry are introduced, along with corresponding measurement techniques. This section is mainly based on [Seltzer, 2011; Zoetelief, 2005; Le Heron, 1992; Nenot, 2009].

Kerma

Kerma K (= ***k****inetic* ***e****nergy* ***r****eleased per unit* ***ma****ss*) describes the first level of energy transfer of indirect ionizing radiation (photons, neutrons) and pertains the kinetic energy of the liberated charged particles. Kerma serves to approximate absorbed dose and is given as the quotient of $\mathrm{d}E_{tr}$ by $\mathrm{d}m$:

$$K = \frac{\mathrm{d}E_{tr}}{\mathrm{d}m}, \tag{2.16}$$

with $\mathrm{d}E_{tr}$ being the mean sum of the initial kinetic energies of all charged particles liberated in a mass $\mathrm{d}m$. The unit of kerma is $(\mathrm{J\,kg^{-1}})$ with the special name gray (Gy). For uncharged particles of a single energy, kerma is related to the fluence Ψ, indicating the energy carried by the X-ray beam, and the mass energy transfer coefficient $\frac{\mu_{tr}}{\rho}$ of the respective material via

$$K = \Psi \cdot \left(\frac{\mu_{tr}}{\rho}\right). \tag{2.17}$$

To achieve comparability in medical imaging, the respective material is set to air, therefore the kerma is expressed as air kerma, K_a, by

$$K_a = \Psi \cdot \left(\frac{\mu_{tr}}{\rho}\right)_a. \tag{2.18}$$

For polychromatic X-rays, a mean value of $\left(\frac{\mu_{tr}}{\rho}\right)_a$ should be used according to the energy distribution of the energy fluence.

Dose

When talking about patient dose, one has to differentiate between absorbed dose, equivalent dose, and effective dose:

Absorbed Dose

The absorbed dose D is the basic physical dose quantity and is defined as the quotient of the mean energy $\mathrm{d}\bar{\epsilon}$ imparted to a matter of mass $\mathrm{d}m$ by ionizing radiation:

$$D = \frac{\mathrm{d}\bar{\epsilon}}{\mathrm{d}m}. \tag{2.19}$$

Absorbed dose (physical units: $\mathrm{J\,kg^{-1}}$, or special name gray (Gy)) is a measurable quantity that is averaged over tissue volumes in practical protection applications. Under certain conditions (see [Zoetelief, 2005]), the kerma will be numerically equal to the absorbed dose.

Equivalent Dose

Equivalent (and later effective) dose is a risk-related quantity, meaning it is taken as an indicator of the probability of subsequent detriment. The equivalent dose H_T in body tissue or organ T, which takes into account the biological effectiveness of the kind and energy of radiation used, can be calculated from the absorbed dose via

$$H_T = \sum_R w_R \cdot D_R, \tag{2.20}$$

where w_R denotes the radiation weighting factors and D_R the absorbed dose. For X-rays, the radiation weighting factor is 1, independent of their energy [Le Heron, 1992; Nenot, 2009].

Effective Dose

The effective dose E is a calculated quantity that accounts for the radiosensitivity of the irradiated tissue. It is determined as a weighted sum from the equivalent dose H_T via

$$E = \sum_T w_T \cdot H_T = \sum_T \sum_R w_T w_R \cdot D_R, \tag{2.21}$$

using the tissue weighting factors w_T according to ICRP 103 [Nenot, 2009] with $\sum w_T = 1$, and summing over all exposed tissues. The physical units of both H_T and E are $\mathrm{J\,kg^{-1}}$ and have the special name sievert (Sv). Although the physical units of all dose quantities are the same, the unit Sv always indicates some kind of weighting.

Effective patient dose is a calculated quantity used to estimate potential detriment caused by exposure to ionizing radiation. The effective dose of a patient over the years determines his probability of developing stochastic effects, i.e., cancer and heritable effects [Nenot, 2009]. Such effects are understood to increase in probability in proportion to the radiation dose [Nenot, 2009]. Especially for medical radiological examinations, the potential risk is important to evaluate the cost-benefit relation of each examination. Further, the concept of effective dose serves to compare the risk of different diagnostic procedures for different body parts.

Note that the use of effective dose for quantifying medical exposure to patients has severe limitations. While it can be of value to compare e.g., the use of similar technologies, it can be problematic if the exposure is very heterogeneous or only applied to isolated organs or tissues [Nenot, 2009]. The absorbed dose in individual targets can be drastically higher than the effective dose for the whole body might indicate. Because of this reason, in mammography, the dose quantity mean glandular dose (MGD) is used instead of effective dose.

2.3.2 Operational Quantities

As the effective dose is a calculated quantity, operational quantities such as the surface entrance dose (SED) or the dose-area product (DAP) (or air kerma-area product (KAP), depending on the calibration) are used to assess the effective dose. These operational quantities are easily measurable for every examination and can be used to estimate the respective effective dose. Conversion coefficients are used to relate these operational quantities to effective dose [Zoetelief, 2005], and for standard examinations, these conversion coefficients can be found in literature [Wall, 2011].

Further, so-called Diagnostic Reference Levels (DRLs) are based on these operational quantities. Per recommendation of the International Commission of Radiological Protection (ICRP), DRLs serve to monitor dose distributions in diagnostic radiology and nuclear medicine [European Commision, 1999]. DRLs are not applicable to individual examinations but are rather set for groups of standardized patients. As X-rays as part of ionizing radiation are potentially harmful, exposure has to be supervised. DRLs are issued by the different states, often determined by the 75^{th} percentile of measured operational quantities for a large patient cohort, or phantom measurements. Therefore, DRLs are part of the regular quality assurance program.

In Germany, the DAP is used as operational quantity and thus the DRL is expressed in DAP for radiography [BfS, 2016; Schegerer, 2019]. Therefore, for the work presented in this thesis, DAP will be used instead of KAP. As mentioned above, the two quantities differ in the calibration of the ionization chamber. Nevertheless, the following definitions are given according to standard literature using the more commonly used

KAP.

2.3.3 Dose Measurement

A comprehensive overview of measurement methods for patient dosimetry can be found in [Zoetelief, 2005], Chapter 4. Here a shortened version of methods relevant to this work is included. Dose quantities can be measured either with ionization chambers or solid-state dosimeters.

The air kerma-area product (KAP), as well as the dose-area product (DAP), is obtained by integrating the air kerma K_a over the irradiated area of the X-ray beam perpendicular to the beam axis. If the air kerma (dose) is constant over the irradiated area, the KAP (DAP) becomes equal to the product of air kerma (dose) and the area. For diverging X-ray beams, the KAP (DAP) is constant along the beam path, as the kerma (dose) decreases with distance according to the inverse-square law, and the irradiated area increases accordingly.
The KAP (DAP) is measured with transmission ionization chambers [EC, 1997] and provides continuous monitoring of the output of the X-ray tube. It is measured on the central axis of the X-ray beam perpendicular to it at a specified distance from the focal spot.

Solid-state dosimeters, most often realized as thermoluminescent dosimeters (TLDs), are used to measure the locally absorbed dose. TLDs consist of materials that, after irradiation, emit electromagnetic waves in the visible regime when heated. Due to their small size, they can be used for dose measurements on patients or in phantoms.

2.4 Exposure Indices

While the section above deals with the measurement, calculation, and assessment of the radiation dose absorbed by an object, this quantity directly depends on the object's exposure. With old-fashioned film radiography, there is a direct proportion between the exposure of the image receptor and its optical density. For today's digital radiography, this does not hold true, therefore so-called exposure indices were introduced [IEC, 2008]. Although manufacturer-specific, these key figures are based on original image data and serve as a standard measure of the amount of exposure received by the image receptor.
A standardized Exposure Index (EI) serves to define directives, especially for the comparison of devices of different manufacturers [IEC, 2008]. The EI allows to estimate whether an image was taken at a suitable exposure level. EIs vary depending on the imaged body part, the projection, and the imaging system itself. However, resulting EI

deviate from the expected values, called target Exposure Index (EIT), mostly because of the non-ideal positioning of the patient and differences in beam quality compared to calibration conditions [Dave, 2018]. In order to quantify this deviation, the so-called deviation index (DI) is proposed. Regulations dictate that both the EI and the DI must be recorded [IEC, 2008].
Here, both EI and DI are introduced for the purposes of exposure control at the dark-field prototype, described in Chapter 5. For a comprehensive overview of exposure indices of digital radiography for medical purposes, the reader is referred to [IEC, 2008].

Exposure Index EI

At calibration conditions, the EI is a measure proportional to the signal level at the image receptor in a relevant image area, with the relevant image area depending on the examined body part. The EI is defined as

$$\mathrm{EI} = c_0 \cdot g(V), \tag{2.22}$$

with c_0 being a constant of $100\,\mu\mathrm{Gy}^{-1}$ and $g(V)$ a device-specific calibration function, which relates in principle the dose at the image receptor to the measured image values of the image receptor.

Deviation Index DI

The difference between the EI of an image and the EIT for that kind of examination is quantified with the DI given as [IEC, 2008]:

$$\mathrm{DI} = 10 \cdot \log_{10}\left(\frac{\mathrm{EI}}{\mathrm{EIT}}\right). \tag{2.23}$$

EITs are issued for different examinations by national medical associations. The DI is 0 if EI equals EIT and changes about ± 1 for every change of the EI of $+25\,\%/-20\,\%$ [IEC, 2008].

2.5 Medical Background

In this section, the structural properties of the human lungs are described based on [Tomashefski, 2008; Faller, 2020; GOLD, 2020], as the dark-field prototype of this

thesis is used for clinical thorax radiography. Due to their inherent structure, the lungs cause small-angle scattering to a great extent resulting in a strong dark-field signal. In conventional (attenuation-based) radiography, the signal of the air-filled lungs is superimposed by surrounding body parts such as the rib cage, heart, and soft tissue, impeding accurate diagnosis. Therefore, lungs are the most suitable use case for the application of the new X-ray dark-field image modality.

2.5.1 Lung structure

The respirator system is responsible for the gas exchange of oxygen and carbon dioxide between blood circulation and the surrounding air. The upper respiratory tract conducts the air toward the lungs. The lungs are divided into left and right lung, consisting of two and three lung lobes, respectively. The two main bronchi branch out into the entire lungs, with their diameter constantly declining with each rising branch generation. By breathing in, oxygen is transported via the bronchial structure to the functional units of the lungs. These gas-exchanging entities are the alveoli, little air sacs with a diameter of $150\,\mu m - 500\,\mu m$ that provide a total interface area of about $143\,m^2$. On the outside of the alveoli, the vascular capillaries transport the deoxygenized blood towards the gas exchange interfaces and the oxygenized blood back into the body. At the air-blood barrier of the alveoli, the exchange of oxygen in air and carbon dioxide in the blood occurs via diffusion. During exhalation, the carbon-dioxide-enriched air is exhaled.

2.5.2 Impairment through COPD and COVID-19

The alveolar surface can be reduced by different pathologies. In principle, this reduction can result from different effects: A destruction of the alveolar structure, its consolidation, or replacement. The different effects can be attributed to different diseases, and the first two (destruction and consolidation) are described in the following.

COPD

Chronic bronchitis and pulmonary emphysema are characterized by a pathological modification of the airways and alveoli, generally inducing impairments of the functional condition of the lung. Persistent respiratory symptoms and airflow limitations caused by these alveolar abnormalities define Chronic Obstructive Pulmonary Disease (COPD). These structural changes are caused by long-term exposure to noxious gases and particles, which induce chronic inflammation of the lung parenchyma. The destruction of the alveolar lung structure is an irreversible process, and the according

disease is called (pulmonary) emphysema. Pronounced emphysema considerably decreases the area of gas exchange in the lungs, resulting in persistent airflow limitations.

Being currently the third leading cause of death worldwide [WHO, 2021] and causing 6 % of all deaths globally, COPD is a major health challenge, yet preventable and treatable if discovered in early stages. Current diagnostic imaging methods either lack sensitivity (conventional radiography) [Pratt, 1987] or are associated with a rather high effective patient dose (CT) [Mettler, 2008].

COVID-19

Since the beginning of the year 2020, the pandemic caused by the new coronavirus SARS-CoV-2 has lead to a global medical, social, and economic crisis. The respective respiratory illness, Coronavirus Disease 2019 (COVID-19), caused a public shutdown in most parts of the world. Until March 2022, more than 6 million people died [JHU, 2022]. Apart from causing flu-like symptoms such as cough and fever, COVID-19 often affects the lungs. The so-called COVID-19-pneumonia usually affects both lungs and causes the lungs to become filled with fluid and inflamed, leading to breathing difficulties [Raptis, 2020]. Alveoli in the lungs consolidate, i.e., fill with fluid, therefore limiting their ability to take in oxygen and causing shortness of breath, cough, and other symptoms. Currently, alternative medical imaging methods for the assessment of pulmonary involvement in patients infected with COVID-19 are sought that combine a higher sensitivity than conventional (attenuation-based) chest radiography with a lower radiation dose than CT imaging.

Methods 3

In this chapter, the prototype system for clinical dark-field radiography is presented. Next, applied image corrections are introduced and described, which render the images used later in this thesis. In the end, a description of the patient studies that were ongoing during this thesis is provided.

3.1 Prototype System for Clinical Dark-field Chest Radiography

A thorough description of the dark-field radiography system, including its conception, technical implementation, and commissioning, can be found in [Frank, 2018; Willer, 2022]. Here, a summary of the most important features is provided.

The clinical dark-field chest radiography system was realized as a Talbot-Lau interferometer, as introduced in Chapter 2. Figure 3.1A depicts a schematic of the prototype system, and Figure 3.1B a photograph of Prof. Dr. Daniela Pfeiffer with a patient at the X-ray dark-field imaging device. The prototype consists of a clinical radiography system including a rotating anode X-ray tube (MRC 200 0508, *Royal Philips*, The Netherlands), a stationary collimator (R 302, *Ralco*, Italy) to restrict the field of view (FOV) to the examined region of the patient, an ionization chamber (Diamentor CI, *PTW*, Germany), and a flat-panel detector (PIXIUM 4343 F4, *Trixell*, France). In between these commercially available components, the three-grating interferometer is installed. Grating parameters are listed in Table 3.1. Due to the challenging fabrication process of X-ray gratings with large aspect ratios [Schröter, 2017; Mohr, 2012], the area of the G2, the largest grating, amounts to $6.5 \times 42\,\mathrm{cm}^2$. To achieve the coverage of the detector area in the horizontal direction, the G2 consists of six individual tiles stitched together [Meiser, 2016]. In order to extend the FOV vertically, we adapted a scanning image acquisition [Kottler, 2007; Koehler, 2015] by moving the interferometer upwards across the patient's thorax, also described in Section 2.2. A linear stage (AKD-P00306-NBEID000, *Kollmorgen*, Germany) placed behind the detector enables the movement. By doing so, we extend the FOV to $37 \times 37\,\mathrm{cm}^2$ in the patient plane,

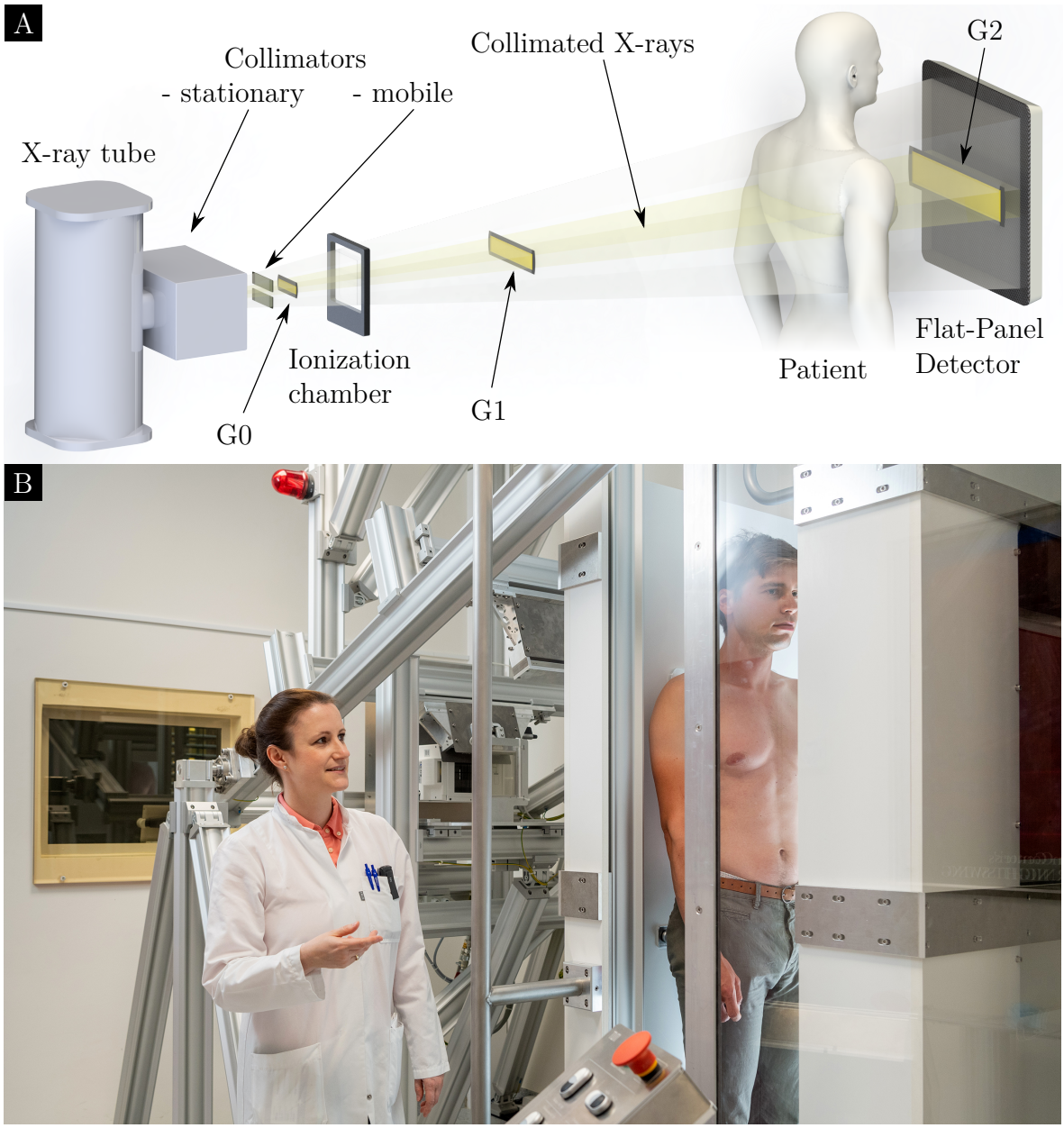

Figure 3.1: Schematic and photograph of the clinical dark-field prototype system. A, Rendering of main technical components of the prototype system. The prototype consists of a clinical radiography setup (X-ray source, stationary collimator, ionization chamber, flat-panel detector) combined with a Talbot-Lau interferometer (G0, G1, G2). The mobile collimator restricts the illuminated area to the gratings. The ionization chamber records the DAP for each image acquisition. B, photograph of Prof. Dr. Pfeiffer with a patient at the X-ray dark-field system. Copyright of photograph by © Andreas Heddergott / TUM.

suitable for human chest imaging.
The image acquisition time amounts to about 7 sec, depending on the total illuminated FOV set by medical staff with the stationary collimator. During image acquisition, the tube operates in pulsed mode at a frame rate of 30 Hz. This results in a local illumination time of 0.87 sec, or about 24 illuminated frames. To achieve the read-out time, a 3 x 3 binning is applied to the detector, reducing the nominal pixel size of $148 \times 148\,\mu m^2$ to a pixel size of $444 \times 444\,\mu m^2$. The X-ray window of each pulse amounts to 17 ms. In contrast to conventional chest radiography, which is carried out at a tube voltage of 125 kV, the tube voltage at the dark-field system is set to 70 kV. This tube voltage proved to produce both attenuation and dark-field images with good quality [Sauter, 2021]. The available tube currents range from 10 mA–930 mA, and are adapted to each patient as later described in Chapter 5.

	G0	G1	G2
Grating type	absorption	phase (π) shifting	absorption
Period / µGy	7.725	10.144	14.766
Duty cycle	0.7	0.5	0.5
Gold height / µGy	280	9.21	250
Substrate	1.0 mm graphite	0.2 mm glass (CrAu)	1.0 mm graphite

Table 3.1: Grating parameters of interferometer implemented in the clinical dark-field prototype system. The specifications are listed as provided by industrial collaborator (*Royal Philips*, The Netherlands).

The technical implementation of the used setup predetermines the structure of the acquired data and the resulting image extraction. A detailed description of the exact approach used for the image acquisition with the dark-field prototype of this thesis can be found in [Willer, 2022].

3.2 Image Corrections

At the clinical dark-field system, a series of corrections are applied to the retrieved images. Here we differentiate between processing, which conducts phase retrieval on raw intensities that are subject to change due to corrections, and postprocessing, which is then applied to the retrieved images. Figure 3.2 depicts the raw (A, D), processed (B, E), and postprocessed (C, F) images, with the dark-field images in the upper row (A, B, C) and the attenuation images in the lower row (D, E, F).

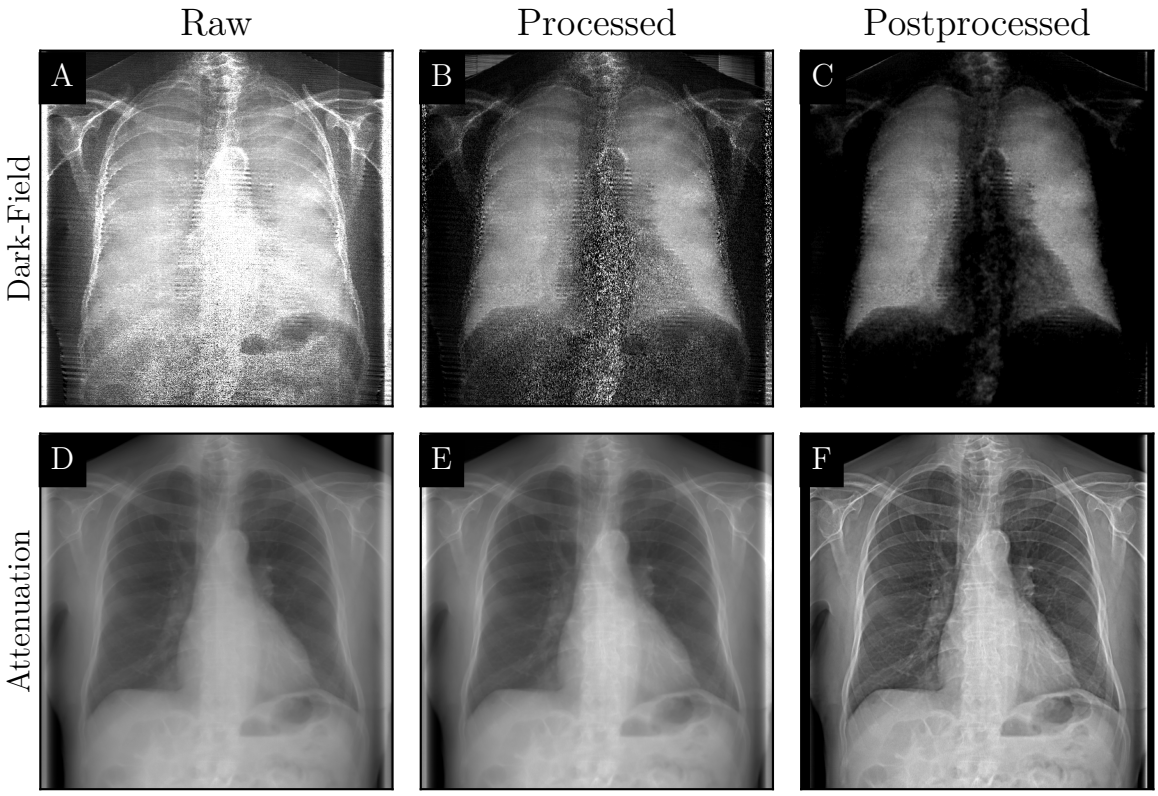

Figure 3.2: Processing steps for images obtained with clinical prototype system. Dark-field (A-C) and attenuation (D-F) images at different processing steps. Raw (A, D), processed (B, E), and postprocessed (C, F) images are depicted for an exemplary subject. The final dark-field image (C) contains only true signal originating from small-angle scatter at the lungs' microstructure. In the final attenuation image (F), contrast is enhanced at the cost of losing quantitative information. Dark-field and attenuation images are perfectly registered as they are retrieved from the raw data set.

Processing

Due to the continuous movement of the grating interferometer at a speed of $87\,\mathrm{mm\,s^{-1}}$ during the pulsed image acquisition at 30 Hz, and the illuminated slit with dimensions of $6.5 \times 42\,\mathrm{cm^2}$, each pixel is illuminated for about 0.8 s. During this time, sample movement, such as the heartbeat, cannot always be avoided. Schick et al. implemented a **motion artifact correction** based on virtually narrowed slots to replace motion-afflicted pixels by reconstructed virtual slots with small χ-squared values [Schick, 2022].

A bias occurs in the calculation of visibility maps in grating-based phase-contrast and dark-field imaging. With decreasing signal-to-noise ratio (SNR), the calculated visibility increasingly deviates from its true value [Chabior, 2011]. Therefore, a **bias correction** method is applied in image areas with a low SNR that takes into account the signal of adjacent pixels with a specific weight, thus increasing the signal.

If a patient's thorax is smaller than the whole FOV, the stationary collimator is set to restrict the illumination to the desired FOV. Due to an extended focal spot size of the X-ray tube and a finite/non-negligible collimator blade thickness, we see a gradient in the raw intensities. The **collimation shadow** originates from photons from the outer positions of the focal spot that are not completely absorbed by the collimator blades as they travel at an angle and penetrate only a small fraction of them. We estimate the according intensity gradient and correct for it in the raw intensity data.

The rotation of the interferometer around the focal spot size introduces **mechanical vibrations** into the interferometer. Although the damping elements between drive and interferometer and the installed counterweights dampen these vibrations, there are still vibrations that result in streak artifacts in the reconstructed images. Noichl et al implemented a correction algorithm to estimate these vibrations and subsequently remove their artifacts [Noichl, 2022].

As the G2 grating consists of several tiles stitched together (as described in Section 3.1), there are **stitching lines** visible in the raw data yielding a high intensity due to a lack of grating coverage. In the attenuation image, corresponding lines are eliminated by the normalization with the reference data if the intensity is within the detector's linear response regime. In the dark-field image, however, the signal is corrupted due to the lack of grating coverage. In order to obtain a continuous image across the stitching gaps, affected pixels in both images are replaced by an interpolation of the neighboring pixels.

Optical and X-ray scatter occurring anywhere within the imaging system can distort the image information. Different processes, such as sample (Compton) scatter, scatter at the grating G2, and detector scatter, lead to measured intensities that superimpose the recorded intensity pattern. This superposition results in a reduced contrast of the stepping curve and therefore increased dark-field signal. A correction for Compton

scatter induced dark-field is implemented based on measured attenuation and Monte-Carlo simulations adapted from the Skyflow Software (Royal Philips, The Netherlands) [Bertram, 2007; Mentrup, 2014; Mentrup, 2016] for setup-specific parameters. G2 scatter and optical scatter in the detector are corrected by subtracting intensity- and process-dependent scatter kernels from the recorded intensities [Urban, in Review].

Postprocessing

Beam hardening artifacts in dark-field images occur when the X-ray spectrum is changed due to absorption, as the measured visibility in a grating-based X-ray interferometer depends on the X-rays' energy. This is because the gratings' attenuation and phase-shifting properties differ for different photon energies, as well as the self-imaging distances. The measured visibility in a polychromatic setup is a weighted average of the photon energy-dependent visibility. We implemented a correction based on polyoxymethylene (POM) and aluminum, as their spectral absorptions are similar to the one of soft tissue and bones, respectively. For different thicknesses of absorber material, we measured the beam hardening induced visibility change and therefore pseudo dark-field signal in each detector pixel. Assuming the attenuation is caused by POM and aluminum in equal parts, we calculate the beam hardening induced dark-field signal pixelwise, and subtract it from the measured dark-field signal.

To obtain a uniform noise variance in the dark-field image independent of the object's local attenuation, an adaptive/regularized **denoising** algorithm is applied that was developed at the chair this PhD project was conducted.

In conventional radiography, attenuation radiographs are postprocessed in order to facilitate diagnosis. Postprocessing steps include both **contrast enhancement** and **histogram equalization**. The former approach suppresses the high frequency bands of a Laplacian pyramid containing mostly uncorrelated noise. The latter algorithm changes the relationship between attenuation and gray values to an S-shaped curve, effectively matching the dynamic range of gray values to diagnostically relevant attenuation values. Both algorithms are implemented for the attenuation images obtained from the clinical dark-field prototype in a way to match best commercially available software (in our case UNIQUE, *Royal Philips, The Netherlands*, employed at the reference device Digital Diagnost (DiDi)).

In the end, **background masks** are applied to both image modalities in order to blacken the background. A black background is standard in conventional attenuation-based radiography, corresponding to image areas without a sample in the beam path. Also, black relates to no signal in the dark-field image for standard windowing. Thus the background correction serves to highlight only visibility reduction due to small-angle scattering of X-rays in the lung structure. At the clinical dark-field prototype

system, this postprocessing step is necessary as the detector signal often saturates in sample-free areas, therefore the recorded intensity values deviate from expectations. The deviation from expected pixel values in the background results in a calculated visibility reduction that manifests in the dark-field signal.

3.3 Patient Studies

In this thesis, the participants of two patient studies were included, one on COPD and one on COVID-19-pneumonia. Further patient studies are planned and have already started during this PhD project. Nevertheless, as they play no part in this thesis, they are not described here. Purpose, inclusion criteria, and participant inclusion of the first two studies are described in the following.

3.3.1 Early Detection of COPD

Since October 2018, the first patient study on early detection of Chronic Obstructive Pulmonary Disease (COPD) has been conducted using the dark-field radiography prototype system at a clinical site (*Klinikum rechts der Isar*, TUM, Munich, Germany). The study was conducted per the Declaration of Helsinki and was approved by both the institutional review board and the national radiation protection agency (approval Z5 – 22462/2 – 2017-021). Up to 500 patients will be included, both without any lung disorders and with varying degrees of COPD. Every patient is imaged at our dark-field chest radiography setup in inspiration and expiration in posterior-anterior (pa) and lateral (lat) orientation. Additionally, the study includes a conventional thorax radiograph as a reference, as well as a whole-body plethysmography and a COPD assessment test. Patients older than 20 years, 150 cm – 182 cm in height, and with a body mass index (BMI) of less than 38 kg/m^2 are eligible.
There are two study arms in which patients are approached: In the first arm, which comprises about 80 % of the patient cohort, patients were approached after undergoing medically indicated chest CT with a contrast agent that showed no anomalies in the lung parenchyma other than emphysema. Patients in the second arm were approached by the institute of pneumology after their medical check-up regarding COPD or emphysema. These patients, which are usually in an advanced stage of COPD, did not undergo a chest CT. All patients gave written informed consent prior to participation.

3.3.2 Diagnosis of Pulmonary Alterations with COVID-19

Approval 1

In a second study starting in May 2020, we investigated dark-field radiography's potential for the detection of pulmonary alterations in accordance with COVID-19. Patients of legal age that underwent chest CT at our institution as part of their diagnostic workup and had a clinically suspected COVID-19 infection were screened for study participation. The study was conducted in accordance with the Declaration of Helsinki and was approved by both the institutional review board and the national radiation protection agency (approval Z5 – 22464/2020-047-G). A total of 60 patients were included in the study.
Only patients with a CO-RADS category 4 (suspicious for COVID-19), 5 (typical for COVID-19), or 6 (Reverse Transcription Polymerase Chain Reaction (RT-PCR) positive for COVID-19, if patients had been tested before the CT scan) as defined by Prokop et al. [Prokop, 2020] were included in this study. Other inclusion criteria were the ability to consent, to stand upright without help, and to hold breath for 7 s. Eligible patients were approached right after the CT scan, and dark-field imaging was conducted within 24 h after the CT scan. Exclusion criteria were a negative RT-PCR test within two days before the CT scan, pregnancy, lung cancer, and pneumothorax. Further eligibility criteria was a height between 150 cm − 182 cm and a BMI of less than 38 kg/m^2. All patients underwent RT-PCR assay for Severe Acute Respiratory Syndrome Coronavirus 2 (SARS-CoV-2)-infection within 48 hours before and 48 hours after the CT scan.

Approval 2

Starting March 2021, up to 140 patients of legal age are included in a continuation study to investigate the correlation of severity of COVID-19 induced pulmonary alterations in dark-field chest radiography and computed tomography (CT). The study is conducted in accordance with the Declaration of Helsinki and was approved by both the institutional review board and the national radiation protection agency (approval Z5 – 22464/2021-004-G). The inclusion process, as well as eligibility and exclusion criteria, are the same as for the first 60 patients. At the time of writing, this study is still ongoing.

Dosimetry at Clinical Dark-Field Prototype 4

The findings presented here have previously been published in the article "Dosimetry on First Clinical Dark-Field Chest Radiography" by Frank et al. [Frank, 2021]. Compared to this work, the figures and some wordings have been slightly modified, and further information about lateral examinations was provided. Finally, the technical introduction to dark-field imaging and dosimetry, as well as the used setup, have been omitted. The reader is instead referred to Chapters 2 and 3 for this information.

4.1 Motivation

Dosimetry is the metrology of interactions of ionizing radiation with matter. Its purposes in radiologic diagnostics are in particular the determination of the radiation exposure of patients and the acquisition of monitoring data for radiological protection to determine whether specific examinations comply with dose limits [Schlegel, 2002]. Recently, we successfully developed and commissioned the first clinical X-ray dark-field chest radiography system [Willer, 2021; Frank, 2018], which is described in Section 3.1. Currently, first patient studies are ongoing with the aim of evaluating the diagnostic potential of dark-field chest radiography for different lung diseases. Part of the comprehensive evaluation process is the risk assessment for the imaged individual. Here, we report on dosimetry performed to estimate effective dose values for the first patient study and the evaluation of monitoring data to determine if we comply with dose limits and thus can justify the examination.

4.2 Methods

Equivalent dose and effective dose values are calculated quantities that depend highly on the exposed body and are not measurable in practice. Therefore, so-called operational quantities are used to assess these dose values [Nenot, 2009] (see also Section 2.3).

In radiography, both the entrance surface dose and the dose-area product (DAP) are used as operational quantities. They are used to monitor dose distributions in diagnostic radiology and nuclear medicine [European Commision, 1999]. For retrospective dose assessment, the International Commission of Radiological Protection (ICRP) recommends the use of Diagnostic Reference Levels (DRLs) [European Commision, 1999]. In clinical practice, the use of DAP for DRL is recommended [European Commision, 1999] and, more importantly for our study, it is used in Germany [Schegerer, 2014; Schegerer, 2019]. The effective dose E of a given examination depends linearly on its DRL and conversion coefficients for standard procedures can be found in literature [Wall, 2011; Schegerer, 2019].

Dark-field radiography is not a standard procedure, therefore literature values can not be applied. Furthermore, at 70 kV we use a tube voltage lower than the typically used 125 kV in conventional thorax radiography [Saure, 2008]. In order to determine a conversion coefficient correlating DAP to E for the clinical dark-field prototype, we conducted measurements in cooperation with the Bundesamt für Strahlenschutz (*Federal Office for Radiation Protection*) (BfS) using a male anthropomorphic phantom that models the reference person according to ICRP 23 [Richmond, 1985] (ATOM® Dosimetry Verification Phantoms Model 701, *CIRS Inc., Norfolk, USA*, see Figure 4.1). The phantom's thorax measures $23 \times 32\,\mathrm{cm}^2$, which translates to a body height of 173 cm, and represents a person weighing 73 kg, resulting in a BMI of $24.4\,\mathrm{kg/m}^2$. It consists of several slabs of epoxy resins, imitating both absorption and Compton scattering properties of the human body. There are drill holes distributed on a $3 \times 3\,\mathrm{cm}^2$ grid in each slab, filled with tissue-equivalent pins that can additionally be equipped with TLDs to measure the locally absorbed dose. Figure 4.1 depicts photographs of the phantom in frontal view (A), one slab, filled with several TLDs, in cross-sectional view (B), and the phantom in lateral view (C).

Absorbed doses were measured inside and at the surface of the phantom with rods (size, 1 mm x 1 mm 6 mm) and chips (size, 3.2 mm x 3.2 mm x 0.9 mm) of lithium fluoride LiF:Mg. Ti (TLD-100, *Bicron-Harshaw, Cleveland, USA*). The TLDs were calibrated in air and corrected to absorbed dose to water, using conventional X-ray equipment (*Seifert, ISOVOLT 420*) at a tube-TLD distance of 2 m. The tube potential and filtration were chosen according to the settings of the X-ray tube at the examination to approximate the radiation quality of the corresponding examination. In the case of the dark-field examination, calibration was performed at 70 kV with a total filtration of 10 mm aluminum, taking into account the medical components as well as the gratings.

Individual calibration, annealing, and read-out of the TLDs were performed following standard procedures [Zoetelief, 2002] and described in detail by Lechel et al. [Lechel, 2009]. The combined uncertainty for a single TLD dose measurement was estimated to be 9 % [Lechel, 2009]. The organ doses were calculated according to the recommen-

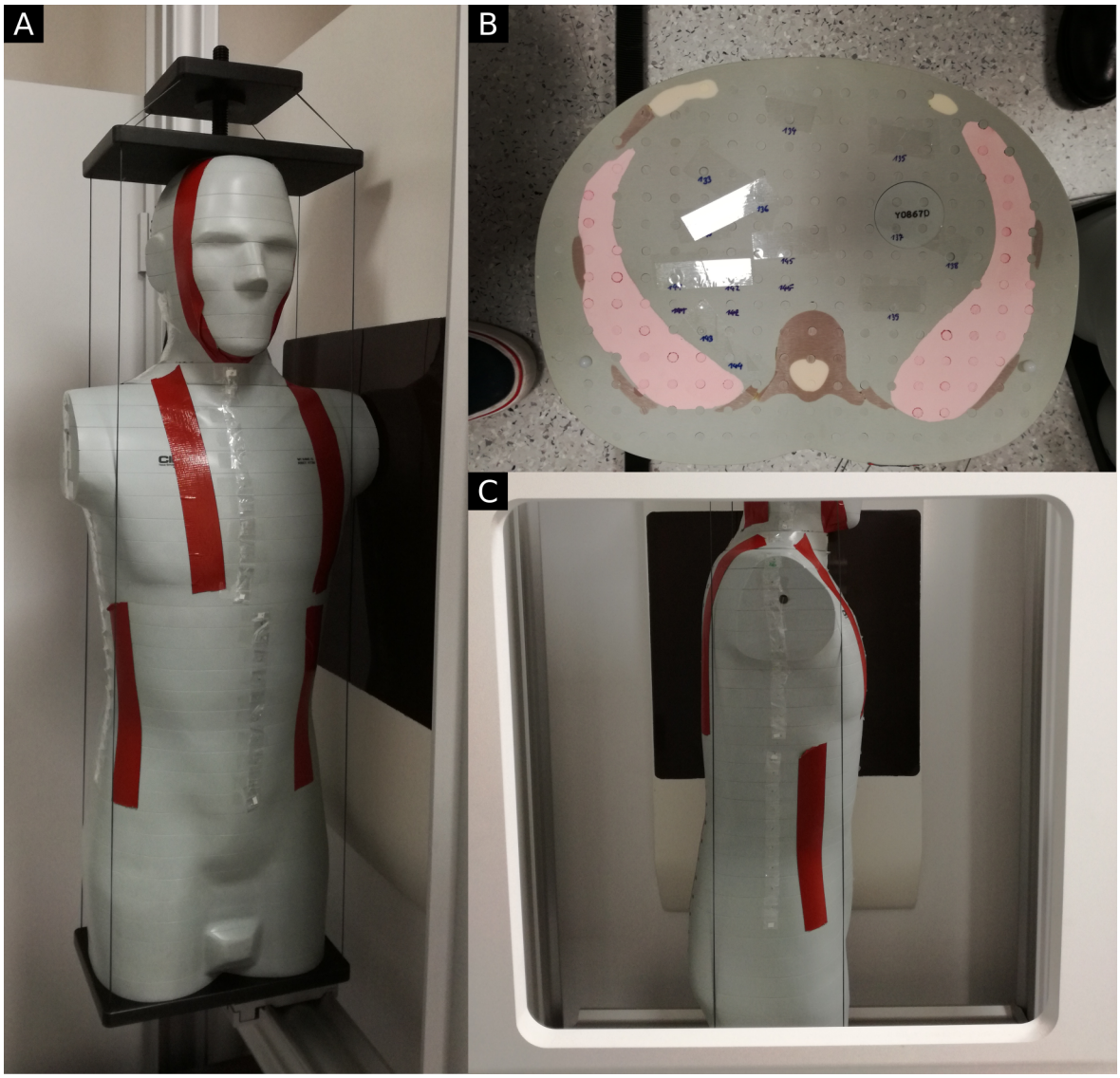

Figure 4.1: Photographs of the male anthropomorphic ATOM phantom. A, frontal view, B, cross-sectional view of one slab, and C, lateral view of phantom used to model a reference person according to ICRP 89 [Valentin, 2002] for quantitative dosimetry. In each phantom slab there are drill holes in which additional thermoluminescent dosimeters can be inserted in order to measure the locally absorbed dose at different anatomical locations. Figure adapted from [Frank, 2021].

dations of the manufacturer's user manual for this phantom. The effective dose was calculated from the tissue and organ equivalent doses using the tissue-weighting factors given in ICRP publication 103 [Nenot, 2009].

For our measurements, the phantom was equipped with around 200 TLDs, distributed at the surface and in the interior of the phantom. The number and location of the TLDs ensure that the absorbed dose is measured at all locations of radiosensitive tissue and organs of the human body. If the spatial extent of an organ was covered by more than a single TLD, the locally absorbed dose was calculated via the manufacturer's specifications.

To estimate conversion coefficients at the dark-field prototype, we took two separate measurements, one in which the phantom was positioned within the imaging system in posterior-anterior (pa) orientation and one in lateral (lat) orientation. Using a tube voltage of 70 kVp, 30 consecutive exposures were conducted at high tube power, and DAP was recorded for each exposure with the installed ionization chamber. The here applied high tube power was determined by the highest possible power at that time, which was during construction. The repeated exposure ensured a sufficiently high absorbed dose in every TLD within the entire phantom to minimize statistical error. Similarly, we repeated the TLD measurement at the clinical reference device (Digital Diagnost (DiDi), *Philips, The Netherlands*). Here, we used the standard thorax pa routine after positioning the phantom accordingly. Again, 30 consecutive scans ensured a sufficiently high absorbed dose. As a separate TLD readout process is necessary for each device and orientation, these measurements were conducted over the course of several weeks. Since the anatomical location of every TLD is known, the correct tissue weighting factor is applied for each radiosensitive tissue and organ to determine the effective dose as outlined in Section 2.3.

From the recorded DAP values and calculated effective dose E collected with the TLD measurements described above, we obtain a conversion coefficient as follows:

$$C = \frac{E/\mu\mathrm{Sv}}{\mathrm{DAP}_{\mathrm{measured}}/\mu\mathrm{Gy\,m^2}}. \tag{4.1}$$

This conversion coefficient C (physical units: $\mu\mathrm{Sv}/(\mu\mathrm{Gy\,m^2})$) can be used for every measurement with the respective system at the used tube voltage (70 kV for the dark-field prototype system, 125 kV at the clinical reference device). A combined uncertainty of up to 10 % for the measurement was assumed, taking into account both TLD and ionization chamber uncertainties [Lechel, 2009].

For clinical dark-field radiography as a novel imaging technique, there is no DRL. Nevertheless, after conducting the measurements described above, the BfS assigned a reference level of $\mathrm{DAP}_{\mathrm{reference,\,pa}} = 30\,\mu\mathrm{Gy\,m^2}$ ($\mathrm{DAP}_{\mathrm{reference,\,lat}} = 80\,\mu\mathrm{Gy\,m^2}$) for pa (lat) examinations to our prototype system. This reference level is only applicable to dark-

field imaging carried out with the described imaging system located at the clinical site *Klinikum rechts der Isar* in Munich. It is a quantity that can be exceeded for individual examinations as long as the measured mean value for a given patient collective is below the specified reference level, similar to DRLs [ICRP, 1997; Schegerer, 2019].

In order to determine the average effective patient dose, the male anthropomorphic ATOM phantom modeling the standardized adult man was imaged again at the dark-field prototype without TLDs. In contrast to the TLD measurements, this time, the tube settings were adapted for an actual patient examination, not for high power output. Using the conversion coefficient determined in Equation 4.1, the effective dose was obtained from the DAP value of this acquisition.

4.3 Deposited Dose in Phantom and Conversion Coefficients

The distribution of deposited dose in the anthropomorphic phantom for pa examinations at the dark-field prototype system is listed in Table 4.1 and Table 4.2. The first columns contain the different radiosensitive organs and tissues of the human body (Table 4.1) and remainder tissue (Table 4.2), the second the respective tissue weighting factors w_T according to ICRP 103 [Nenot, 2009], and the third and fourth columns list the equivalent dose H_T. The values in the third column correspond to the measured dose deposited into the phantom averaged over 30 scans at an increased tube power. The equivalent doses of an actual patient scan, obtained by scaling the measurements to the actual reference patient dose, are listed in the fourth column.

The highest fraction of equivalent dose was deposited in the lung, followed by remainder tissue, similar to conventional thorax radiography [Jones, 1985; Huda, 1989]. For the phantom measurements at an increased tube power, the calculated effective dose amounts to 44.3 µSv at a DAP of 29.7 µGy m^2, which yields the conversion coefficient $C = 1.5\,\mu\text{Sv}/(\mu\text{Gy}\,\text{m}^2)$ with a reported uncertainty of up to 10 % [Lechel, 2009]. This conversion coefficient is now used for calculation of effective patient doses in pa orientation.

A through-out investigation of the equivalent dose of each radiosensitive organ and tissue was only carried out by the BfS for pa and lat examinations at the dark-field prototype and for pa examinations at the commercial DiDi used for reference in the first COPD study. Only the exact values for pa examinations at the dark-field prototype as presented were provided by the BfS. Nevertheless, the resulting effective dose for all three examinations at a respective DAP were provided, for which we could then determine a conversion coefficient. All determined conversion coefficients are listed in Table 4.3.

Organ	Weighting factor w_T	Equivalent Dose, measured / µSv	Equivalent Dose, scaled / µSv
Gonads	0.08	0.7	0.6
Red bone marrow	0.12	38.1	30.5
Colon	0.12	2.9	2.3
Lung	0.12	138.5	110.8
Stomach	0.12	30.6	24.5
Bladder	0.04	2.1	1.7
Breasts	0.12	63.4	50.7
Liver	0.04	49.7	39.8
Esophagus	0.04	65.6	52.5
Thyroid	0.04	25.7	20.6
Skin	0.01	31.7	25.4
Bone surface	0.01	26.3	21.0
Salivary glands	0.01	3.9	3.1
Brain	0.01	8.2	6.4

Table 4.1: Radiosensitive organs of the male anthropomorphic phantom with tissue weighting factors according to ICRP 103 [Nenot, 2009] and equivalent dose. The two columns giving equivalent dose differ in such as the values in the first column are obtained from reference measurements with increased tube power, while the values in the second column are scaled to represent the actual dose for a patient scan.

Remainder tissue	Weighting factor w_T	Equivalent Dose, measured / µSv	Equivalent Dose, scaled / µSv
Small intestine	0.12	2.9	2.3
Kidney		86.0	76.8
Adrenal		119.5	95.6
Spleen		94.5	75.6
Pancreas		48.0	38.4
Thymus		40.3	32.2
Gall bladder		17.8	14.2
Oral mucosa		5.0	4.0
Heart		48.0	38.4
ET-region		4	3
Prostate		1.4	1.2
Lymph nodes		36	29
Muscle		36	29

Table 4.2: Remainder tissue of the male anthropomorphic phantom with tissue weighting factor according to ICRP 103 [Nenot, 2009] and equivalent dose. The two columns giving equivalent dose differ in such as the values in the first column are obtained from reference measurements with increased tube power, while the values in the second column are scaled to represent the actual dose for a patient scan. Note that the effective dose of remainder tissue is calculated as the arithmetic mean of the 13 different tissues [Nenot, 2009].

Setup, Orientation	Measured DAP / µGy m²	Effective Dose / µSv	Conversion Coefficient / µSv/(µGy m²)
Dark-field Scanner, pa	29.7	44.3	1.5
Dark-field Scanner, lat	24.5	46.4	1.9
DiDi	8.57	17.6	2.1

Table 4.3: Measured DAP and calculated effective dose values from calibration measurements conducted in cooperation with BfS, along with retrieved conversion coefficient.

4.4 Effective Dose Values

4.4.1 Effective Dose Values for the Reference Person

The effective dose imparted to the reference person for one examination at the dark-field prototype was determined by adapting the tube settings to the anthropomorphic ATOM phantom modeling the reference person. Here, we measured a DAP of 23.4 µGy m^2, which amounts to an effective dose of $E = 35.1$ µSv, using the previously determined conversion coefficient. This value is the effective dose for the reference person for one examination in *pa* orientation. Therefore, the equivalent dose values in the last column of Tables 4.1 and 4.2 are scaled by the factor 35.1 µSv/44.3 µSv = 0.80 to adapt from high tube output to patient-adapted output. The effective dose values for the reference person [Richmond, 1985] for pa examinations at the dark-field scanner and the commercial DiDi system are listed in Table 4.4.

Setup	Effective Dose / µSv
Dark-field Scanner, pa	35.1
DiDi, pa	17.6

Table 4.4: Effective dose values for the reference person [Richmond, 1985] for pa examinations at the dark-field prototype and the commercial DiDi system.

4.4.2 Effective Dose Values for Patient Collective

For the evaluation presented here, we considered n = 92 patients of which 37 were female and 55 were male, with an average age of (63.7 ± 11.8) years and an average BMI of

$(25.5 \pm 4.6)\,\mathrm{kg\,m^{-2}}$. Here, values are given as (mean value ± standard deviation). Figure 4.2 depicts the histogram of the measured DAP values and calculated effective doses for these patients. The data include radiographs in pa (Figure 4.2A) and lat (Figure 4.2B) orientation in both inspiration and expiration. Our reference level of $\mathrm{DAP}_{\mathrm{reference,pa}} = 30\,\mu\mathrm{Gy\,m^2}$ for pa examinations, corresponding to an effective dose of $E_{\mathrm{reference,pa}} = 45\,\mu\mathrm{Sv}$, is indicated with a solid blue line in Figure 4.2A. The respective reference level $\mathrm{DAP}_{\mathrm{reference,lat}} = 80\,\mu\mathrm{Gy\,m^2}$ for lat orientation, corresponding to an effective dose of $E_{\mathrm{reference,lat}} = 152\,\mu\mathrm{Sv}$, is out of axis in Figure 4.2B.

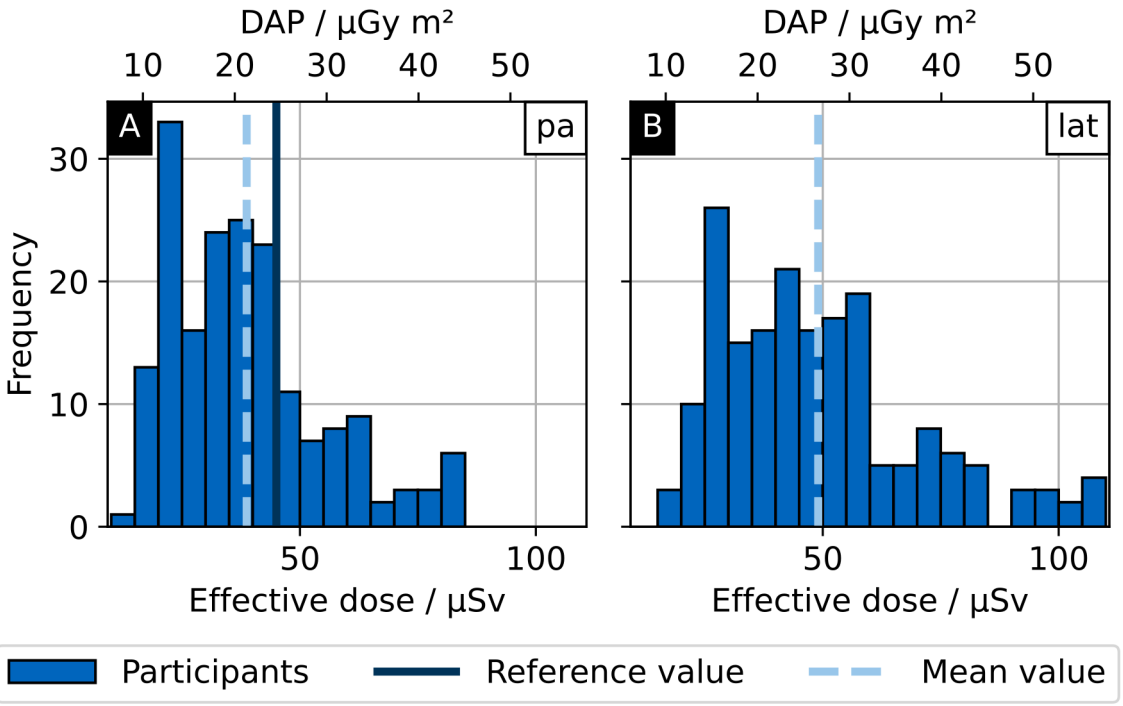

Figure 4.2: Histogram of measured DAP values and corresponding effective dose values for examinations in both inspiration and expiration of 92 patients. A, examinations in pa and B, in lat orientation. The solid blue line indicates the reference value and the dashed line the mean value. In B, the reference value is at $80\,\mu\mathrm{Gy\,m^2}$ and therefore out of axis. For both orientations, the mean DAP value is below the reference value.

The mean DAP for this patient collective is $(25.8 \pm 10.9)\,\mu\mathrm{Gy\,m^2}$ for pa and $(25.8 \pm 10.9)\,\mu\mathrm{Gy\,m^2}$ for lat examinations (dashed lines in Figure 4.2A and Figure 4.2B, respectively). The corresponding mean effective doses for the patient collective are $(38.7 \pm 16.4)\,\mu\mathrm{Sv}$ and $(49.0 \pm 20.8)\,\mu\mathrm{Sv}$, respectively. In addition, for pa examinations we find a median effective dose of 35.7 µSv, a 95th percentile value of 74.8 µSv, and a fifth percentile value of 18.4 µSv. For lat examinations, we find a median effective dose of 45.3 µSv, a 95th percentile value of 94.8 µSv, and a fifth percentile value of 23.3 µSv. The mean

DAP values are below the reference values for both pa and lat examinations for the examined patient collective.

4.5 Discussion

Determination of Effective Doses for Lateral Examinations

To determine the effective dose for the reference person in lat orientation at the dark-field prototype system, a phantom that represents the reference person has to be imaged at the dark-field system with appropriate exposure settings and correct anatomical collimation. With the respective conversion coefficient listed in Table 4.3, the effective dose can be calculated from the measured DAP value. No such phantom was available, therefore for the time being, no reference effective dose for lat examinations at the dark-field system could be determined.

Comparison to Literature Values

As mentioned above, there is an uncertainty of about 10 % arising from TLD calibration and readout [Lechel, 2009]. Compared to the literature value for conventional thorax imaging for pa orientations of $C = 1.6\,\mu Sv/(\mu Gy\,m^2)$ [Wall, 2011], the measured value at the commercial system of $2.1\,\mu Sv/(\mu Gy\,m^2)$ is increased by 30 %. The conversion coefficient for pa dark-field imaging, on the other hand, agrees within uncertainty to the reported literature value for conventional radiography, although the X-ray spectrum differs due to different maximal tube voltages and filtration, such as the gratings in the dark-field prototype. The calculated conversion coefficient for lat examinations is lower than for pa examinations, contrary to literature [Wall, 2011].

These observations demonstrate the need for the estimation of a conversion coefficient for each system separately. Thanks to these measurements, we have an excellent understanding of effective dose values at the two systems included in our patient study on COPD. Although there are deviations from literature values, one has to keep in mind that reported values vary greatly depending on equipment and should be used for estimation purposes only [Mettler, 2008].

Applicability of Measured Dose Values to Living Participants

The conversion coefficients are determined for the reference person defined by ICRP 23 [Richmond, 1985] and, therefore, only correct for patients with standard measures. The exact values of equivalent dose measured in each radiosensitive organ or tissue as listed

in Table 4.1 and Table 4.2 are also only true for the reference person. For patients with body proportions deviating from standard measures, neither equivalent dose values nor conversion coefficients hold true. Further, the values are not completely transferable to women, as breast tissue and female reproductive organs are not modeled. The consequent calculation of effective dose is only an approximation to estimate potential detriment [Mettler, 2008].
To estimate the effective dose more precisely for body types deviating from standard measures of the reference man, a Monte-Carlo simulation would have to be conducted. Only with the correct spectrum with all filters, correct distances, and correct anatomical models the equivalent dose values in each radiosensitive organ and tissue can be simulated. From there, effective dose values for different body types can be calculated. For an overview of organ doses for different spectra and examinations, obtained from Monte-Carlo simulations, the reader is referred to Drexler et al. [Drexler, 1993].

Low DAP Values for lat Examinations

For the lat examinations, all measured DAP values are far below the DRL, although the exposure is generally increased for lat examinations, as a considerably higher fraction of the initial radiation is attenuated. One reason is the narrower irradiated area compared to pa orientation. Further, due to power limitations of the X-ray source, the exposure is generally below what is necessary to achieve the target detector dose (see Chapter 5). The combination of those two factors results in comparably small DAP values. If the exposure was adequate for lat examinations in order to reach the target detector dose, the resulting DAP values would increase. A corresponding evaluation would be necessary once the exposure control settings are adapted.

Distribution for Patient Collective

The broad distribution of measured DAP values in the patient collective is caused by the varying body types and sizes of the patient collective. To ensure a constant dose in the detector plane, the tube current is adapted to the patient (see also Chapter 5). Therefore, heavier patients receive more dose compared to lighter ones [Yanch, 2009] for two reasons: they absorb a higher percentage of the initial dose as the length of the beam path within the body is usually increased, and also they are exposed to more initial dose due to the increased tube current. The deviation between measured DAP of the reference person and mean DAP of the examined patient collective for pa examinations is also caused by the difference in patient size. The BMI of the reference person is with $24.4\,\mathrm{kg/m^2}$ lower than the mean patient BMI of $25.5\,\mathrm{kg/m^2}$, therefore also the derived effective dose is lower for the reference person than for the

patient collective. Note that similar to conversion coefficients, also DRLs themselves are determined for the reference person. Therefore, DRLs can be exceeded when the examined patients deviate from the reference person.

Further Dose Reduction

In the future, the potential for further dose savings within this prototype system has to be evaluated. One possibility is the reduction of the number of frames during the scanning procedure, which would directly lead to a decrease in patient exposure. Therefore, the minimum number of different relative fringe positions per pixel required for robust image processing has to be determined. Another approach to directly decrease patient exposure is the reduction of the intended detector dose, which would reduce the tube current per patient. Therefore, the minimum detector dose at which images with high quality can be reconstructed has to be determined. Yet, a reduced detector dose increases the effect of electronic read-out noise on the images, so the replacement of our detector by a photon-counting detector (PCD) can be considered. As there is no readout noise in PCDs, it would be possible to acquire images with the same signal-to-noise ratio as with the flat panel detector while decreasing the necessary detector dose. Currently, colleagues are working on a project to evaluate the image quality at lower detector doses. Another hardware approach is the implementation of improved gratings with higher aspect ratios, which could absorb X-rays of higher energy more efficiently and therefore enable the application of a higher tube voltage. As especially low-energetic photons contribute to absorbed dose, this could also decrease the effective patient dose.

Compliance to Legal Requirements

The mean DAP values measured for the given patient collective are below the local reference DAP assigned by the BfS, therefore our prototype system fully complies with the legal requirements in Germany. As discussed before, the large standard deviation of measured DAP values indicates that this result highly depends on the examined patient collective. The compliance with the regulations was affirmed by the BfS in April 2020. This affirmation is also a prerequisite for further studies.

Comparison to other Reference Values

While we fulfill the legal requirements for our prototype system, our reference values of $\mathrm{DAP}_{\mathrm{reference,pa}} = 30\,\mu\mathrm{Gy\,m^2}$ and $\mathrm{DAP}_{\mathrm{reference,lat}} = 80\,\mu\mathrm{Gy\,m^2}$ are twice as high as the respective DRLs of conventional thorax radiography in Germany [Schegerer, 2019]. How-

ever, the prototype system yields both a conventional radiograph as well as the novel dark-field image simultaneously. Numerous animal models proved an increased diagnostic value of dark-field radiography for different lung pathologies [Schleede, 2012; Meinel, 2013; Hellbach, 2015; Yaroshenko, 2015; Hellbach, 2017; Scherer, 2017; Hellbach, 2018], and recently its application for detection and quantification of emphysema in humans was confirmed [Willer, 2021; Gassert, 2021; Urban, 2022]. Further studies will evaluate whether the additional and complementary diagnostic information justifies the increase in effective patient dose.

Because DRLs depend on the issuing country, their variation is quite high even for the same examination. For plain chest radiography in pa orientation, DRLs range from 10–50 µGy m^2 in Europe [EC, 2011]. Higher DRL values are adopted from European or international recommendations, while countries with lower DRLs have carried out their own survey to determine local DRLs [EC, 2011]. So even though the assigned reference value for the dark-field system is higher than for conventional radiography at the local site, it is still within the range of reported DRLs [EC, 2011].

Exposure Control for Prototype System 5

The findings presented here will be published in the article "Exposure Control at First Dark-Field Chest Radiography Demonstrator System" by Frank and Willer et al. [Frank, in Review], which is in review at the time of writing. Compared to the submitted work, some wording and figures have been slightly modified, and further information about the calibration process was provided. In addition to pa examinations, also lat examinations are presented in this chapter. Additionally, an evaluation of the achieved detector doses of the second study on COVID-19-pneumonia was included. Further, the regulations on exposure indices are presented in Section 2.4, and the technical introduction to the used setup has been omitted, as it can be found in Chapter 3.1.

5.1 Motivation

In contrast to film radiography, gray levels of digital radiographs are usually adjusted later, making it independent of incident optical density. Nevertheless, exposure of detectors has to be supervised to ensure image quality, as underexposure leads to increased noise and reduced signal-to-noise ratio which may impede diagnosis, yet overexposure increases the associated effective patient dose unnecessarily. The amount of exposure resulting in a diagnostic image differs based on the body part examined as well as the size of the patient, as larger patients absorb more of the incident radiation. Exposure control is supposed to find the optimum dose level with regard to the ALARA principle (***A**s **L**ow **A**s **R**easonably **A**chievable*) [ICRP, 1997].
In conventional radiography, so-called automatic exposure control (AEC) is implemented to satisfy these requirements [Ching, 2014]. Exposure is regulated by adapting either tube current or exposure time, in fluoroscopy also tube voltage [Geise, 2001]. One working principle of AEC used for digital projection radiographs is based on controlling the exposure time at a fixed tube current via a feedback between ionization chambers located in the image receptor plane, and the X-ray tube. The ionization chambers measure the amount of dose right in front of the detector, and signal the X-ray tube to stop the exposure once a given threshold is reached [Eastman, 2011; Artz, 1997; Markivee, 1980]. In computed tomography imaging, exposure time is constant

for each projection while the tube current is adjusted. Often, an additional scout scan of the investigated body part is utilized to determine the tube current necessary for a given detector dose in dependence on the longitudinal axis of the patient [Kalra, 2004].

5.2 Methods

An overview of key figures in exposure control is given in Section 2.4. The regulatory requirements for Germany specify measures of exposures for the respective region of interest (ROI) for patient examinations [IEC, 2008]. For images obtained at the dark-field system in pa orientation, the ROI consists of the entire lung without the heart shadow, and for lat examinations of the entire lung. In order to evaluate the exposure at the system, we manually selected the outline of the lung from the obtained attenuation images. Detector dose maps for the region of interest were generated by summation over all individual frames and subsequent conversion of the measured intensity into dose values. A conversion from detector units to absorbed dose at the dark-field system was obtained via prior calibration measurements using a solid state dose sensor (NOMEX Multimeter, *PTW*, Germany) (for further information, the reader is referred to [Willer, 2022]).

Note that we use the detector dose D instead of the Exposure Index (EI) for the dark-field system. The detector dose is directly accessible from the raw data at the dark-field system and, therefore not dependent on the algorithm determining the region of interest. Contrary, at the commercial system, the detector dose is not directly accessible. Consequently, for examinations at the dark-field system, we calculate the DI according to Equation 2.23 with (target) detector dose values instead of (target) exposure index. At the commercial system, the detector dose is not accessible, therefore we used the standardized EI and DI.

5.2.1 Approach 1: Calibration from Reference Device to Dark-field System

For the first exposure control approach at the dark-field system, we take advantage of the fact that every patient obtains a thorax radiograph on a commercial system as an integral part of the COPD study (see Section 3.3.1). The conventional radiograph is utilized as a scout scan for the dark-field system, similar to common practice for CT examinations [Kalra, 2004]. The commercial system operates at 125 kV and regulates exposure with an AEC. The relevant exposure parameters are patient-specific and subsequently serve as input to adjust the tube current at the prototype system for

each patient individually via a calibration we present here. Note that the conventional radiograph is taken in inspiration [Saure, 2008], and the calibration is accordingly most suited for radiographs in inspiration. In this study, the calibration is also exploited for radiographs in expiration, where the total attenuation along the beam path is increased.

Exposure at Commercial Reference System

For chest examinations, AEC is used. The AEC at the commercial system automatically stops the X-ray tube current once sufficient radiation dose has reached the selected ionization chambers in front of the flat-panel detector. In practice, this results in deviations between the EI and the EIT, as the relevant image area does not perfectly register with the location of the ionization chambers.

To account for these deviations, we calculate the normalized exposure for which the EIT for the individual patient examination would have been reached:

$$Q_{\text{normalized}} = Q_{\text{measured}} \cdot \frac{\text{EIT}}{\text{EI}_{\text{measured}}}, \tag{5.1}$$

with the exposure Q (current-time-product, physical unit: mAs). Here, the exposure applied to each individual patient during the standard chest examination is normalized to the ratio of the actually measured EI and the EIT. In our institution, EIT = 250 is the value used for clinical routine work. For this approach, we will use the normalized exposure of the standard chest examination at the commercial system for prospective exposure control for the image acquisition at the dark-field system.

Calibration Method

In order to convert exposure from the commercial system to the necessary tube current at the dark-field prototype system, we use a calibration based on an equivalent attenuator thickness to model each patient individually. As we are interested in lung imaging, with the lung mainly consisting of soft tissue, we use polyoxymethylene (POM) as a surrogate material to model attenuation properties. The amount of POM necessary to model the attenuation of the individual lung is called equivalent attenuator thickness (d_{POM}). Here, the calculated d_{POM} serves as input at the dark-field prototype system to adjust the tube current accordingly in order to reach a desired target detector dose.

Therefore, in the first step, we recorded the current-time-product Q as well as the EI for measurements at the commercial system with different amounts of POM in the beam path three times. Acquisition parameters were set for default thorax measurements, with a selection of the according ionization chambers for AEC. The measured data is

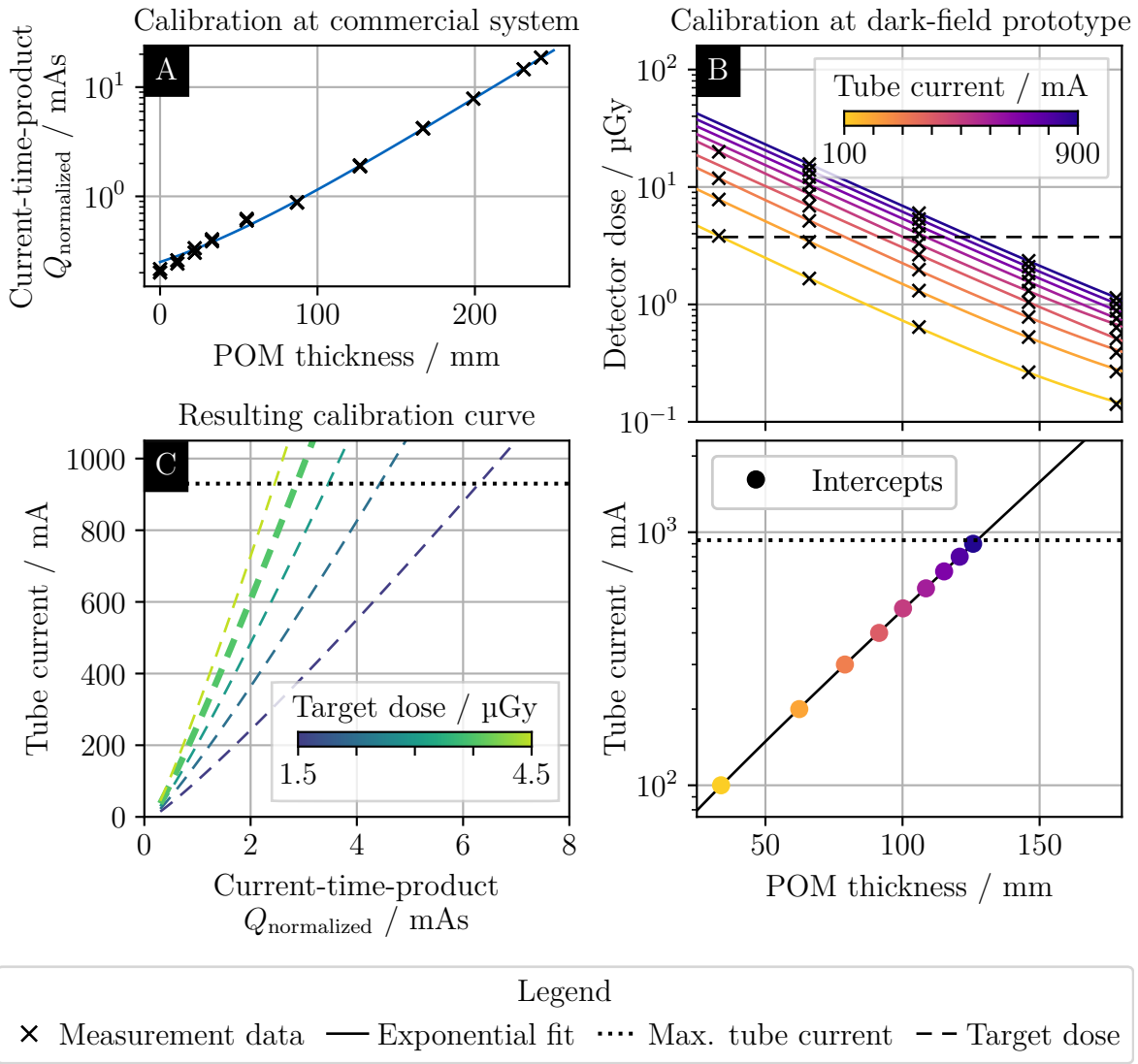

Figure 5.1: Calibration measurements and fits. A, AEC-regulated exposure (tube current-time-product Q) at commercial system, normalized with actual Exposure Index (EI) according to Equation 5.1. Measurement points were taken with increasing attenuator thicknesses of POM, along with exponential fit. B, Upper part shows the detector dose at the dark-field prototype for increasing thickness of attenuator material, obtained with different tube currents. For each tube current, an exponential decay fit gives the achieved detector dose for any amount of attenuator thickness. The intercept values of the single functions with D_{target} (dashed line) are plotted in the lower part, in combination with an exponential fit. C, Resulting calibration curves for different target dose values. The target dose at the dark-field system used within the study ($D_{\text{target}} = 3.75\,\mu\text{Gy}$) is marked by a thicker line.

depicted in Figure 5.1A, along with the respective exponential model obtained from a least-squares fit of the form

$$Q_{\text{normalized}} = a \cdot e^{b \cdot d_{\text{POM}}} + c. \tag{5.2}$$

Assuming Compton scatter can be neglected due to an installed anti-scatter grid, an exponential behavior is predicted by the Beer–Lambert law.
In a second step, we took a measurement series at the dark-field prototype system obtaining the detector dose D for varying attenuator thicknesses at different tube currents (cf. Figure 5.1B, upper part). Note that in this case, we took the detector dose, averaged over the whole detector. A least-squares fit to an exponential model gave the exact thickness of POM for each measured tube current at which the target detector dose D_{target} is reached. Through another exponential fit to these intercepts values, we found a calibration curve that relates the tube current required for each amount of POM to achieve D_{target} at the dark-field prototype system (cf. Figure 5.1B, lower part) via

$$I_{\text{tube}} = f \cdot e^{g \cdot d_{\text{POM}}} + h. \tag{5.3}$$

We determined a relation between equivalent attenuator thickness and detector dose with this information.
By combining the calibration curves of both systems, more precisely, by taking the calculated equivalent POM thickness from the commercial system as input to the calibration curve at the dark-field system that gives the respective necessary tube current to reach D_{target} (cf. Figure 5.1B, lower part), a final conversion of patient-specific exposure settings at the commercial system to required tube current at the dark-field prototype system is retrieved (cf. Figure 5.1C).

Due to the linear relation between tube current and obtained detector dose, the calibration function can be adapted by

$$I_{\text{tube}}(D_{\text{target}}) = I_{\text{tube}}(D_{\text{target,calib}} = 3.75\,\mu\text{Gy}) \cdot \frac{D_{\text{target}}}{3.75\,\mu\text{Gy}}, \tag{5.4}$$

to reach any desired target detector dose D_{target}. For exemplary D_{target}, the corresponding conversion functions are depicted in Figure 5.1C. A thicker line marks the conversion function used for the patient study.

Exact Description of Approach

The above-described calibration was carried out before the prototype was finalized in all details. Therefore, the speed of the interferometer drive and the X-ray window,

meaning the time the X-ray tube actively produces X-rays per frame, changed from calibration to operation. Therefore, the calibration measurements were carried out at 30 Hz, the X-ray window was set to 12 ms, and the interferometer drive moved at a speed of 100 mm s^{-1}.

As mentioned in Section 3.1, patient measurements are now performed at a frame rate of 30 Hz with a set X-ray window of 19 ms. Nevertheless, although the settings suggest an X-ray window of 19 ms, in reality it corresponds to 17 ms. The speed of the interferometer drive is set to 87 mm s^{-1}. Therefore, the obtained calibration values were readjusted to the final settings by dividing by 1.413 (17 / 12, due to the X-ray window) and multiplying with 87 / 100 (due to the speed of the interferometer drive).

Also, for the calibration measurement at the dark-field prototype, the target detector dose was set to $D_{\text{target}} = 2.5\,\mu\text{Gy}$. The curves in Figure 5.1B and Figure 5.1C are plotted for the final $D_{\text{target}} = 3.75\,\mu\text{Gy}$, as calculated according to Equation 5.4. The reasoning for the chosen D_{target} is discussed in the following section.

A final calibration curve of the form

$$I_{\text{tube}} = \left(f \cdot e^{\frac{g}{b} \ln\left(\frac{Q_{\text{normalized}} - c}{a}\right)} + h \right) \cdot \frac{3.75\,\mu\text{Gy}}{2.5\,\mu\text{Gy}} \tag{5.5}$$

is obtained, combining Equation 5.2 solved for d_{POM} and Equation 5.3. Here, $Q_{\text{normalized}}$ is obtained from the commercial system according to Equation 5.1, and a to f are fit parameters. The values of the fit parameters as used for patient examinations are listed in Table 5.1.

Parameter	a / mA s	b / mm^{-1}	c / mA s	d / mA	e / mm^{-1}	f / mA
Value	0.1376	0.020 22	0.111 30	21.646	0.022 72	−5.7451

Table 5.1: Fit parameters of Equation 5.5 for calibration approach 1. Although the parameters can not be determined with that kind of precision, these are the values that are hard-coded in the operator software.

Determination of Target Detector Dose

Prior to the start of the patient study, the target detector dose for patient examinations at the dark-field system was determined to $D_{\text{target}} = 3.75\,\mu\text{Gy}$. By that, a maximum POM thickness of about 150 mm (corresponding to a soft tissue thickness of 210 mm) can be covered by the system. In the following, we outline the argumentation on which

this determination is based.
In clinical routine, target value proposals are generally issued by medical associations [Saure, 2008]. Here, extensive clinical studies result in guidelines restricting patient exposure to a reasonable level when addressing certain medical questions. For instance, besides anatomical and technical requirements, the German medical association proposes the detector dose not to exceed 5 µGy in thorax examinations [Saure, 2008]. In our case, however, where no prior clinical experience is available, an initial determination based on the results from the exposure control validation study with the phantom and the exposure limits approved by the Bundesamt für Strahlenschutz (*Federal Office for Radiation Protection*) (BfS) was made. The BfS issued a local reference dose-area product (DAP) of 30 µGy m^2 for examinations in pa orientation that refers to the reference person weighing 73 kg [Frank, 2021] (cf. Chapter 4). Due to the reference to the body weight, the target detector dose for the scan at the dark-field system was chosen in a way that the approved DAP value is reached for a reference person, here modeled by the LUNGMAN phantom with one additional chest plate, corresponding to 73.7 kg.
Prior to the start of the patient study, D_{target} in Eq. 5.4 was adapted until the approved DAP limit was measured for this phantom configuration. With a DAP of 29.3 µGy m^2 at $D_{\text{target}} = 3.75$ µGy, this target value was then utilized to estimate the proper tube current settings for patient scans.

5.2.2 Approach 2: Conversion with Patient's Body Parameters

In further studies with the dark-field system, we aimed to be independent of a reference measurement with additional exposure to ionizing radiation. Therefore we investigated alternative methods for exposure control. For this purpose, we calculated the Pearson correlation coefficient between the tube current necessary for image acquisition at the dark-field system and patient-specific body parameters.

Conversion Method

As there are deviations in the achieved detector dose from the target value D_{target} with the tube current set via approach 1, the tube current that would have given the target detector dose is obtained via a normalization of the used tube current:

$$I_{\text{normalized}} = I_{\text{used}} \cdot \frac{D_{\text{target}}}{D_{\text{measured}}}, \tag{5.6}$$

similar to Equation 5.1. The normalization accounts for uncertainties and deviations in the process, such as human error and the fact that the lung region is superposed by

surrounding tissue. As possible patient-specific parameters, we collected weight, BMI, the girth of the upper bust, and girth under the bust line for each patient.
In a simple assumption, we suppose that all these parameters scale proportional to an approximate POM-equivalent thickness in the region of interest. Due to the Beer–Lambert law, this suggests a linear dependency between the logarithmic normalized tube current and these body parameters, therefore the Pearson correlation coefficient is evaluated between these values.

For the parameter k with the strongest correlation, a least-squares fit of the form

$$\ln\left(I_{\text{normalized}}\right) = m \cdot k + t \tag{5.7}$$

is performed. The fit function, yielding the normalized tube current depending on the body parameter, then gives us a method for exposure control in future studies in which a conventional radiograph is not included for the patients.

Correlation with Patient's Body Parameters

Figure 5.2 and Figure 5.3 depict the normalized tube current (cf. Equation 5.6) of 94 patients imaged via approach 1 as a function of the patient's body parameter for pa and lat examinations, respectively. More precisely, the figures show weight (A), body mass index (BMI) (B), girth of the upper bust (C), and girth under the bust line (D). Note that the y-axes in both figures are scaled differently. In each subplot, the Pearson correlation coefficient r along with its p-value is given.

For pa examinations, the strongest correlation was found between normalized tube current (in the logarithmic scale) and patient's BMI ($r = 0.87$), being closely followed by patient's weight ($r = 0.86$). For the girth of the upper bust ($r = 0.80$) and girth below the bust line ($r = 0.77$), a weaker correlation was found. All these correlations are significant with $p < 0.05$.
For lat examinations, again, the strongest correlation was found between normalized tube current (in the logarithmic scale) and patient's BMI ($r = 0.77$). The second strongest correlation is also with the patient's weight ($r = 0.75$), followed by the girth of the upper bust ($r = 0.68$) and girth below the bust line ($r = 0.62$). As for pa examinations, all these correlations are significant with $p < 0.05$.
For the BMI, the resulting calibration curves (cf. Equation 5.7) obtained from a least-squares fit are depicted in orange in Fig. 5.2B and Fig. 5.3B. The respective fit parameters for pa and lat examinations of Equation 5.7 are listed in Table 5.2. With these two new calibration curves, the tube current is chosen via the patient's BMI in studies that do not include a conventional radiograph for reference, such as the study on COVID-19-pneumonia described in Chapter 6.

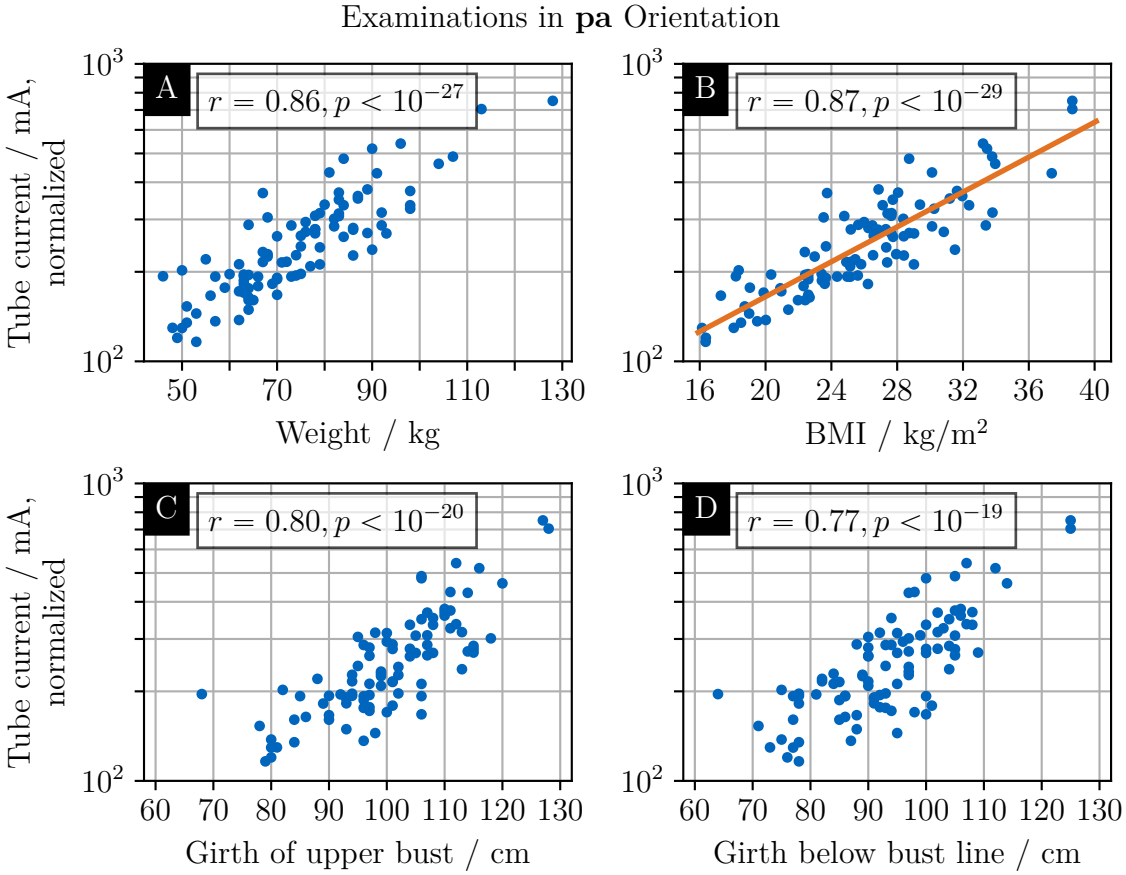

Figure 5.2: Normalized tube current at dark-field prototype system for different body parameters of patient collective for pa examinations. A: Weight, B: body mass index (BMI), C: Girth of upper bust, D: Girth below bust line. The tube current was set according to approach 1, and normalized to the target detector dose according to Eq. 5.6. The Pearson correlation coefficient r for each parameter was calculated for the logarithmic tube current along with its p-value. In B, the resulting calibration function from BMI to tube current is included (R^2-value for fit: 0.75).

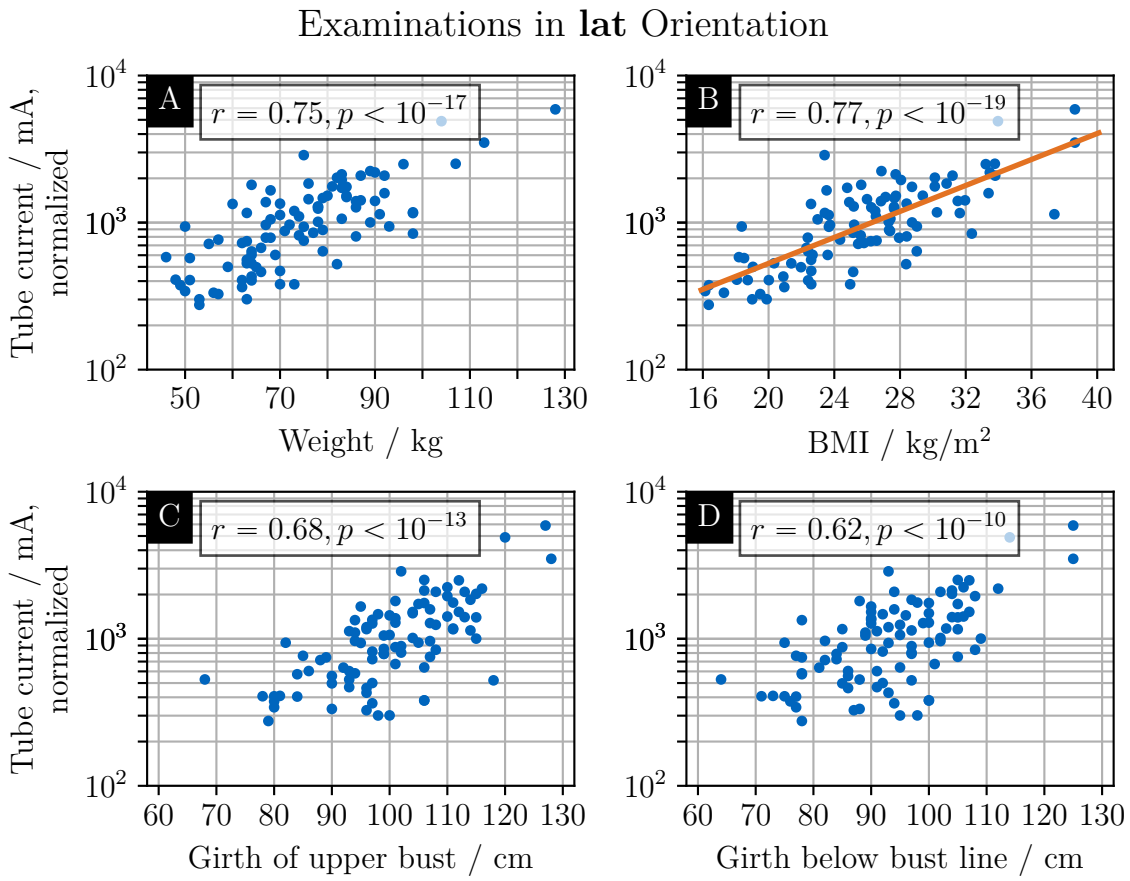

Figure 5.3: Normalized tube current at dark-field prototype system for different body parameters of patient collective for lat examinations. A: Weight, B: body mass index (BMI), C: Girth of upper bust, D: Girth below bust line. The tube current was set according to approach 1, and normalized to the target detector dose according to Eq. 5.6. The Pearson correlation coefficient r for each parameter was calculated for the logarithmic tube current along with its p-value. In B, the resulting calibration function from BMI to tube current is included (R^2-value for fit: 0.60). Note that the y-axes have a different scale than in Figure 5.2.

Parameter	m / mA/(µGym^2)	t / mA
Value for pa orientation	0.067 720 62	3.748 018 67
Value for lat orientation	0.102 379 56	4.213 612 80

Table 5.2: Fit parameters of Equation 5.7 for calibration approach 2. Although the parameters can not be determined with that kind of precision, these are the values that are hard-coded in the operator software.

5.2.3 Evaluation with Phantom and Patient Collective

The approaches described above were evaluated first with an anthropomorphic chest phantom and later again with a patient collective.

Validation Using an Anthropomorphic Chest Phantom

Before starting the first patient study, we verified the exposure control approach 1 described above by employing the anthropomorphic X-ray LUNGMAN thorax phantom (Multipurpose Chest Phantom N1, *Kyoto Kagaku*, Japan). The phantom models the anatomy of a human torso in life-size dimensions. X-ray attenuation properties of the soft tissue surrogate material and the synthetic bones are similar to the human counterpart. We used urethane foam to mimic the lung and could therefore not use the heart and pulmonary vessels inset, which in turn are not modeled. Two additional chest plates can be attached to the phantom to represent larger body types. Characteristics of the three different versions of the LUNGMAN phantom simulating different patient sizes (light, medium, and heavy physique realized with no chest plate, one chest plate, and two chest plates, respectively) are listed in Table 5.3.

	Light physique	Medium physique	Heavy physique
Number chest plates	0	1	2
Height / cm	168.2	168.2	168.2
Weight / kg	65.4	73.7	82.0
BMI / kg m^{-2}	23.1	26.1	29.0

Table 5.3: Characteristics of the LUNGMAN phantom simulating the three different represented body types.

For the initial validation, all three versions of the LUNGMAN phantom were imaged at the commercial system with AEC. Here, the same thorax protocol as intended for the patient study was utilized. With the prior determined calibration function and the acquisition parameters obtained from the commercial system, we then took radiographs of the phantom's light, medium, and heavy configurations at the dark-field prototype system. Note that this initial validation was performed for pa examinations only, as the focus was placed on these examinations.
For the second exposure control approach, only the light physique was tested. As the urethane foam inset does not adequately represent the pulmonary vessel structure and therefore underestimates absorption, a certain deviation between the target detector dose and the actual detector dose is expected. No additional value is obtained from testing the other physiques with approach 2.

Validation for Patient Collective

To assess the accuracy of the tube current settings for patients, a similar evaluation procedure to the previous phantom study was carried out retrospectively: Detector dose values in the manually selected lung regions were extracted, averaged, and compared to the ones obtained in the phantom study as well as the target detector dose. The patient collective used to evaluate approach 1 comprises participants of the COPD study, while the patient collective used for approach 2 consists of patients included in the study on COVID-19-pneumonia, both described in Section 3.3.2. For the evaluation of approach 1, three subjects with varying BMIs were chosen to cover the patient collective. In contrast, three subjects with roughly the same body parameter for tube current determination were selected to evaluate approach 2.

5.3 Validation of Approach 1

The obtained EIs and tube current-time-products from LUNGMAN phantom measurements modeling different physiques at the commercial system, as listed in the upper part of Table 5.4, were used as input for the conversion function.

The lower part of Table 5.4 shows the results of the dark-field system, namely, the tube current used for image acquisition, the mean detector dose in the lung region for examinations at the dark-field system, and the DI (cf. Equation 2.23). Additionally, for the LUNGMAN measurement in light physique configuration in lat orientation at the commercial system, EI = 375 and $Q = 1.26\,\mathrm{mA\,s}$ was found, translating to a tube current of $I_{\mathrm{tube}} = 202\,\mathrm{mA}$.

Figure 5.4 depicts detector dose maps obtained from summation over all exposures

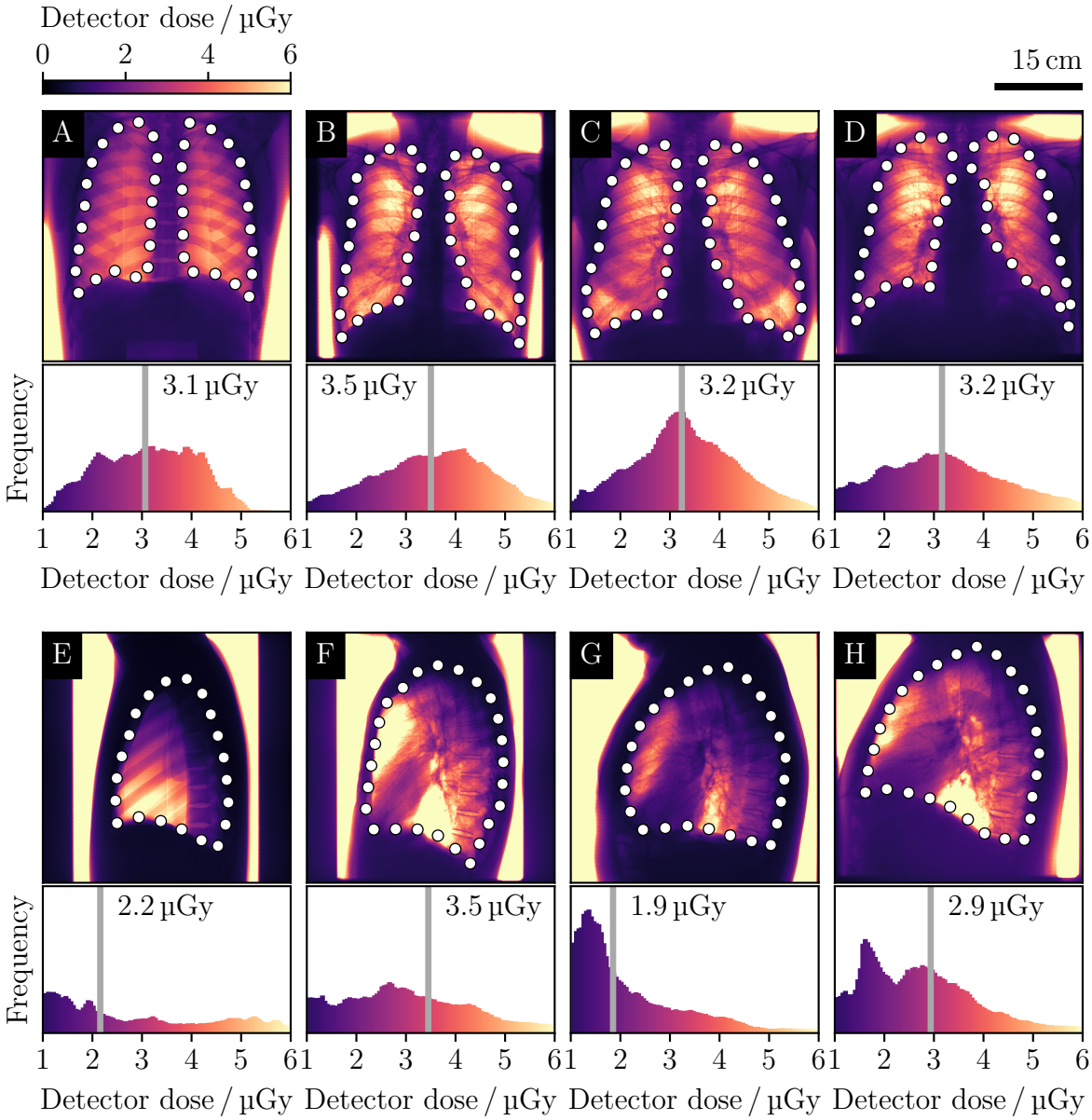

Figure 5.4: Exposure control validation, Approach 1. Detector dose map with mask for lung region segmentation (each upper row), and histogram of the dose values (each lower row) present in the segmented region. The mean detector dose in the segmented region is given within the histograms. The evaluation was carried out for the phantom (A, E) and three patients (B-D, F-H). B&F, C&G, and F&H are obtained from pa and lat examinations of one patient, respectively. Information on patients can be found in Table 5.5. Dose values of directly exposed regions exceed the value range of the displayed images.

	Light physique	Medium physique	Heavy physique
Current-time-product Q / mAs	1.4	2.2	3.3
Exposure Index EI	594	556	519
Tube current I / mA	122	251	459
Detector dose lung region D / µGy	3.1	3.4	3.5
Deviation index DI	-0.83	-0.43	-0.30

Table 5.4: Measured parameters for LUNGMAN examinations simulating the different body types at commercial system (upper part) and dark-field prototype system (lower part).

taken at the dark-field system, including segmented lung masks (upper part, outline of mask indicated by dots) and histograms of detector dose distribution within the respective lung region (lower part). The data set obtained for the phantom in the lightest physique configuration is depicted in Figure 5.4A&E, and data sets of three exemplary patients in Figure 5.4B-D and F-H for examinations in pa and lat orientation, respectively. Information on the three patients, along with the tube current used for image acquisition, can be found in Table 5.5, and information on the LUNGMAN is listed in Table 5.4.
We observe a good agreement of achieved detector dose values for pa examinations, independent of the person's BMI. There is a larger deviation for lat examinations. Especially in the regions where the heart shadow and the spine are depicted, low detector dose values are observed.

Patient	Gender	Age / years	BMI / kg m^{-2}	I_{tube}, pa / mA	I_{tube}, lat / mA
B & F	male	55	16.1	123	344
C & G	male	48	25.0	172	202
D & H	male	57	32.4	295	683

Table 5.5: Patient information for patients depicted in Figure 5.4B-D and E-H, along with tube current used for image acquisition at dark-field prototype system.

Here, we evaluated the first 94 participants (57 male, 37 female) of the first patient study on COPD, with an average age of 63.4 (SD: 12.2) years and an average BMI of 25.8 (SD: 4.9) kg m^{-2}. Table 5.6 lists the mean detector dose, averaged over all patients, including its standard deviation and its DI obtained in the different breathing states for

Orient.		Inspiration	Expiration
pa	Detector dose D in lung region / µGy	3.43	3.00
	SD detector dose in lung region / µGy	0.52	0.47
	Deviation index DI	−0.39	−0.97
lat	Detector dose D in lung region / µGy	2.39	1.48
	SD detector dose in lung region / µGy	0.92	0.73
	Deviation index DI	−1.95	−4.05

Table 5.6: Average detector dose behind lung region and deviation index DI of the first 94 study participants for examinations at the dark-field system in inspiration and expiration. Abbreviation: Orient., Orientation; pa, posterior-anterior; lat, lateral; SD, standard deviation.

the first 94 patients for the examinations at the dark-field system. For both breathing states, the mean detector dose is below the target detector dose, reflected in negative DI values, with a smaller deviation for examinations in inspiration.
Additionally, we evaluated the EI of the radiographs taken at the commercial system for the same patients. Here, we found a mean EI of 319 (SD: 49.4) for pa examinations and a mean EI of 409 (SD: 92.1) for lat examinations for a target value of EIT = 250, which results in DIs of 1.06 and 2.14, meaning slight overexposure.

5.4 Validation of Approach 2

In the style of Figure 5.4, Figure 5.5 depicts detector dose maps of pa and lat examinations obtained from summation over all exposures taken at the dark-field system, including segmented lung masks (each upper row, outline of mask indicated by dots) and histograms of detector dose distribution within the respective lung region (each lower row). As above, Figure 5.5A and E represent the data set obtained for the phantom in the lightest physique configuration, and the respective data set of three exemplary patients are depicted in Figure 5.5B-D and F-H for examinations in pa and lat orientation, respectively. According information on the imaged subjects is listed in Table 5.7, along with the used tube current.

Further, the mean detector dose, its standard deviation, and the mean DI for 60 patients, which were subject to exposure control approach 2 per study about COVID-19-pneumonia, are listed in Table 5.8. The patient cohort exhibits an average age of 57.5

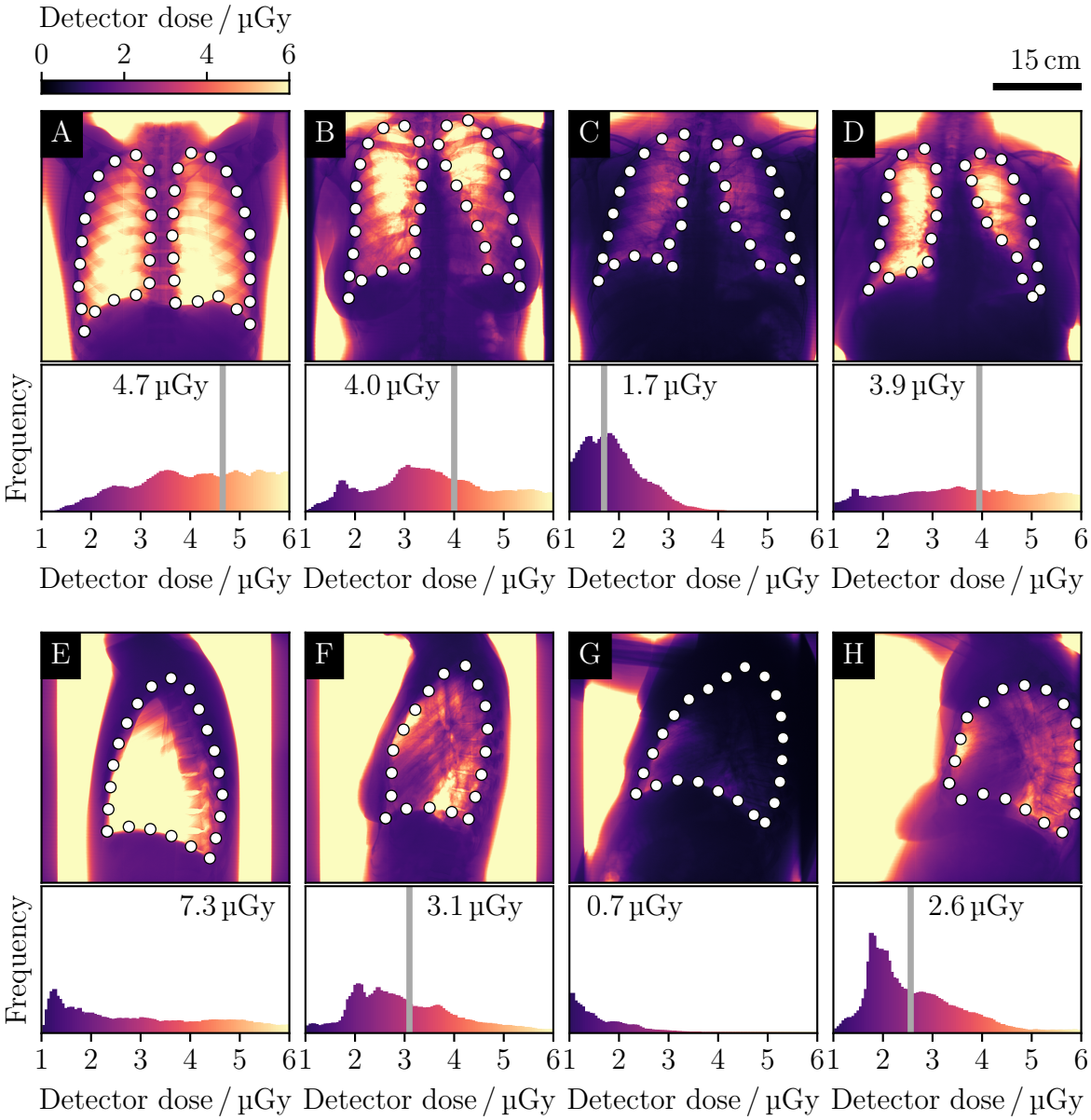

Figure 5.5: Exposure control validation, Approach 2. Detector dose map with mask for lung region segmentation (each upper row), and histogram of the dose values (each lower row) present in the segmented region. The mean detector dose in the segmented region is given within the histograms. The evaluation was carried out for the phantom (A, E) and three patients (B-D, F-H). B&F, C&G, and F&H are obtained from pa and lat examinations of one patient, respectively. Information on patients can be found in Table 5.5. Dose values of directly exposed regions exceed the value range of the displayed images.

Patient	Gender	Age / years	BMI / $kg\,m^{-2}$	I_{tube}, pa / mA	I_{tube}, lat / mA
A & E	LUNGMAN		23.1	202	714
B & F	female	32	24.5	224	834
C & G	male	53	28.1	290	930
D & H	female	78	29.4	310	930

Table 5.7: Patient information for patients depicted in Figure 5.5B-D and F-G, along with tube current used for image acquisition at dark-field prototype system. These participants are chosen to validate approach 2 for exposure control. Note that 930 mA is the upper limit of available tube currents.

(SD: 13.8) years and an average BMI of 26.9 (SD: 3.9) $kg\,m^{-2}$.

Orientation		Inspiration
pa	Detector dose D in lung region / µGy	2.75
	SD detector dose in lung region / µGy	0.68
	Deviation index DI	−1.35
lat	Detector dose D in lung region / µGy	2.06
	SD detector dose in lung region / µGy	0.80
	Deviation index DI	−2.60

Table 5.8: Average detector dose behind lung region and deviation index DI of 60 study participants with exposure control approach 2, for examinations at the dark-field system. Abbreviation: pa, posterior-anterior; lat, lateral; SD, standard deviation.

In contrast to approach 1, the LUNGMAN phantom produces considerably higher detector doses. We can see that for patient C & G, the detector dose values are very low, even lower than patient D & H, who has a higher BMI. Compared to approach 1, the deviation in achieved detector dose values is increased, both towards higher and lower values. The higher deviation is reflected in the increased standard deviation. The altogether decreased D values result in a decreased DI compared to approach 1.

5.5 Discussion

Influence of Choice of Target Detector Dose

Due to the linear relation between tube current and emitted dose, the calibration function can be adapted by

$$I_{\text{tube}}(D_{\text{target}}) = I_{\text{tube}}(D_{\text{target,calib}} = 3.75\,\mu\text{Gy}) \cdot \frac{3.75\,\mu\text{Gy}}{D_{\text{target}}}, \tag{5.8}$$

to reach any desired target detector dose D_{target} as long as it is within the detector's linear response range. For exemplary D_{target}, the corresponding conversion functions are depicted in Figure 5.1C. By the course of the different functions, these curves illustrate that the choice of D_{target} influences the upper limit of absorber thickness and corresponding patient weight due to the power limitations of the X-ray source.

Validation of Dose Planning Approach 1

Comparing the obtained detector dose values with the targeted dose for the phantom measurements, lower values are obtained for all measurements with a tendency to a better match for larger physiques (see Table 5.4). Differences between the calibration and the phantom scan in terms of Compton-scatter occurrence may serve as a possible explanation for this observation. Apart from the transmitted ratio of the primary beam, Compton scatter from the adjacent irradiated tissue contributes to the radiation reaching one detector pixel. The POM slabs used for the calibration might differ from the phantom regarding the generation of scatter photons. Also, the spatial distribution of scattered photons, associated with the spatial distribution of the attenuating material, varied between calibration measurement where the POM slabs covered the entire detector and the phantom measurements. The empirically determined fit parameters for the POM calibration incorporate its Compton properties and would therefore yield a correct dose conversion for a POM sample of unknown thickness. However, for the phantom, the conversion function is only a close approximation as the scatter properties deviate from the ones of the calibration material.

Similar to the phantom measurements, also the detector dose values obtained for patients as listed in Table 5.6 are below the targeted detector dose. The same differences in Compton scatter as for the phantom apply to the patients. Also, there is an additional methodical inaccuracy depending on the patient's individual anatomy (i.e., breast size) and the positioning at the conventional radiography system with respect to the dose sensors of the AEC. Considering that, and the requirement of the German

Institute for Standardization of the EI to be consistent within 20 % for a homogeneous absorber where positioning errors can be eliminated [DIN, 2013], the detector dose consistency, expressed by the relative standard deviation and its deviation from the target value over the patient collective, is in an acceptable range.

A decrease in detector dose for examinations in expiration is observed (cf. Table 5.6). As the conventional radiographs are carried out in inspiration and utilized for exposure planning at the dark-field system, this observation is related to an increased density of the lung associated with material compression when air is exhaled.

Further, a decrease in detector dose is also observed for examinations in lat orientation. We contribute this to the fact that both the heart shadow and the spine is located within the evaluated lung region. While the heart might be modeled with the equivalent absorber thickness of POM in principle, the location of the ionization chambers of the commercial system should exclude the influence of the heart for the most part. Therefore, the contribution of the heart is neglected already in the first step, performing the scout scan. The latter is also true for the spine, although bone structures can never be approximated by a soft tissue equivalent.

Deviation from Target Values

While AEC controlled exposure tends to exceed the target value, the mean detector dose at the dark-field system is below the target value. The higher values at the conventional system can be explained by the nature of the AEC, as the exposure is stopped once the dose threshold is reached, and finite response times lead then to an exceedance. In contrast, the calibration model for the dark-field system sets the tube current before the exposure, and due to the differences in Compton scatter as described above, a lower value is found. To assure diagnostic image quality, it is important to avoid underexposure, therefore a reduced detector dose could lead to increased noise in the radiographs. For future systems, this has to be taken into account when providing patient-specific exposure control. Yet in this first approach, we achieve satisfactory consistent detector dose values over the examined patient collective that are well within legal requirements.

Justification of Target Detector Dose

A target detector dose of $D_{\text{target}} = 3.75\,\mu\text{Gy}$ was chosen for the first patient study evaluating the potential of X-ray dark-field lung imaging based on exposure limits issued by the Bundesamt für Strahlenschutz (*Federal Office for Radiation Protection*) (BfS). This consideration is not yet based on medical evaluation of the obtained images and their quality, as they did not exist beforehand. The target detector dose is subject

to adjustment when there is more clinical data and long-time experience, and the adjustment can be both towards lower and higher doses.

Relation to Patient's Body Parameters

Although the assumption that all four parameters scale proportionally to the irradiated tissue thickness seems crude, the high correlation with very small p-values justifies this approach. In future patient studies, we want to be able to regulate exposure without an additional radiograph. The strong correlation between BMI and tube current at the dark-field prototype system indicates the suitability of choosing the tube current patient-specific, depending on their BMI while keeping the corresponding detector dose consistently stable. A BMI-based adaption of CT protocols has proven successful in other areas such as angiography [Hosch, 2012; Schreiner, 2017].

Deviations for Approach 2

The observed deviations of the achieved detector dose and the target detector dose are increased compared to approach 1, with the mean of the achieved detector doses at $D_{\text{mean}} = 2.75\,\mu\text{Gy}$. Consequently, the DI is increased compared to approach 1, with a mean DI of -1.35. We contribute this deviation in part to the fact that COVID-19-pneumonia consolidates the lung, therefore increasing the lung's attenuation. In contrast to healthy subjects or participants with emphysema, COVID-19-patients inherently are subject to lower detector dose values due to these consolidations. In hindsight, a correlation of any body parameter to normalized tube current in a patient cohort of healthy subjects or participants with pulmonary emphysema will likely not be transferable to subjects with a pulmonary disorder that leads to increased attenuation in the lung. While the strong correlation ($r = 0.87$ and $r = 0.77$ for pa and lat examinations, respectively) is there for the evaluated patient collective, the evaluation showed the approach is not transferable to consolidating pulmonary diseases. With the experience of the 60 participants in the study on COVID-19-pneumonia, the correlation between normalized tube current and body parameter should be determined again. It is possible that a different fit, depending on the subject's lung condition, is necessary, therefore discriminating between healthy subjects, subjects with emphysema decreasing the lung's attenuation, and subjects with disease increasing the lung's attenuation. Further studies will need to evaluate the correlation for different disease models.

For now, the strong recommendation is to continue patient studies with exposure control approach 1, and using the scout scan of the commercial DiDi for tube current determination. Once sufficient data on different diseases is available, a new study on the correlation of the body parameters is appropriate.

Nevertheless, while exposure approach 2 does not provide detector dose values sufficiently close to the target detector dose, the deviation seems not to impact the diagnostic confidence of the images. In reader studies on the respective images, radiologists could successfully determine diseased from healthy lungs (see next Chapter 6). An evaluation of the target detector dose necessary to produce images with diagnostic quality is ongoing, but a first analysis shows that the detector dose can be decreased further than what is reached with approach 2. While this does not justify the large deviations, it could serve as a reason to continue the present studies with approach 2 and develop better exposure control approaches in the future. Additionally, it has to be mentioned that the current exposure control approaches determining the tube current prior to exposure will be obsolete with systems of the next generation that feature full-field gratings. By replacing the scanning image acquisition with phase stepping again, one can imagine exposure control approaches that once again vary the exposure time based on the amount of dose registered at the detector instead of the tube current.

Power limitations X-ray source

From the normalized tube current values for lat examinations depicted in Figure 5.3, it becomes evident that the power of the X-ray tube does not suffice for the current target detector dose. With the current tube settings regarding tube voltage, tube current, frame rate, and X-ray window (see Section 3.1), the current target detector dose can be reached only for patients with a BMI up to $25.6\,\mathrm{kg\,m^{-2}}$. In contrast, the upper inclusion limit for pa examinations with the current target detector dose is at a BMI of $45.6\,\mathrm{kg\,m^{-2}}$. Nevertheless, this approach was put into action to acquire the respective lat images in the study on COVID-19 (cf. Section 3.3.1). A number of reasons legitimate the use: For once, until the start of the COVID-19 study, no image-based evaluation on a lower limit for detector doses was conducted. An ongoing evaluation hints at a diagnostic image quality at drastically reduced detector dose values. Also, post-processing steps were optimized for pa radiographs, and the lat radiographs were not yet looked at for diagnostic evaluation. As the effective patient dose is almost negligible in comparison to natural background radiation (cf. Chapter 4), we reasoned that the acquisition of the lat radiographs is of interest even if the target detector dose is not reached.

Outlook

We can conclude that of the approaches presented in this chapter, the first approach relying on the scout scan of a reference device delivers detector dose values consistent with target values, while the second approach, based on body parameters but neglect-

ing the lung's condition, does not suffice for lung diseases not considered in the original correlation study. Therefore, we recommend the use of exposure control approach 1 for further patient studies. Nevertheless, for the current study of COVID-19-pneumonia, approach 2 is sufficient to deliver images for further evaluation of the imaging technique. For new systems evaluating dark-field chest radiography with different image acquisition, we recommend approaches similar to conventional AEC, which rely on the regulation of exposure time instead of tube current modulation.

Dark-field Chest X-ray Imaging for the Assessment of COVID-19-Pneumonia

6

In this chapter, dark-field radiographs of patients with COVID-19-pneumonia are presented. As only the second pulmonary disease evaluated in humans, we assess the image appearance of COVID-19-pneumonia in dark-field radiographs. Further, a reader study was conducted to estimate the detection capability for COVID-19-pneumonia of attenuation-based images alone, dark-field images alone, and the simultaneous display of both modalities. Note that the results presented in this chapter are similarly published by Frank & Gassert et al. [Frank, 2022].

6.1 Motivation

At present, the RT-PCR test is the standard of reference for the definitive diagnosis of COVID-19 [Li, 2020; Chen, 2020]. Although the Fleischner Society recommends CT imaging in patients with COVID-19 and worsening respiratory status under certain conditions [Rubin, 2020], the use of CT as a primary screening tool is discouraged [Raptis, 2020], among other things because it is associated with a rather high radiation dose. Therefore, alternative low-dose imaging techniques for the reliable evaluation and monitoring of COVID-19-pneumonia are highly desirable. This includes the potential application for follow-up assessment of patients suffering from long-COVID-syndrome, as radiation exposure reduction is crucial, especially in the setting of repetitive scans.

6.2 Methods

6.2.1 Patient recruitment

A total of 100 patients are included in the image evaluation. Of these, 60 patients had lung changes in accordance to COVID-19-pneumonia, and 40 were healthy controls.

COVID-19 patients

Figure 6.1 illustrates COVID-19 patient selection. Between May 2020 and December 2020, 60 patients were included according to the study description outlined in Section 3.3.2, Approval 1. All CT images of potential study participants were analyzed for COVID-19 associated lung changes by two of three radiologists (with 2, 6, and 12 years of experience in chest CT imaging) immediately after the scan according to the CO-RADS assessment scheme for patients suspected of having COVID-19 [Prokop, 2020]. Only patients with a CO-RADS category 4 (suspicious for COVID-19), 5 (typical for COVID-19), or 6 (RT-PCR positive for SARS-CoV-2, if patients had been tested before the CT scan) were included in this study.

Controls

Between October 2018 and January 2020, patients of legal age (≥ 18 years) that underwent chest CT at our institution as part of their diagnostic workup were screened for study participation as described in Section 3.3.1. All CT images of potential study participants were analyzed for pathological lung changes by three radiologists (with 2, 6, and 12 years of experience in chest CT imaging). Inclusion criteria were a normal chest CT scan, the ability to consent, to stand upright without help, and to hold breath for 7 seconds. Eligible patients were approached right after the CT scan. Exclusion criteria were pregnancy, strong medical conditions, and changes in the lung tissue, such as cancer, pleural effusion, atelectasis, emphysema, infiltrates, ground glass opacities, and pneumothorax. 40 patients were included in the control group, previously reported by Gassert et al. [Gassert, 2021] and also included in Urban et al. [Urban, 2022].

CT protocol

CT was performed on one of three CT scanners (Philips iCT, Siemens SOMATOM, and Philips IQon Spectral CT) with the following parameters, according to routine clinical protocols: Reconstructed slice thickness, 0.625 mm–0.9 mm; pixel spacing, 0.4/0.3 mm; pitch factor, 0.8/0.9; tube voltage (peak), 120 kV; modulated tube current, 125 mA s–350 mA s. Images were reformatted in 3 mm slice thickness using a lung-specific kernel.

6.2.2 Image data evaluation

Four radiologists with different levels of experience in dark-field imaging (2, 5, 7, 9 years) assessed only attenuation-based radiographs, only dark-field radiographs, and both displayed simultaneously for all patients. All readers were blinded to the group

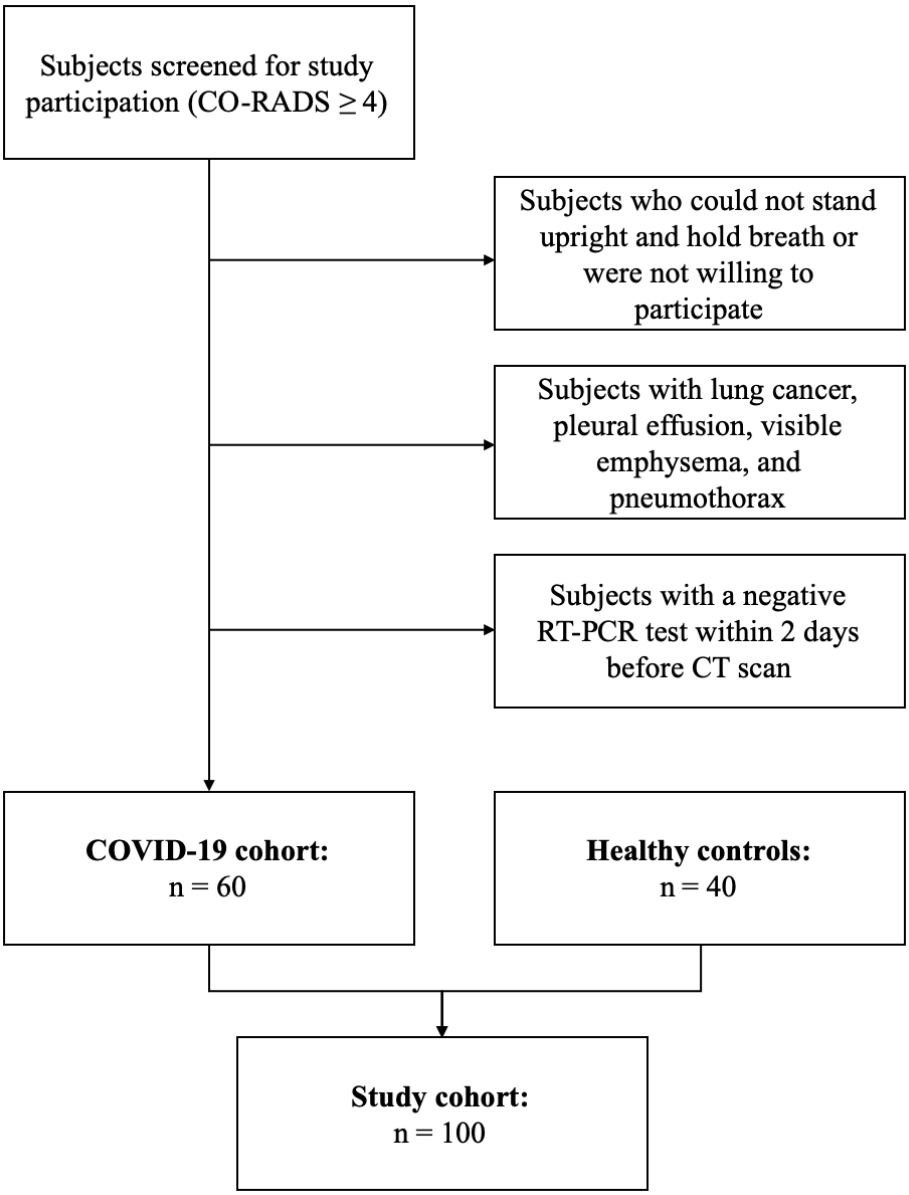

Figure 6.1: Flowchart illustrating patient selection. Subjects with a CO-RADS category $\geqslant 4$ were screened for study participation. Taking into account the exclusion criteria, 60 participants were included in the COVID-19 cohort. 40 healthy subjects formed the control group. Figure adapted from [Frank, 2022].

affiliation of images, and images were presented in random order. Readers used a PACS system and authorized monitors used in everyday clinical practice and were asked to rate the presence of COVID-19-pneumonia on a scale from 1 to 6 (1 = surely not, 2 = very unlikely, 3 = unlikely, 4 = likely, 5 = very likely, 6 = surely). Window settings were optimized for image illustration with the same window for all images within each modality. Readers were allowed to adjust window settings at their convenience. Values 1 to 3 were counted as negatives, while values 4 to 6 were counted as positives. Attenuation-based images were additionally evaluated by using the winning neural network of the SIIM-FISABIO-RSNA COVID-19 Detection Challenge [Lakhani, 2021], which provides a probability for the presence of COVID-19-pneumonia for each patient. The quantitative dark-field coefficient was calculated according to Gassert et al. [Gassert, 2021] and Urban et al. [Urban, 2022].

6.2.3 Statistical Analysis

Statistical analysis was performed with Python (version 3.8.5), specifically using the packages NumPy (version 1.20.2) [Harris, 2020] and SciPy (version 1.5.4) [Virtanen, 2020], as well as R (version 4.1.1) for the Receiver Operating Characteristic (ROC) analysis. The area under the ROC curve (AUC) was calculated for all three reading modalities, and AUC values were tested for differences with Obuchowski's method for correlated and clustered ROCdata [Obuchowski, 1997]. Additionally, a z-test based on AUC values was used to determine whether the ratings of the two groups (healthy subjects and patients with COVID-19-pneumonia) differ within each reading modality. The averaged dark-field coefficients were tested for normal distribution using the Shapiro-Wilk-test, and only the coefficient of the healthy subjects was found to follow a normal distribution. Therefore, a two-sided Mann-Whitney-U-test was applied to determine whether the two groups (healthy subjects and patients with COVID-19-pneumonia) differ in averaged dark-field coefficient. The participant's demographic parameters, age and weight, were tested for significant differences between participants with COVID-19-pneumonia and the control group using Student's t-test. For the parameter sex, a χ^2 test was used. For all tests, a 0.05 level of significance was chosen. The inter-reader reliability for the presence of COVID-19-pneumonia was rated with Cohen's weighted kappa (with quadratic weights).

6.3 Image Appearance

A total of 100 patients (56 men, 44 women) were included, of which 40 were healthy controls [Gassert, 2021] and 60 had COVID-19-pneumonia. Demographics of all study participants are listed in Table 6.1. No differences were found between healthy controls

and patients with COVID-19-pneumonia regarding sex, age, and weight.

Parameter	All	Healthy	COVID-19	p-value
Number of participants	100	40	60	
Men / Women	59 / 41	25 / 15	34 / 26	0.56
Age in years	58 ± 14	61 ± 12	57 ± 15	0.18
Weight in kg	79 ± 16	79 ± 13	79 ± 16	0.89

Table 6.1: Subject demographics. Values are given as mean ± standard deviation. P-values for the significance of differences between the COVID-19 group and the healthy controls are listed in the very right column. The 40 healthy subjects were also included in Gassert et al. [Gassert, 2021] and Urban et al. [Urban, 2022].

Figure 6.2 and Figure 6.3 show X-ray dark-field imaging results on COVID-19 patients. Figure 6.2 depicts dark-field (A, C) and attenuation radiographs (B, D) of a healthy participant (A, B) and subject with COVID-19-pneumonia (C, D). Figure 6.3 depicts imaging results of four additional patients infected with COVID-19, more precisely, further attenuation images (A-D), dark-field images (E-H), and respective coronal CT slices of the patient (I-L). Compared to dark-field images in healthy subjects (Figure 6.2A), those in patients with typical COVID-19-pneumonia in the CT scan showed an overall decrease of the dark-field signal (Figure 6.2C, Figure 6.3E-H). While dark-field images in healthy subjects exhibit a relatively homogeneous structure [Gassert, 2021], images of COVID-19 patients appear rather inhomogeneous and patchy, especially in the lung periphery. Whereas changes are evident in dark-field images, conventional X-ray images of healthy subjects (Figure 6.2B) and infected patients (Figure 6.2D, Figure 6.3A-D) are difficult to distinguish.

Figure 6.3I-L also depicts coronal slices of four patients' respective CT. Patchy appearances in the dark-field images correspond well to ground-glass opacities and consolidated areas in the respective CT scan, proving that COVID-19-pneumonia causes the patches in the dark-field images. A quantitative evaluation of how well the dark-field images correspond to the respective CT was carried out by Gassert & Bast et al. [Gassert, Submitted], the corresponding paper is in preparation at the time of writing this thesis. For that purpose, amongst a reader study, they projected the three-dimensional CT with COVID-19-afflicted voxel marked in red along the sagittal axis to generate a two-dimensional overlay of the CT-based attenuation image with the projected thickness of diseased lung in a two-dimensional color map. They concluded that the detection and visualization of COVID-19-pneumonia in dark-field images correlates

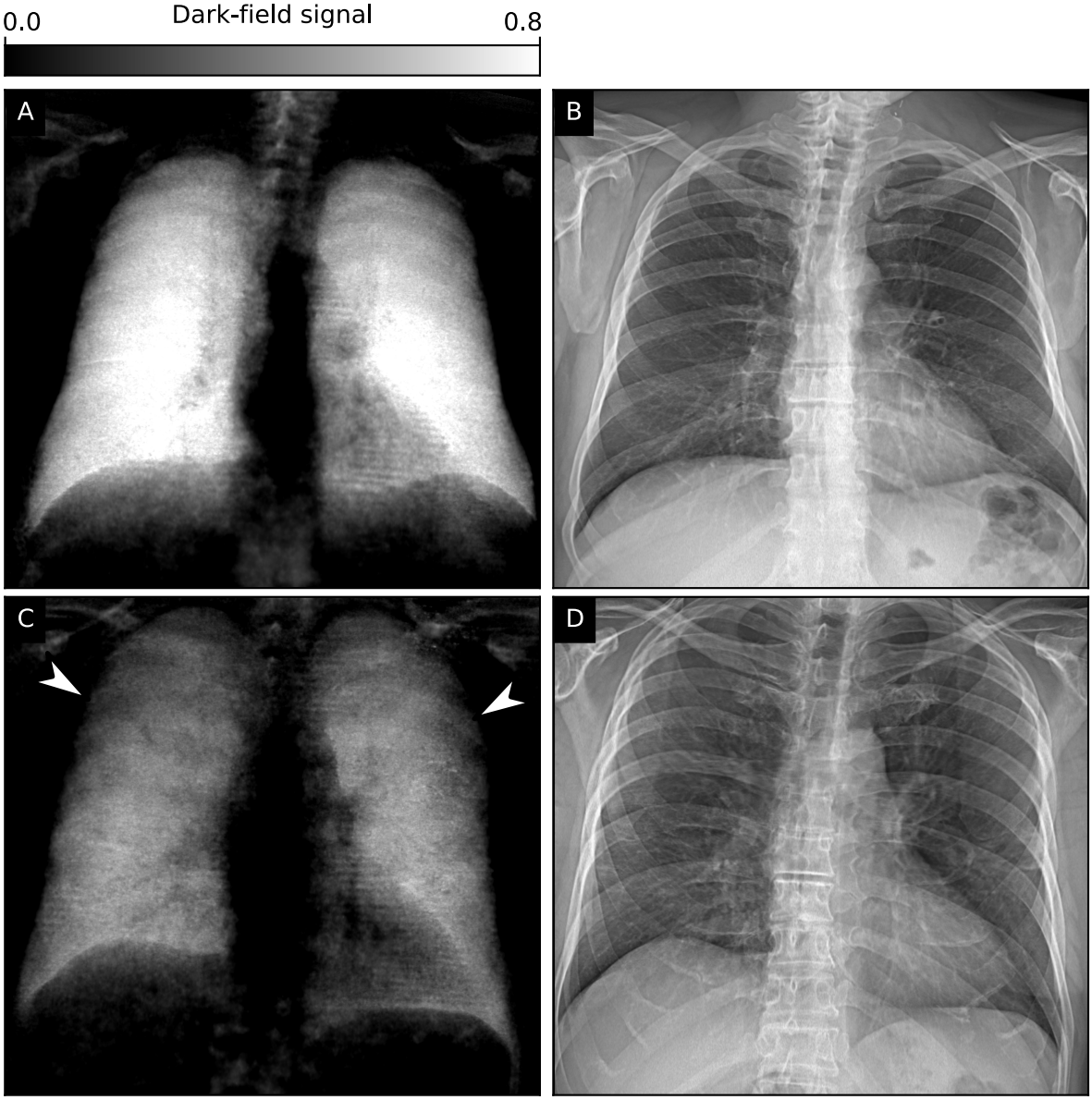

Figure 6.2: Dark-field and attenuation chest X-rays of healthy and COVID-19-infected subjects. A, Dark-field and B, conventional (attenuation-based) chest radiographs of a healthy subject. The dark-field radiograph exhibits a strong, homogeneous dark-field signal. The respective attenuation-based image shows no apparent pathology. C, Dark-field and D, attenuation-based chest radiographs of a patient infected with COVID-19. Compared to the healthy subject, the infected patient shows an overall decrease in signal intensity. While the signal of the healthy subject is homogeneous, the dark-field signal of the infected patient appears inhomogeneous and patchy, especially in the periphery of the lung (arrowheads). Figure adapted from [Frank, 2022].

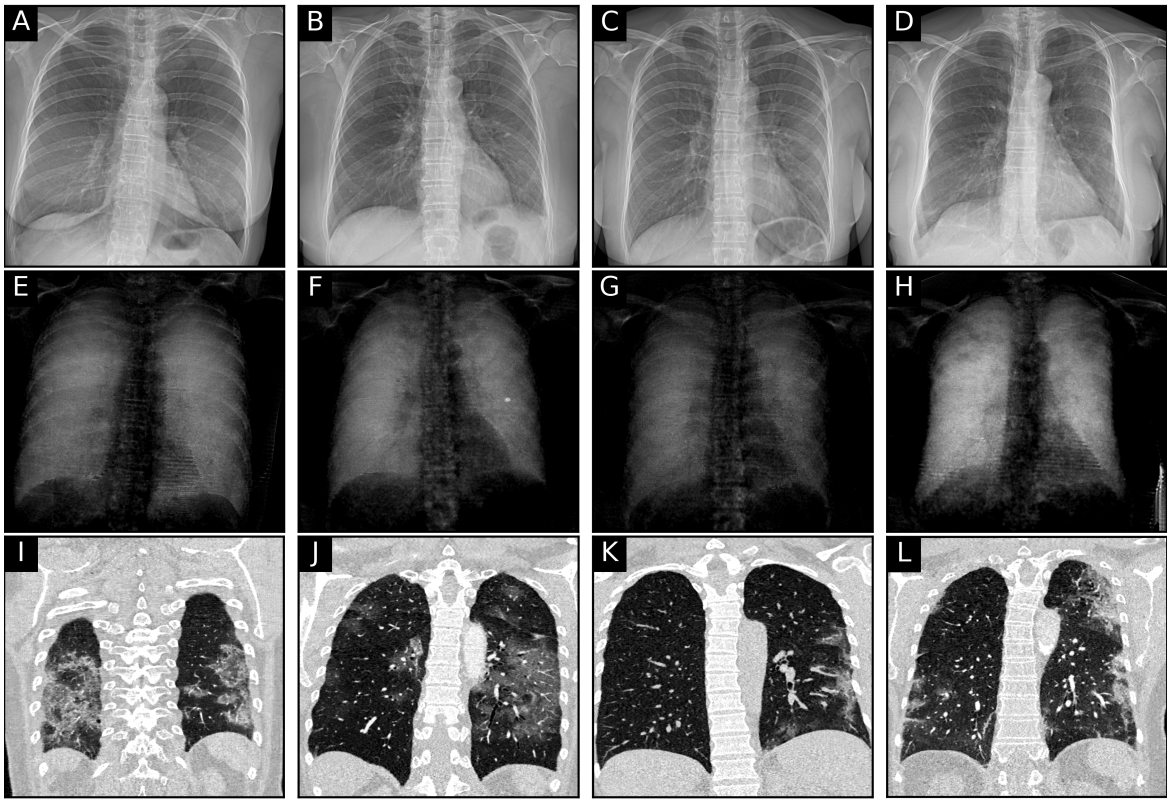

Figure 6.3: Dark-field and attenuation chest X-ray images compared to CT information for four selected patients. A-D, Dark-field images, E-H, attenuation images, and I-L, coronal CT slices of four patients with COVID-19-pneumonia. Each column depicts the different images of one patient. Although sometimes difficult to determine in attenuation radiographs, the locations of consolidations visible in the CT slices correspond to areas with reduced dark-field signal.

well with their localization in CT images.

6.4 Reader Study and Quantitative Analysis

To evaluate the potential clinical impact, we performed a reader study for the detection of COVID-19-pneumonia on both attenuation-based and dark-field images alone, as well as both images displayed simultaneously. The ratings for the presence of COVID-19-pneumonia in healthy subjects and patients with COVID-19-pneumonia in the CT scan did show a highly significant difference for all displayed variations, attenuation-based, dark-field-based, and the combination of both ($p < 0.05$ for all) (Figure 6.4A).

Overall rating values for the presence of COVID-19-pneumonia in infected patients were substantially higher for dark-field imaging (4.84 ± 1.39) compared to attenuation-based imaging (3.16 ± 1.46). Additionally, rating values for infected patients were higher for the combination of dark-field-based and (conventional) attenuation-based imaging (5.04 ± 1.37) compared to dark-field based imaging alone. In a ROC analysis for the differentiation between infected patients and healthy subjects, the effect size expressed as the AUC was 0.78 (95 % confidence interval (CI) 0.73 to 0.83) for attenuation-based radiographs, 0.91 (95 % CI 0.88 to 0.94) for dark-field images and 0.93 (95 % CI 0.91 to 0.96) for the combination of both (Figure 6.4B). By including dark-field images, AUC values were significantly higher compared to attenuation images only ($p < 0.001$ for dark-field alone and for the combination). These results are also listed in Table 6.2.

	Attenuation	Dark-field	Attenuation & Dark-field
Overall rating values	3.16 ± 1.46	4.84 ± 1.39	5.04 ± 1.37
AUC (95 % CI)	0.78 (0.73–0.83)	0.91 (0.88–0.94)	0.93 (0.91–0.96)
Overall sensitivity (95 % CI)	0.43 (0.38–0.48)	0.86 (0.80–0.92)	0.88 (0.82–0.94)

Table 6.2: Overall rating values, AUC, and overall sensitivity for all three reading modalities.

For comparison, we additionally applied the winning neural network of the SIIM-FISABIO-RSNA COVID-19 Detection Challenge [Lakhani, 2021], trained on conventional attenuation images, to the attenuation images of both the COVID-19 patients and healthy controls. In this setting, an AUC value of 0.88 was achieved, which can also be found in literature [Hurt, 2022]. This value was higher than the AUC achieved by readers on the same images. However, compared to the trained network, readers

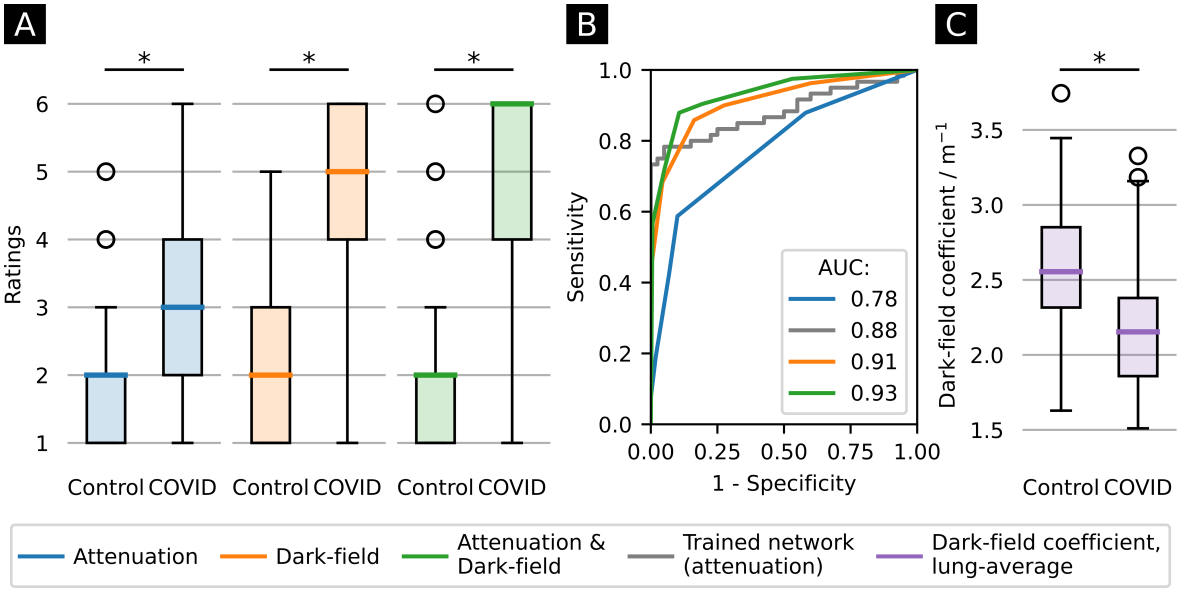

Figure 6.4: Results of clinical evaluation and statistical analysis. A, Reader scores for both healthy subjects and infected patients in dark-field based (blue), attenuation-based (orange), and dark-field- & attenuation-based (green) readings. B, Receiver Operating Characteristic (ROC) analysis for the respective modalities for the differentiation between infected patients and healthy subjects. Additionally, an AI algorithm (trained neural network) for COVID-19-pneumonia detection was applied for attenuation image evaluation. AUC values were 0.78 (attenuation), 0.88 (trained network on attenuation), 0.91 (dark-field), and 0.93 (dark-field & attenuation), respectively. C, Objective, quantitative image analysis, showing the average dark-field coefficient (integrated over the whole lung area and evaluated after segmentation) for the lungs of healthy subjects and infected patients. Significant differences are indicated by asterisks: *, $p < 0.05$. Abbreviations: AUC, area under the curve. Figure adapted from [Frank, 2022].

achieved an even higher AUC when reading dark-field images alone or the combination of both imaging modalities (Figure 6.4B).

The overall sensitivity for COVID-19-pneumonia was 0.43 (95 % CI 0.38 to 0.48) for attenuation-based images, 0.86 (95 % CI 0.80 to 0.92) for dark-field images, and 0.88 (95 % CI 0.82 to 0.94) for the combination of both. Respective specificities and accuracies, also on an individual reader basis, are shown in Table 6.3. The inter-rater reliability between the readers ranged 0.16–0.42 for attenuation-based imaging, 0.56–0.67 for dark-field imaging, and 0.48–0.74 for the combination of both. Reader-specific reliability scores are provided in Table 6.4. The average image quality rating over all readers was 4.97 ± 0.99 for dark-field and 5.35 ± 0.66 for attenuation-based imaging.

	Reader	Sensitivity	Specificity	Accuracy
Attenuation	1	0.50	0.84	0.63
	2	0.33	0.98	0.59
	3	0.38	1.00	0.63
	4	0.48	0.98	0.68
	Overall	0.43	0.93	0.63
Dark-field	1	0.92	0.95	0.93
	2	0.95	0.90	0.93
	3	0.92	0.88	0.90
	4	0.65	0.78	0.70
	Overall	0.86	0.84	0.85
Attenuation & Dark-field	1	0.93	0.97	0.95
	2	0.90	0.95	0.92
	3	0.88	0.95	0.91
	4	0.80	0.86	0.82
	Overall	0.88	0.89	0.89

Table 6.3: Sensitivity, specificity, and accuracy for each reader individually and overall, for all three reading modalities.

For a quantitative analysis of the dark-field signal, we calculated the average dark-field coefficient of every patient's lung, corresponding to the average dark-field signal

generated per path length through the lung parenchyma [Gassert, 2021]. The average dark-field coefficient was significantly lower in patients infected with COVID-19 ($(2.15 \pm 0.44)\,\mathrm{m}^{-1}$) compared to healthy subjects ($(2.53 \pm 0.44)\,\mathrm{m}^{-1}$, p = 8.6e-5), as depicted in Figure 6.4C.

	Attenuation	Dark-field	Attenuation & Dark-field
Reader 1 & Reader 2	0.27	0.56	0.48
Reader 1 & Reader 3	0.38	0.67	0.63
Reader 1 & Reader 4	0.36	0.57	0.59
Reader 2 & Reader 3	0.16	0.62	0.74
Reader 2 & Reader 4	0.22	0.65	0.66
Reader 3 & Reader 4	0.42	0.66	0.74

Table 6.4: Inter-rater reliability expressed with Cohen's quadratic weighted kappa.

6.5 Discussion

Reader Study Findings

In this study, we present the first application of the recently developed dark-field X-ray imaging technology for the assessment of COVID-19-pneumonia and demonstrate its superiority over conventional radiography. This essentially introduces a low-radiation, medical imaging alternative to present CT imaging for COVID-19-pneumonia detection and potentially therapy follow-up. It allows for the reliable detection of COVID-19-pneumonia and is, in that respect, superior to conventional radiography. For the latter, our results are in line with a previous study by Self et al. [Self, 2013], who found a similar sensitivity for the detection of pulmonary opacities in conventional attenuation radiographs as we found for attenuation images.
In the performed reader study, the simultaneous presentation of both attenuation and dark-field images yielded the highest sensitivity of all reading modalities. The combined information from both attenuation and dark-field images provide an even better picture of the ventilation situation of the lung, also reflected by the higher inter-rater reliability for the combination of both imaging modalities compared to each imaging modality separately. Even though the achieved sensitivity when reading both modalities is not as high as in CT imaging [Self, 2013], it is still reasonably high and comes with only a

fraction of the dose.
We included only patients with moderate courses of the disease who could stand upright and their hold breath for the duration of the scan. These patients could be clearly distinguished from healthy controls. This underlines the technique's potential to detect even minor lung changes such as ground glass opacities.

Dark-field Imaging outperformed Neural Network

The applied neural network was trained on publically available conventional attenuation images, which are acquired at a higher tube voltage than what is used at the dark-field prototype system. An evaluation of the performance for images obtained with the dark-field prototype system was performed, and its applicability to the images acquired here is presented in the Appendix A.1.

Within this study, the evaluation of attenuation images alone was enhanced by the trained neural network. Both the results of the readers and the neural network on attenuation images are comparable to literature values [Self, 2013; Hurt, 2022]. The higher AUC values for the trained neural network compared to readers were expected. Nevertheless, the reader-based assessment of dark-field images outperforms the algorithm, highlighting the additional diagnostic information obtained by dark-field chest radiography. We are confident that there is potential to further enhance these results by applying artificial intelligence on dark-field images once a sufficiently large number of cases is available for training.

Limitations

The patient study also exhibits some limitations. The study cohort, comprising 100 subjects, is presently relatively small, and the technique must be further evaluated in future studies with larger cohorts. Another drawback in this context is also that potential pulmonary comorbidities in COVID-19-patients are not taken into account, while the control group comprised only healthy subjects without any pulmonary disorders. While this initial pilot study aimed at evaluating the accuracy of X-ray dark-field imaging for the detection of COVID-19-pneumonia compared to pulmonary healthy subjects, future studies must be performed to evaluate the technique for the assessment of the lung when other pathologies are present.
Currently, no pixel-based analysis is available, as the projected lung thickness in each pixel, which is necessary for the normalization of the dark-field signal with the respective lung thickness, remains unknown. Therefore, only the average dark-field coefficient of the whole lung is available as the total signal is normalized with the lung volume. This leads to only a small reduction of the average dark-field coefficient in the presence

of beginning and localized pneumonia, while the dark-field images show a distinct localized signal decrease in these cases. Whereas the quantitative analysis does not allow for the assessment of local changes in dark-field signal, radiologists may detect patterns of local signal losses. Future studies are needed to analyze the dark-field signal locally and therefore allow for a quantitative assessment of the alveolar integrity on a pixel basis.

Potential further Evaluations

More patient studies are needed to evaluate the technique's potential for the imaging of COVID-19-pneumonia. Dark-field imaging might, for example, also be suitable for disease and treatment monitoring of COVID-19 patients due to the obtained image-based information on the lung's alveolar condition at a low effective patient dose. With constantly new variants increasingly leading to higher infection rates [Mahase, 2021], and severe courses in younger patients [Taylor, 2021], dark-field imaging might be a low-radiation alternative for disease monitoring, especially in patients where repetitive CT scans should be avoided. Low-dose imaging techniques such as dark-field radiography are also highly desirable for the assessment of pulmonary involvement in patients with long-COVID-syndrome. However, this potential use case of the presented method is yet to be evaluated. Nevertheless, the presented study highlights the potential of dark-field chest X-ray imaging for the assessment of COVID-19-pneumonia and shows that it might be a promising new tool in the fight against the SARS-CoV-2 pandemic.

7 Conclusion and Outlook

The first clinical prototype system for dark-field chest radiography was approved and commenced operation during the time of this PhD project. It is now possible for the first time to acquire novel dark-field X-ray images of the human lung within clinical boundary conditions. In this work, the diagnostic value and effective dose associated with dark-field chest radiography with this system for patients were evaluated, and the superior performance of the additional image information is demonstrated.

The physical fundamentals of X-rays and their interaction with matter are presented in Chapter 2. Furthermore, grating-based X-ray imaging is introduced on which the clinical prototype is based. The concepts of dosimetry and the regulatory parameters concerning exposure control are introduced, along with the medical background relevant to X-ray dark-field chest imaging. This chapter forms the basis and provides the theoretical background for all work conducted within the scope of this PhD thesis.

An overview of the clinical system for dark-field chest radiography is given in Chapter 3, but the design aspects and implementations are discussed more extensively in the doctoral thesis of my former colleague, Konstantin Willer [Willer, 2022]. The present work introduces the setup and describes the image processing steps in short. Further, the specifications of the two patient studies used later in this thesis are defined.

The dosimetry conducted at the clinical dark-field system is presented in Chapter 4. We found that the effective dose deposited into the reference man, modeled by an anthropomorphic phantom, accumulates to 35 µGy. This value is within current literature values for chest radiography, as are the recorded dose values for the examined patient cohort. By demonstrating that dark-field chest imaging is possible in a dose-compatible way, we opened up the possibility of examining the potential of dark-field chest radiography on humans on a broad scale.

Since the system uses a scanning image acquisition, conventional automatic exposure control (AEC) employed in commercially available radiography systems cannot be used. We established two approaches for exposure control at the clinical prototype system, presented in Chapter 5. The first approach is based on an additional chest radiograph taken at a commercial system with AEC acting as a scout scan. Based on exposure settings from the AEC, we used a calibration function to model the human chest as

an equivalent attenuator of POM of a certain thickness. In turn, we determined the exposure settings at the dark-field system to reach a target detector dose for that POM thickness. This first approach works well within regulatory requirements, independent of the imaged subject's body parameters.
The second approach is based on a correlation between the person's BMI and the tube current necessary to reach the target detector dose. This approach was also implemented and used for a patient study. Here we find considerably larger deviations, partly because the correlation was evaluated for participants with a healthy lung or a disease that decreases the lung's attenuation, while we employed this approach for patients with a disease that consolidates the lung. The resulting images still have a diagnostic quality. Nevertheless, I strongly recommend using the first approach for this system whenever a conventional radiograph is part of the study.

In Chapter 6 we presented the application of clinical dark-field chest radiography for the assessment of COVID-19-pneumonia. In contrast to healthy lungs, the dark-field signal is reduced in areas corresponding to ground glass opacities visible in the accompanying CT. In a reader study, we found that dark-field imaging has a higher sensitivity for COVID-19-pneumonia than attenuation-based imaging and that the simultaneous display of both is superior to one imaging modality alone. Furthermore, a quantitative image analysis shows a significant reduction of dark-field signals for COVID-19 patients. These results highlight the potential of dark-field chest X-ray imaging for disease and treatment monitoring of COVID-19 patients. Its low radiation dose might be especially valuable for patients where repetitive CT scans should be avoided.

Outlook

As illustrated in Chapter 6, dark-field X-ray imaging outperforms conventional radiography for the assessment of COVID-19-pneumonia. Other publications demonstrate that the quantitative dark-field coefficient in chest radiographs of healthy subjects is independent of demographic subject parameters [Gassert, 2021] but is decreased in the presence of pulmonary emphysema [Urban, 2022]. Further, dark-field chest radiography can detect structural impairment associated with COPD [Willer, 2021], and findings in dark-field radiographs are superior for staging of emphysema compared to conventional radiography [Urban, Submitted].

All these results are very promising and highlight the technique's potential to facilitate the detection of pulmonary diseases. Dark-field radiography proved diagnostic benefit for COPD and COVID-19-pneumonia, and consequently further patient studies on other pulmonary disorders will be investigated. At the time of writing, two new patient studies on the detection of pneumothoraces and lung tumors have started. Even more successful patient studies on other lung pathologies are beneficial for the radiology

community to fully accept dark-field chest radiography. These should include more participants and be conducted with different systems at multiple locations. With enough clinical evidence, a widespread application of dark-field chest radiography can take place.

While the prototype system employed in this work enables the acquisition of both dark-field and attenuation radiographs with diagnostic image quality, the system needs further advancement in order to be authorized for commercial application. At the moment, not all regulatory standards for chest radiography are fulfilled. For one, the default resolution necessary for chest radiographs is not met due to the employed binning (see Chapter 3) [Saure, 2008]. In newer-generation detectors, the read-out time might be improved to overcome the need for binning. Also, the image acquisition time of about 7 s exceeds the specified acquisition time for chest radiographs of ≤ 20 ms [Saure, 2008]. The latter issue could be resolved by installing gratings that cover the entire field of view, so-called full-field gratings. By doing so, scanning image acquisition can be abandoned in favor of phase stepping (see Chapter 2), enabling faster image acquisition. The outlined modifications will help license dark-field chest radiography systems and make them commercially available.

Another benefit of employing full-field gratings could be using other exposure control mechanisms that are more closely related to conventional AEC. Instead of adapting the tube current beforehand, the exposure time can be regulated depending on the measured detector dose during the image acquisition. This can help to deliver constant detector dose values for all lung diseases.

Dark-field chest radiography is a projection-based imaging technique, resulting in a two-dimensional projection of the human thorax. For three-dimensional information, dark-field CT has to be employed. Recently, the first human-scale dark-field CT system was realized [Viermetz, 2022a; Viermetz, 2022b]. Results of dark-field CT in a human patient are anticipated to fuel the community's interest in X-ray dark-field imaging for the assessment of pulmonary diseases.

Finally, I personally believe that dark-field imaging provides additional value for chest radiography, as it enables the acquisition of information on the lungs' microstructure that is not accessible with other imaging methods. Further patient studies will underline the technique's potential on a broader scale, and I am confident that dark-field chest radiography will become a standard procedure in the future.

A Appendix

A.1 SIIM-FISABIO-RSNA COVID-19 Detection Challenge

The here applied neural network of the SIIM-FISABIO-RSNA COVID-19 Detection Challenge [Lakhani, 2021] was trained on publicly available conventional attenuation images. These conventional attenuation X-ray images are usually acquired at high tube voltages of about 120 kV–125 kV [Uffmann, 2005]. To evaluate if the network is also applicable to the attenuation images acquired from the clinical dark-field prototype system with lower tube voltages, the algorithm was applied to participants that were imaged both at the dark-field prototype system and the commercially available radiography system (DiDi). Therefore, only participants of the COPD study were eligible. As the training data set for the neural network did not include pulmonary emphysema cases, only the healthy participants were chosen for the performance evaluation. As a result, the algorithm was applied to the images of the 40 healthy participants of the COPD study (also included in Gassert et al. [Gassert, 2021]). Only the true negativ rate and the false positive rate of the neural network could be determined, as only healthy participants were included. Nevertheless, rates for both imaging systems were calculated. For this purpose, the differentiation threshold for the decision was set to 0.5.

Resulting performance rates are listed in Table A.1, along with the performance of the readers as presented in Section 6.4. The neural network achieved a higher true negativ (TN) rate for the radiographs acquired at the clinical dark-field prototype system than at the commercial system. The readers still outperformed the neural network on attenuation images of healthy participants only.

	TN	FP	TP	FN
NN DiDi	0.575	0.425		
NN DF	0.8	0.2		
Reader 1	0.875	0.125	0.317	0.683
Reader 2	0.975	0.025	0.5	0.5
Reader 3	0.9	0.1	0.282	0.616
Reader 4	0.975	0.025	0.5	0.5

Table A.1: Performance comparison between neural network and readers. The decision threshold was set to 0.5 for the neural network (on a scale from 0–1), and to 3.5 for the readers (on a scale from 1–6). Abbreviations: TN, true negativ; FP, false positive; TP, true positive; FN, false negativ; NN, neural network; DiDi: Digital Diagnost (commercial system); DF: Dark-field prototype system.

A.2 List of Abbreviations

AEC	automatic exposure control
AI	artificial intelligence
AUC	area under the ROC curve
BfS	Bundesamt für Strahlenschutz (*Federal Office for Radiation Protection*)
BMI	body mass index
CI	confidence interval
COPD	Chronic Obstructive Pulmonary Disease
CO-RADS	COVID-19 Reporting and Data System
COVID-19	Coronavirus Disease 2019
CT	computed tomography
CNR	contrast-to-noise ratio
DAP	dose-area product
DI	deviation index
DiDi	Digital Diagnost
DRL	Diagnostic Reference Level
EI	Exposure Index
EIT	target Exposure Index
FN	false negativ
FP	false positive
FOV	field of view
ICRP	International Commission of Radiological Protection
KAP	air kerma-area product

kerma	Kinetic Energy Released per Unit Mass
lat	lateral
pa	posterior-anterior
PACS	Picture Archiving and Communication System
PCD	photon-counting detector
POM	polyoxymethylene
ROC	Receiver Operating Characteristic
ROI	region of interest
RT-PCR	Reverse Transcription Polymerase Chain Reaction
SARS-CoV-2	Severe Acute Respiratory Syndrome Coronavirus 2
SD	standard deviation
SNR	signal-to-noise ratio
TLD	thermoluminescent dosimeter
TN	true negativ
TP	true positive
WHO	World Health Organization

B Publications and Scientific Presentations

Publications as first author

M. Frank, T. Urban, K. Willer, W. Noichl, F. De Marco, R. Schick, B. Gleich, A. Schegerer, U. Lechel, P. Mayer, J. Mohr, T. Koehler, A. Yaroshenko, I. Maack, T. Pralow, B. Renger, P. Noël, A. Fingerle, D. Pfeiffer, E. Rummeny, J. Herzen & F. Pfeiffer. Dosimetry on First Clinical Dark-Field Chest Radiography. *Med Phys.* **14**(10):e0222816 (2021).

M. Frank*, F. Gassert*, T. Urban, K. Willer, W. Noichl, R. Schick, M. Schultheiss, M. Viermetz, B. Gleich, F. De Marco, J. Herzen, T. Koehler, K. J. Engel, B. Renger, F. Gassert, A. Sauter, A. Fingerle, B. Haller, M. Makowski, D. Pfeiffer & F. Pfeiffer. Dark-field Chest X-ray Imaging for the Assessment of COVID-19-Pneumonia. *Commun Med* **2**, 147 (2022).

F. Gassert*, **M. Frank***, F. De Marco, K. Willer, T. Urban, J. Herzen, A. Fingerle, A. Sauter, M. Makowski, F. Kriner, F. Fischer, C. Braun, F. Pfeiffer & D. Pfeiffer. Assessment of Inflation in a Human Cadaveric Lung by Dark-field Chest Radiography. *Radiology: Cardiothoracic Imaging* **4.** doi:10.1148/ryct.220093 (2022).

M. Frank*, K. Willer*, T. Urban, W. Noichl, R. Schick, F. De Marco, T. Koehler, I. Maack, D. Pfeiffer, B. Renger & F. Pfeiffer. Exposure Control at First Dark-Field Chest Radiography Demonstrator System. *In Review at Medical Physics.*

Publications as Co-author

A. Sauter*, J. Andrejewski*, **M. Frank**, K. Willer, F. Meurer, A. Fingerle, M. Makowski, F. Pfeiffer & D. Pfeiffer. Correlation of image parameter and tube voltage in X-ray dark-field chest radiography: results of the first human in-vivo scanner. *Scientific Reports* **5**(10):106108 (2021).

F. Gassert*, T. Urban*, **M. Frank**, K. Willer, W. Noichl, P. Buchberger, R. Schick, T. Koehler, A. Fingerle, A. Sauter, D. Pfeiffer, M. Makowski & F. Pfeiffer. Qualitative and Quantitative Characteristics of Dark-Field X-ray Imaging in Healthy Patients. *Radiology* **301**, 389–395 (2021).

K. Willer*, A. Fingerle*, W. Noichl, F. De Marco, **M. Frank**, T. Urban, R. Schick, A. Gustschin, B. Gleich, J. Herzen, T. Koehler, A. Yaroshenko, T. Pralow, G. Zimmermann, B. Renger, A. Sauter, D. Pfeiffer, M. Makowski, P. Grenier & F. Pfeiffer. X-ray dark-field chest imaging for detection and quantification of emphysema in patients with chronic obstructive pulmonary disease: a diagnostic accuracy study. *The Lancet Digital Health* **3**, e733–e744 (2021).

R. Schick, T. Koehler, W. Noichl, F. De Marco, K. Willer, T. Urban, **M. Frank**, T. Pralow, I. Maack, S. Prevrhal, B. Lundt, A. Fingerle, D. Pfeiffer, J. Herzen & F. Pfeiffer. Correction of Motion Artifacts in Dark-Field Radiography of the Human Chest. *IEEE Transactions on Medical Imaging* **8**:15700 (2021).

J. Andrejewski, F. De Marco, K. Willer, W. Noichl, T. Urban, **M. Frank**, A. Gustschin, P. Mayer, T. Koehler, F. Pfeiffer & J. Herzen. Retrieval of 3D information in X-ray dark-field imaging with a large field of view. *Scientific Reports* **11.1** 1-8. (2021).

T. Urban*, F. Gassert*, **M. Frank**, K. Willer, W. Noichl, P. Buchberger, R. Schick, T. Koehler, J. Bodden, A. Fingerle, A. Sauter, M. Makowski, F. Pfeiffer & D. Pfeiffer. Qualitative and Quantitative Assessment of Emphysema Using Dark-field Chest Radiography. *Radiology* **303**, 119-127 (2022).

G. Zimmermann*, A. Fingerle*, B. Renger, H. Hautmann, A. Sauter, F. Meurer, F. Gassert, J. Bodden, C. Müller-Leisse, M. Renz, E. Rummeny, M. Makowski, K. Willer, W. Noichl, F. De Marco, **M. Frank**, T. Urban, R. Schick, J. Herzen, T. Koehler, B. Haller, D. Pfeiffer & F. Pfeiffer. Dark-Field Chest X-Ray Imaging: First experience in Patients with α1-Antitrypsin Deficiency. *European Radiology Experimental* **6**, 9 (2022).

W. Noichl, F. De Marco, K. Willer, T. Urban, **M. Frank**, R. Schick, B. Gleich, L. Hehn, A. Gustschin, P. Mayer, J. Mohr, T. Koehler, I. Maack, K. J. Engel, B. Lundt, B. Renger, A. Sauter, D. Pfeiffer, E. Rummeny, J. Herzen & F. Pfeiffer. Correction for mechanical inaccuracies in a scanning Talbot-Lau interferometer. *In Review at IEEE Transactions on Medical Imaging.*
Preprint available at `https://doi.org/10.36227/techrxiv.21201475.v1`.

M. Kattau, K. Willer, W. Noichl, T. Urban, **M. Frank**, F. De Marco, R. Schick, J. Herzen, T. Koehler, I. Maack, B. Renger, M. Renz, A. Sauter, Y. Leonhardt, A. Fingerle, D. Pfeiffer, M. Makowski & F. Pfeiffer. Chest Radiography: A Reader Study to Evaluate the Diagnostic Quality of Attenuation Images Acquired with a Dual-Contrast Scanning Prototype Operated at 70 kVp. *Eur Radiol* (2023).

T. Urban*, A. Sauter*, **M. Frank**, K. Willer, W. Noichl, R. Schick, J. Herzen, T. Koehler, F. Gassert, J. Bodden, A. Fingerle, B. Gleich, B. Renger, M. Makowski, D. Pfeiffer & F. Pfeiffer. Emphysema Diagnosis and Staging with Conventional and Dark-field Radiographs. *Accepted at Investigative Radiology.*

F. Gassert*, H. Bast*, T. Urban, **M. Frank**, F. Gassert, K. Willer, R. Schick, B. Renger, T. Koehler, A. Sauter, A. Fingerle, M. Makowski, F. Pfeiffer & D. Pfeiffer. Comparison of Dark-field Chest Radiography and CT for the Assessment of COVID-19 Pneumonia. *Submitted to Physica Medica.*

* Shared first authorship

Oral presentation

Dosimetry for Combined Dark-Field & Attenuation Chest X-ray Imaging on Patients. *International Workshop on X-ray and Neutron Phase Imaging with Gratings (XNPIG), Sendai, Japan, October 2019.*

Dosimetry for Combined Dark-Field & Attenuation Chest X-ray Imaging on Patients. *Annual Meeting of the Radiological Society of North America (RSNA), Chicago, USA, December 2019.*

Dark-field Chest Radiography: Dose Values in First Patients Studies. *International Symposium on Biomedical Applications of X-ray Phase-Contrast Imaging (IMXP), Munich, Germany, January 2020.*

Strahlendosis beim Dunkelfeld-Röntgen. *Jahrestagung der Deutschen Gesellschaft für Medizinische Physik (DGMP), online, September 2020.*

Determination of Dose Parameters. *Joint Conference of the ÖGMP, DGMP and SGSMP - Dreiländertagung der Medizinischen Physik, online, September 2021.*

Poster presentations

Dark-field Chest Radiography: Dose Values in First Patients Studies. *European Congress of Radiology (ECR), online, July 2020.*

Dark-Field Chest Radiography improves the Detection of COVID-19-pneumonia. *European Congress of Radiology (ECR), online, March 2022 & Vienna, Austria, July 2022.*

C Acknowledgements

Thank you, Franz, for giving me the opportunity to write my PhD thesis on this exciting project. Not only did you take me on for my master's thesis, but allowing me to continue with the PhD. You enabled the team and, therefore, me to work in fruitful cooperation with Philips, attend many international conferences, work with functioning infrastructure and equipment, and supported me when I wanted to gain more international experiences or when searching for a job. Thank you for your trust and constant support!

A special thanks to the staff that ensures everyone at E17 can keep working smoothly. Thank you, Martin and Klaus, for always being quick and patient to answer any question and keep the infrastructure running. Dear Veronica, thank you for your help with all administrative tasks at the clinics and constant support for all projects, and mostly thank you, Nelly, for being so patient and helpful, independent of the questions or how often they are asked.
Thank you, Wolfgang, for helping with IT-realted topics far more than what can be expected.

Thank you, Konsti, Theresa, Wolfgang, Rafael, and Henriette. Without all of you, the Patient Scanner, or clinical dark-field prototype, would not exist as it does. Thanks for many fruitful discussions, great teamwork, countless papers, and keeping up the balance between work and fun.

Many thanks again to Theresa and Henriette for proofreading this thesis. I appreciate it, and the thesis was improved with your help, even when I complained about the many comments.

Huge thanks to the medical team at *Klinikum rechts der Isar*, without whom it would have been impossible to conduct the clinical research. Thank you, Daniela, for working on bureaucratic stuff so we can focus on the research, and thank you, Alex and Andi, for overseeing the clinical studies. Thank you, Flo, for being the most motivated physician we could have hoped for; without you everything would have taken so much longer, and thanks for letting us glimpse into the daily clinic life! Thanks to all the other radiologists who helped acquire and image the study participants.

Special thanks to the team at Philips Research. Mainly Thomas, thanks for your valuable feedback and new ideas for all projects; without you, things would be less scientific.

Many thanks to the MAXS Team: Theresa, Konsti, Wolfgang, and Jule. Although it didn't turn out the way we had hoped, it was a fun, memorable, and educational experience. Thank you for not only getting deep into the entrepreneurial mindset while working on disruptive and exciting technology but also learning about my own plans, dreams, and talents.

I also want to acknowledge the master students Maggie, Henriette, and Jule, whom I (co-)supervised. It was great having you on the team.

Thank you, Bernhard, David, Felix, and Christiane, for your help with the IT of the radiology department, and your knowledge and support concerning all regulatory affairs necessary to keep a clinical radiography system running.

Also, thank you, Powerpuff Girls, for being the awesome friend group that you are. I am looking forward to our next trips!

Thank you, every other member of E17, for fruitful discussions, coffee breaks, playing Kicker, and all in all, making this a memorable time.

Big thanks to my family, for enabling me to continue on this track, supporting me in all my decisions, listening to my complaints, and always having my back.
Thank you, Jacob, for your love, help, and encouragement.

Bibliography

[Artz, 1997] Artz, D. S. Computed radiography for the radiological technologist. *Seminars in Roentgenology* **32,** 12–24 (1997) (Cited on page 43).

[Bech, 2013] Bech, M. *et al.* In-vivo dark-field and phase-contrast x-ray imaging. *Scientific Reports* **3,** 3209 (2013) (Cited on page 2).

[Bech, 2009] Bech, M. *X-ray imaging with a grating interferometer* Dissertation (University of Copenhagen, 2009) (Cited on page 9).

[Beer, 1852] Beer. Bestimmung der Absorption des rothen Lichts in farbigen Flüssigkeiten. *Annalen der Physik und Chemie* **162,** 78–88 (1852) (Cited on page 7).

[Bertram, 2007] Bertram, M., Hohmann, S. & Wiegert, J. SU-FF-I-22: Scatter Correction for Flat Detector Cone-Beam CT Based On Simulated Sphere Models. *Medical Physics* **34,** 2342–2343 (2007) (Cited on page 26).

[Bérujon, 2012] Bérujon, S., Ziegler, E., Cerbino, R. & Peverini, L. Two-Dimensional X-Ray Beam Phase Sensing. *Physical Review Letters* **108,** 158102 (2012) (Cited on page 2).

[BfS, 2022] BfS. *X-ray diagnostics: Frequency and radiation exposure of the German population.* `https://www.bfs.de/EN/topics/ion/medicine/diagnostics/x-rays/frequency-exposure.html` (2022) (Cited on page 1).

[Bonse, 1965] Bonse, U. & Hart, M. An X-ray Interferometer. *Applied Physics Letters* **6,** 155–156 (1965) (Cited on page 2).

[BfS, 2016] Bundesamt für Strahlenschutz. Bekanntmachung der aktualisierten diagnostischen Referenzwerte für diagnostische und interventionelle Röntgenanwendungen. **2010** (2016) (Cited on page 16).

[Chabior, 2011] Chabior, M. *et al.* Signal-to-noise ratio in x ray dark-field imaging using a grating interferometer. *Journal of Applied Physics* **110,** 053105 (2011) (Cited on page 25).

[Chen, 2020] Chen, N. *et al.* Epidemiological and clinical characteristics of 99 cases of 2019 novel coronavirus pneumonia in Wuhan, China: a descriptive study. *The Lancet* **395,** 507–513 (2020) (Cited on page 65).

[Ching, 2014] Ching, W., Robinson, J. & Mcentee, M. Patient-based radiographic exposure factor selection: A systematic review. *Journal of Medical Radiation Sciences* **61,** 176–190 (2014) (Cited on page 43).

[EC, 1997] Council of the European Union. *Council Directive 97/43/Euratom of 30 June 1997 on health protection of individuals against the dangers of ionizing radiation in relation to medical exposure, and repealing Directive 84/466/Euratom* 1997 (Cited on page 17).

[Dave, 2018] Dave, J. K. *et al.* Current state of practice regarding digital radiography exposure indicators and deviation indices: Report of AAPM Imaging Physics Committee Task Group 232. *Medical Physics* **45.** doi:10.1002/mp.13212 (2018) (Cited on page 18).

[De Marco, 2021] De Marco, F. D. *Image reconstruction, pre-clinical studies, and signal formation investigations at a dark-field chest radiography setup* Dissertation (Technische Universität München, 2021) (Cited on pages 12, 13).

[DIN, 2013] DIN Deutsches Institut für Normung e.V. *DIN 6868-150:2013-06, Sicherung der Bildqualität in röntgendiagnostischen Betrieben - Teil 150: Abnahmeprüfung nach RöV an medizinischen Röntgeneinrichtungen für Aufnahme und Durchleuchtung* 2013. doi:http://dx.doi.org/10.31030/1937120 (Cited on page 61).

[Drexler, 1993] Drexler, G., Panzer, W. & Stieve, F.-E. *Die Bestimmung von Organdosen in der Röntgendiagnostik* 2., überar, 48 S. (Hoffmann, Berlin, 1993) (Cited on page 39).

[Eastman, 2011] Eastman, T. R. Exposure technique documentation. *Radiologic technology* **83,** 202–3 (2011) (Cited on page 43).

[European Commision, 1999] European Commision. Guidance on Diagnostic Reference Levels (DRLs) for Medical Exposures. *Nuclear Safety and Civil Protection* (1999) (Cited on pages 16, 30).

[EC, 2011] European Commission Directorate-General for Energy *et al. European study on clinical diagnostic reference levels for X-ray medical imaging: EUCLID* doi:doi/10.2833/452154 (Publications Office, 2021) (Cited on page 41).

[Faller, 2020] Faller, A. & Schünke, M. *Der Körper des Menschen* 18th (eds Faller, A., Schünke, M. & Schünke, G.) doi:10.1055/b000000452 (Georg Thieme Verlag, Stuttgart, 2020) (Cited on page 18).

[FDA, 2022] FDA. *Medical X-ray Imaging* https://www.fda.gov/radiation-emitting-products/medical-imaging/medical-x-ray-imaging (2022) (Cited on pages 1, 2).

[Frank, 2018] Frank, M. *Characterization of a Dark-field Chest Radiography Scanner* Master Thesis (Technical University of Munich, 2018) (Cited on pages 21, 29).

[Frank, 2022] Frank, M. *et al.* Dark-field chest X-ray imaging for the assessment of COVID-19-pneumonia. *Communications Medicine* **2,** 147 (2022) (Cited on pages 65, 67, 70, 73).

[Frank, 2021] Frank, M. *et al.* Dosimetry on first clinical darkfield chest radiography. *Medical Physics* **48,** 6152–6159 (2021) (Cited on pages 29, 31, 49).

[Frank, in Review] Frank, M. *et al.* Exposure Control at the First Dark-Field Chest Radiography Demonstrator System. *In Review at Medical Physics* (Cited on page 43).

[Gassert, 2021] Gassert, F. T. *et al.* X-ray Dark-Field Chest Imaging: Qualitative and Quantitative Results in Healthy Humans. *Radiology* **301,** 389–395 (2021) (Cited on pages 41, 66, 68, 69, 75, 80, 83).

[Gassert, Submitted] Gassert, F. T. *et al.* Comparison of Dark-field Chest Radiography and CT for the Assessment of COVID-19 Pneumonia. *Submitted to European Radiology* (Cited on page 69).

[Geise, 2001] Geise, R. A. Fluoroscopy: Recording of Fluoroscopic Images and Automatic Exposure Control. *RadioGraphics* **21,** 227–236 (2001) (Cited on page 43).

[GOLD, 2020] Global Initiative for Chronic Obstuctive Lung Disease. *Global Strategy for the Diagnosis, Management, and Prevention of Chronic Obstructive Pulmonary Disease* tech. rep. (2020 Global Initiative for Chronic Obstructive Lung Disease, 2020) (Cited on page 18).

[Gromann, 2017] Gromann, L. B. *et al.* In-vivo X-ray Dark-Field Chest Radiography of a Pig. *Scientific Reports* **7,** 1–7 (2017) (Cited on page 2).

[Harris, 2020] Harris, C. R. *et al.* Array programming with NumPy. *Nature* **585,** 357–362 (2020) (Cited on page 68).

[Hellbach, 2018] Hellbach, K. *et al.* Depiction of pneumothoraces in a large animal model using x-ray dark-field radiography. *Scientific Reports* **8,** 2602 (2018) (Cited on pages 2, 41).

[Hellbach, 2015] Hellbach, K. *et al.* In Vivo Dark-Field Radiography for Early Diagnosis and Staging of Pulmonary Emphysema. *Investigative Radiology* **50,** 430–435 (2015) (Cited on pages 2, 41).

[Hellbach, 2017] Hellbach, K. *et al.* X-ray dark-field radiography facilitates the diagnosis of pulmonary fibrosis in a mouse model. *Scientific Reports* **7,** 340 (2017) (Cited on pages 2, 41).

[Hosch, 2012] Hosch, W. *et al.* Reduction of radiation exposure and improvement of image quality with BMI-adapted prospective cardiac computed tomography and iterative reconstruction. *European Journal of Radiology* **81,** 3568–3576 (2012) (Cited on page 62).

[Huda, 1989] Huda, W., Sandison, G. A., Palser, R. F. & Savoie, D. Radiation doses and detriment from chest X-ray examinations. *Physics in Medicine and Biology* **34,** 1477–1492 (1989) (Cited on page 33).

[Hurt, 2022] Hurt, B. *et al.* Radiologist-supervised Transfer Learning. *Journal of Thoracic Imaging* **37,** 90–99 (2022) (Cited on pages 72, 76).

[ICRP, 1997] ICRP. ICRP Publication 26: Recommendations of the Radiological Protection. *Annals of the ICRP,* 1–87 (1997) (Cited on pages 33, 43).

[IEC, 2008] International Electrotechnical Commission. Medical electrical equipment–Exposure index of digital X-ray imaging systems-Part 1: Definitions and requirements for general radiography. *IEC, Geneva, Switzerland,* 62491–62494 (2008) (Cited on pages 17, 18, 44).

[JHU, 2022] Johns Hopkins University. *COVID-19 Dashboard* `https://gisanddata.maps.arcgis.com/apps/dashboards/bda7594740fd40299423467b48e9ecf6` (2022) (Cited on page 20).

[Jones, 1985] Jones, D. & Wall, B. Organ Doses from Medical X-ray Examinations Calculated Using Monte Carlo Techniques. *NRPB-186,* 87 (1985) (Cited on page 33).

[Kalra, 2004] Kalra, M. K. *et al.* Techniques and applications of automatic tube current modulation for CT. *Radiology* **233,** 649–657 (2004) (Cited on page 44).

[Koehler, 2015] Koehler, T. *et al.* Slit-scanning differential x-ray phase-contrast mammography: Proof-of-concept experimental studies. *Medical Physics* **42,** 1959–1965 (2015) (Cited on pages 13, 21).

[Kottler, 2007] Kottler, C., Pfeiffer, F., Bunk, O., Grünzweig, C. & David, C. Grating interferometer based scanning setup for hard x-ray phase contrast imaging. *Review of Scientific Instruments* **78,** 1–4 (2007) (Cited on pages 12, 21).

[Lakhani, 2021] Lakhani, P. *et al.* The 2021 SIIM-FISABIO-RSNA Machine Learning COVID-19 Challenge: Annotation and Standard Exam Classification of COVID-19 Chest Radiographs. (2021) (Cited on pages 68, 72, 83).

[Le Heron, 1992] Le Heron, J. C. Estimation of effective dose to the patient during medical X-ray examinations from measurements of the dose-area product. *Physics in Medicine and Biology* **37,** 2117–2126 (1992) (Cited on pages 14, 15).

[Lechel, 2009] Lechel, U., Becker, C., Langenfeld-Jäger, G. & Brix, G. Dose reduction by automatic exposure control in multidetector computed tomography: comparison between measurement and calculation. *European Radiology* **19,** 1027–1034 (2009) (Cited on pages 30, 32, 33, 38).

[Li, 2020] Li, Q. *et al.* Early Transmission Dynamics in Wuhan, China, of Novel CoronavirusInfected Pneumonia. *New England Journal of Medicine* **382,** 1199–1207 (2020) (Cited on page 65).

[Mahase, 2021] Mahase, E. Covid-19: Where are we on vaccines and variants? *BMJ* **372,** n597 (2021) (Cited on page 77).

[Markivee, 1980] Markivee, C. R., Edwards, F. M. & Leonard, P. Microcomputer Controlled Diagnostic X-Ray Exposure Factors: A Pilot Study. *Proceedings. Symposium on Computer Applications in Medical Care* **1,** 113–116 (1980) (Cited on page 43).

[Meinel, 2013] Meinel, F. G. *et al.* Diagnosing and Mapping Pulmonary Emphysema on X-Ray Projection Images: Incremental Value of Grating-Based X-Ray Dark-Field Imaging. *PLoS ONE* **8** (ed Taube, C.) e59526 (2013) (Cited on pages 2, 41).

[Meiser, 2016] Meiser, J. *et al.* Increasing the field of view in grating based X-ray phase contrast imaging using stitched gratings. *Journal of X-Ray Science and Technology* **24,** 379–388 (2016) (Cited on page 21).

[Mentrup, 2016] Mentrup, D., Jockel, S., Menser, B. & Neitzel, U. Iterative scatter correction for grid-less bedside chest radiography: Performance for a chest phantom. *Radiation Protection Dosimetry* **169,** 308–312 (2016) (Cited on page 26).

[Mentrup, 2014] Mentrup, D., Jockel, S., Neitzel, U., Menser, B., *et al. Grid-like contrast restoration for non-grid chest radiographs by software-based scatter correction* in *ECR congress* (2014). doi:10.1594/ecr2014/C-0181 (Cited on page 26).

[Mettler, 2008] Mettler, F. A., Huda, W., Yoshizumi, T. T. & Mahesh, M. Effective doses in radiology and diagnostic nuclear medicine: A catalog. *Radiology* **248,** 254–263 (2008) (Cited on pages 1, 20, 38, 39).

[Mohr, 2012] Mohr, J. *et al. High aspect ratio gratings for X-ray phase contrast imaging* in *American Institute of Physics Conference Series* (eds Momose, A. & Yashiro, W.) **1466** (2012), 41–50. doi:10.1063/1.4742267 (Cited on page 21).

[Momose, 2003] Momose, A. *et al. Demonstration of x-ray Talbot interferometry* 2003. doi:10.1143/JJAP.42.L866 (Cited on pages 2, 8).

[Nenot, 2009] Nenot, J.-C., Brenot, J., Laurier, D., Rannou, A. & Thierry, D. *ICRP Publication 103: The 2007 Recommendations of the International Commission on Radiological Protection* tech. rep. (France, 2009), 417 (Cited on pages 14–16, 29, 32–35).

[Noichl, 2022] Noichl, W. *et al.* Correction for mechanical inaccuracies in a scanning Talbot-Lau interferometer (2022) (Cited on page 25).

[Obuchowski, 1997] Obuchowski, N. A. Nonparametric Analysis of Clustered ROC Curve Data. *Biometrics* **53,** 567 (1997) (Cited on page 68).

[Pfeiffer, 2018] Pfeiffer, F., Reiser, M. & Rummeny, E. Röntgen-Phasenkontrast. *Der Radiologe* **58,** 218–225 (2018) (Cited on pages 1, 2).

[Pfeiffer, 2008] Pfeiffer, F. *et al.* Hard-X-ray dark-field imaging using a grating interferometer. *Nature Materials* **7,** 134–137 (2008) (Cited on pages 2, 8, 13).

[Pfeiffer, 2009] Pfeiffer, F. *et al.* X-ray dark-field and phase-contrast imaging using a grating interferometer. *Journal of Applied Physics* **105,** 102006 (2009) (Cited on pages 2, 8, 10).

[Pfeiffer, 2006] Pfeiffer, F., Weitkamp, T., Bunk, O. & David, C. Phase retrieval and differential phase-contrast imaging with low-brilliance X-ray sources. *Nature Physics* **2,** 258–261 (2006) (Cited on pages 2, 8, 9).

[Pfeiffer, 2013] Pfeiffer, F. *et al.* Grating-based X-ray phase contrast for biomedical imaging applications. *Zeitschrift für Medizinische Physik* **23,** 176–185 (2013) (Cited on page 2).

[Pratt, 1987] Pratt, P. C. Role of conventional chest radiography in diagnosis and exclusion of emphysema. *The American Journal of Medicine* **82,** 998–1006 (1987) (Cited on page 20).

[Prokop, 2020] Prokop, M. *et al.* CO-RADS: A Categorical CT Assessment Scheme for Patients Suspected of Having COVID-19 – Definition and Evaluation. *Radiology* **296,** E97–E104 (2020) (Cited on pages 28, 66).

[Raptis, 2020] Raptis, C. A. *et al.* Chest CT and Coronavirus Disease (COVID-19): A Critical Review of the Literature to Date. *American Journal of Roentgenology* **215,** 839–842 (2020) (Cited on pages 20, 65).

[Rayleigh, 1881] Rayleigh, L. XXV. On copying diffraction-gratings, and on some phenomena connected therewith. *The London, Edinburgh, and Dublin Philosophical Magazine and Journal of Science* **11,** 196–205 (1881) (Cited on page 8).

[Richmond, 1985] Richmond, C. R. ICRP Publication 23: Report on the Task Group on Reference Man. *International Journal of Radiation Biology and Related Studies in Physics, Chemistry and Medicine* **48,** 285 (1985) (Cited on pages 30, 36, 38).

[Röntgen, 1896] Röntgen, W. C. On a New Kind of Rays. *Science* **3,** 227–231 (1896) (Cited on pages 1, 5).

[Rubin, 2020] Rubin, G. D. *et al.* The Role of Chest Imaging in Patient Management During the COVID-19 Pandemic: A Multinational Consensus Statement From the Fleischner Society. *Chest* **158,** 106–116 (2020) (Cited on page 65).

[Saure, 2008] Saure, D. Qualitätssicherung in der Röntgendiagnostik und in der Computertomografie: aktualisierte Leitlinien der deutschen Bundesärztekammer. *Radiopraxis* **1,** 99–100 (2008) (Cited on pages 30, 45, 49, 81).

[Sauter, 2021] Sauter, A. P. *et al.* Correlation of image quality parameters with tube voltage in X-ray dark-field chest radiography: a phantom study. *Scientific Reports* **11,** 14130 (2021) (Cited on page 23).

[Schegerer, 2014] Schegerer, A. A. *et al.* Dose and Image Quality of Cone-Beam Computed Tomography as Compared With Conventional Multislice Computed Tomography in Abdominal Imaging. *Investigative Radiology* **49,** 675–684 (2014) (Cited on page 30).

[Schegerer, 2019] Schegerer, A., Loose, R., Heuser, L. J. & Brix, G. Diagnostic Reference Levels for Diagnostic and Interventional X-Ray Procedures in Germany: Update and Handling. *RöFo - Fortschritte auf dem Gebiet der Röntgenstrahlen und der bildgebenden Verfahren* **191,** 739–751 (2019) (Cited on pages 16, 30, 33, 40).

[Scherer, 2017] Scherer, K. *et al.* X-ray Dark-field Radiography - In-Vivo Diagnosis of Lung Cancer in Mice. *Scientific Reports* **7,** 402 (2017) (Cited on page 41).

[Schick, 2022] Schick, R. C. *et al.* Correction of Motion Artifacts in Dark-Field Radiography of the Human Chest. *IEEE Transactions on Medical Imaging* **41,** 895–902 (2022) (Cited on page 25).

[Schleede, 2012] Schleede, S. *et al.* Emphysema diagnosis using X-ray dark-field imaging at a laser-driven compact synchrotron light source. *Proceedings of the National Academy of Sciences* **109,** 17880–17885 (2012) (Cited on page 41).

[Schlegel, 2002] *Medizinische Physik 2* (eds Schlegel, W. & Bille, J.) doi:10.1007/978-3-642-56259-4 (Springer Berlin Heidelberg, Berlin, Heidelberg, 2002) (Cited on page 29).

[Schreiner, 2017] Schreiner, M. M. *et al.* A BMI-adjusted ultra-low-dose CT angiography protocol for the peripheral arteries-Image quality, diagnostic accuracy and radiation exposure. *European Journal of Radiology* **93,** 149–156 (2017) (Cited on page 62).

[Schröter, 2017] Schröter, T. J. *et al.* Large field-of-view tiled grating structures for X-ray phase-contrast imaging. *Review of Scientific Instruments* **88,** 015104 (2017) (Cited on page 21).

[Self, 2013] Self, W. H., Courtney, D. M., McNaughton, C. D., Wunderink, R. G. & Kline, J. A. High discordance of chest x-ray and computed tomography for detection of pulmonary opacities in ED patients: Implications for diagnosing pneumonia. *American Journal of Emergency Medicine* **31,** 401–405 (2013) (Cited on pages 75, 76).

[Seltzer, 2011] Seltzer, S. M. *et al.* Report 85: Fundamental Quantities and Units for Ionizing Radiation. *Journal of the ICRU* **11,** 5–6 (2011) (Cited on page 14).

[Snigirev, 1995] Snigirev, A., Snigireva, I., Kohn, V., Kuznetsov, S. & Schelokov, I. On the possibilities of xray phase contrast microimaging by coherent highenergy synchrotron radiation. *Review of Scientific Instruments* **66,** 5486–5492 (1995) (Cited on page 2).

[Suleski, 1997] Suleski, T. J. Generation of Lohmann images from binary-phase Talbot array illuminators. *Applied optics* **36,** 4686–4691 (1997) (Cited on page 8).

[Talbot, 1836] Talbot, H. LXXVI. Facts relating to optical science. No. IV. *The London, Edinburgh, and Dublin Philosophical Magazine and Journal of Science* **9,** 401–407 (1836) (Cited on page 8).

[Taylor, 2021] Taylor, L. Covid-19: Brazil's spiralling crisis is increasingly affecting young people. *BMJ* **373,** n879 (2021) (Cited on page 77).

[Tomashefski, 2008] *Dail and Hammar's Pulmonary Pathology* (eds Tomashefski, J. F., Cagle, P. T., Farver, C. F. & Fraire, A. E.) doi:10.1007/978-0-387-68792-6 (Springer New York, New York, NY, 2008) (Cited on page 18).

[Uffmann, 2005] Uffmann, M. *et al.* Flat-PanelDetector Chest Radiography: Effect of Tube Voltage on Image Quality. *Radiology* **235,** 642–650 (2005) (Cited on page 83).

[Umkehrer, 2022] Umkehrer, S. M. *Phase-contrast Radiography and Dark-field Computed Tomography for the Detectionof Bronchial and Pulmonary Pathologies* Dissertation (Technische Universität München, 2022) (Cited on page 9).

[Urban, in Review] Urban, T., Noichl, W., Koehler, T., Engel, K. J. & Pfeiffer, F. Correction for Optical and X-ray Scatter in Dark-Field Radiography. *In Review at IEEE Transactions on Medical Imaging* (Cited on page 26).

[Urban, Submitted] Urban, T. *et al.* Dark-Field Chest Radiography Outperforms Conventional Chest Radiography for the Diagnosis and Staging of Pulmonary Emphysema. *Submitted to European Radiology* (Cited on page 80).

[Urban, 2022] Urban, T. *et al.* Qualitative and Quantitative Assessment of Emphysema Using Dark-Field Chest Radiography. *Radiology* **303,** 119–127 (2022) (Cited on pages 41, 66, 68, 69, 80).

[Valentin, 2002] Valentin, J. & Streffer, C. ICRP Publication 89: Basic anatomical and physiological data for use in radiological protection: Reference values. *Annals of the ICRP* **32,** 1–277 (2002) (Cited on page 31).

[Velroyen, 2015] Velroyen, A. *et al.* Grating-based X-ray Dark-field Computed Tomography of Living Mice. *EBioMedicine* **2,** 1500–1506 (2015) (Cited on page 2).

[Viermetz, 2022a] Viermetz, M. *et al.* Dark-field computed tomography reaches the human scale. *Proceedings of the National Academy of Sciences* **119.** doi:10.1073/pnas.2118799119 (2022) (Cited on page 81).

[Viermetz, 2022b] Viermetz, M. *et al.* Technical design considerations of a human-scale Talbot-Lau interferometer for dark-field CT. *IEEE Transactions on Medical Imaging,* 1–1 (2022) (Cited on page 81).

[Virtanen, 2020] Virtanen, P. *et al.* SciPy 1.0: fundamental algorithms for scientific computing in Python. *Nature Methods* **17,** 261–272 (2020) (Cited on page 68).

[Wall, 2011] Wall, B. F. *et al.* Radiation risks from medical X-ray examinations as a function of the age and sex of the patient. *Health Protection Agency Centre for Radiation, Chemical and Environmental Hazards,* 978– (2011) (Cited on pages 16, 30, 38).

[Willer, 2022] Willer, K. *Development of a Dark-Field Chest Radiography Prototype System for the Initial Clinical Evaluation in COPD Patients* Dissertation (Technische Universität München, 2022) (Cited on pages 10, 21, 23, 44, 79).

[Willer, 2021] Willer, K. *et al.* X-ray dark-field chest imaging for detection and quantification of emphysema in patients with chronic obstructive pulmonary disease: a diagnostic accuracy study. *The Lancet Digital Health* **3,** e733–e744 (2021) (Cited on pages 29, 41, 80).

[WHO, 2021] World Health Organization. *The top 10 causes of death* https://www.who.int/news-room/fact-sheets/detail/the-top-10-causes-of-death (2021) (Cited on page 20).

[Yanch, 2009] Yanch, J. C., Behrman, R. H., Hendricks, M. J. & McCall, J. H. Increased radiation dose to overweight and obese patients from radiographic examinations. *Radiology* **252,** 128–139 (2009) (Cited on page 39).

[Yaroshenko, 2015] Yaroshenko, A. *et al.* Improved In vivo Assessment of Pulmonary Fibrosis in Mice using X-Ray Dark-Field Radiography. *Scientific Reports* **5,** 17492 (2015) (Cited on pages 2, 41).

[Yaroshenko, 2013] Yaroshenko, A. *et al.* Pulmonary Emphysema Diagnosis with a Preclinical Small-Animal X-ray Dark-Field Scatter-Contrast Scanner. *Radiology* **269,** 427–433 (2013) (Cited on page 2).

[Yaroshenko, 2016] Yaroshenko, A. *et al.* Visualization of neonatal lung injury associated with mechanical ventilation using x-ray dark-field radiography. *Scientific Reports* **6,** 24269 (2016) (Cited on page 2).

[Zoetelief, 2005] Zoetelief, J., Dance, D., Drexler, G., Järvinen, H. & Rosenstein, M. Report 74: Patient Dosimetry for X-rays used in Medical Imaging. *Journal of the International Commission on Radiation Units and Measurements* **5.** doi:10.1093/jicru/ndi016 (2005) (Cited on pages 14–17).

[Zoetelief, 2002] Zoetelief, J., Julius, H. W. & Christensen, P. Recommendations for patient dosimetry in diagnostic radiology using thermoluminescence dosimetry (IAEA-CN-96/46P). *Standards and Codes of Practice in Medical Radiation Dosimetry. Proceedings of an International Symposium, Vienna, 35-38 November 2002* **1,** 439–447 (2002) (Cited on page 30).

List of Figures

List of Tables